PHYSICS MODELING OF STRENUOUS GROUND SELF-RIGHTING AND CLUTTERED LARGE OBSTACLE TRAVERSAL

by
Qihan Xuan

A dissertation submitted to Johns Hopkins University in conformity with the requirements for the degree of Doctor of Philosophy

Baltimore, Maryland
February 2024

Abstract

Mobile robots are becoming increasingly prevalent in society. While many of these robots are designed for simple terrains, there is a growing demand for their use in more complex environments, such as search and rescue through earthquake rubble, environmental monitoring through dense vegetation, and extraterrestrial exploration through Martian and lunar rocks.

However, traversing these environments poses challenges, current robots often get stuck on obstacles or flip over. Enhancing self-righting and traversal capabilities is vital. Studying biological models, like the discoid cockroach, which excels at moving through vegetation and rocky terrain with rapid self-righting, provides valuable insights.

Observations from animal experiments show that the cockroach can push both its wings together against the ground and flail its legs laterally to self-right. We noted a significant randomness in the movements of both wings and legs during this strenuous ground self-righting. While randomness is typically considered a nuisance, in this context, we sought to study whether it is beneficial for strenuous self-righting. We developed a simplified simulation robot capable of generating similar self-righting behavior and varied the randomness level in wing-leg coordination. We found that wing-leg coordination, measured by the phase between wing and leg oscillations, had a crucial impact on self-righting outcome. With randomness, the system explored phases thoroughly and had a better chance of encountering good phases to self-right. Our study demonstrated that randomness helps destabilize locomotor systems from being trapped in undesired metastable states, a situation common in strenuous locomotion.

We delved deeper into the phase between wing and leg oscillations and its significant impact on self-righting by creating a dynamic model template. This model helped us quantify the potential energy barrier the body must surpass to self-right, the mechanical energy from wing pushing and leg flailing, and energy loss from wing-ground collisions. It became clear that wing-leg coordination, or phase, strongly influences the self-righting outcome by changing mechanical energy budget. Lastly, we utilized the template to propose improved control methodologies and offer insights for robotic design.

Our studies also highlight the importance of environmental force sensing in assisting robots with challenging locomotion tasks, such as traversing cluttered large obstacles. Inspired by cockroaches, we demonstrated in simulation that environmental force sensing helps robots traverse cluttered large obstacles. By creating a physics model, we were able to determine beam stiffness from the robot's contact forces. With model-based feedback control, the robot can select the locomotor mode with a lower mechanical energy cost.

Drawing inspiration from animals and utilizing physics-based models and simulations, our research not only deepens our understanding of animal behavior (the biological aspect) but also provides valuable insights for enhancing robotic design and control in challenging conditions (the robotic aspect).

Primary Reader and Advisor: Chen Li

Secondary Readers: Noah J. Cowan, Marin Kobilarov

Acknowledgments

I am profoundly grateful for the mentorship and guidance of my advisor, Prof. Chen Li, throughout my Ph.D. journey. His dedication to rigorous scientific research, coupled with his unwavering support during the pandemic and my career development, has been invaluable. His unwavering optimism, meticulousness, and commitment to scholarship have left an indelible mark on my academic journey.

I would like to extend my appreciation to Prof. Noah Cowan, not only for the foundational courses he taught but also for his constructive feedback on my research, his unwavering support in my career progression, and for his vital contribution to my dissertation. Similarly, I wish to express my gratitude to Prof. Marin Kobilarov. His insightful course, the opportunity to serve as his teaching assistant, and his valuable feedback on my research and contribution to my dissertation have greatly enriched my Ph.D. journey.

Working with the members of the Terradynamics Lab has been both an honor and a pleasure. The assistance and camaraderie of Dr. Ratan Othayoth, Dr. Qiyuan Fu, Yaqing Wang, Bokun Zheng, Yifeng Zhang, Divya Ramesh, Eugene Lin, Zhiyi Ren, Dr. Sean Gart, Jonathan Mi, Dr. Yuanfeng Han, Gargi Sadalgekar, Kaiwen Wang, Kangxin Wang, Changfan Chen, Kaiyue Wu, Jonathan Mi, Dr. Huidong Gao, Changxing Yan, Dr. Thomas Mitchel, Dr. Hongtao Wu, Yucheng Kang, Siyuan Yu, Kapi Ketan Mehta, Soowon Kim, Zheliang Wang, Eric Lara, Zhong Guan, and many others have not only enriched my research but also my life.

I am particularly indebted to Professors Noah Cowan, Gregory Chirikjian, Marin Kobilarov, Pablo Iglesias, and Simon Leonard for their roles in my qualification exams and endorsement of my Ph.D. candidacy.

I would like to acknowledge the insightful suggestions and comments from Ratan Othayoth, Qiyuan Fu, Yaqing Wang, Yifeng Zhang, Soowon Kim, Zhiyi Ren, Tom Libby, Prof. Noah Cowan, Prof. Shai Revzen, Prof. Daniel Goldman, Prof. Greg Chirikjian, Prof. Yang Ding, Prof. Avanti Athreya. Special thanks to Prof. Dan Negrut, Dr. Arman Pazouki, Dr. Radu Serban, and Dr. Luning Fang for their invaluable assistance with the Chrono engine. My academic journey was further enriched by the feedback I received from the scientific communities, particularly those at the Society for Integrative and Comparative Biology, the American Physical Society, and International Conference on Intelligent Robots and Systems.

The administrative staff at the Department of Mechanical Engineering and the Laboratory for Computational Sensing and Robotics provided indispensable support, enabling me to focus my energies on my academic pursuits. In particular, I'd like to mention Mike Bernard, Kevin Adams, John Soos, Patrick Caufield, Lorrie Dodd, Jordan Card, Ashley Moriarty, and Alison Morrow.

I am thankful for the essential financial resources that facilitated my Ph.D. journey, including the Army Research Office, Burroughs Wellcome Fund, the Whiting School of Engineering, and Johns Hopkins University.

My friends have been an incredible source of support and joy throughout this journey. My heartfelt thanks to Yu Yang, Xiangze Zeng, Siming Deng, Qiyuan Fu, Zhiyi Ren, Changfan Chen, Kaiwen Wang, Mengze Wang, Zheliang Wang, Chengda Ji,

Changyan He, He Chen, Tanqi Zheng, Zhaoshuo Li for their companionship, support, and shared moments of joy.

My heartfelt appreciation goes to my wife, Di Cao. Throughout my Ph.D. journey, our shared moments of happiness have been a source of great joy. We have provided emotional, research, and life support for each other. Her understanding, steadfast companionship, and unwavering support have been my guiding light in challenging times. Her presence in my life is indeed a blessing.

Finally, to my family, especially my parents Xingding Xuan and Youdi Xue, thank you for your boundless love and support. Your tireless efforts, both financial and emotional, have been the backbone of my journey to becoming a Ph.D. Without you, this achievement would have been impossible.

Table of contents

List of Tables

List of Figures

Chapter 1

Introduction

1.1 Motivation and overview

Mobile robots are increasingly becoming prevalent in society, serving a variety of purposes across numerous domains. However, the mobility of current robotic systems is mostly restricted to relatively simple terrains, such as flat surfaces with sparse obstacles. These obstacles can be detected and avoided through sensing environmental geometry, like robot vacuum cleaners (Tribelhorn and Dodds, 2007) and self-driving vehicles (Thrun et al., 2000).

There is a growing demand for robots capable of operating in more complex environments, such as search and rescue through earthquake rubble (Pratt, 2014; Reddy et al., 2015), environmental monitoring through dense vegetation (Oliveira et al., 2021), and extraterrestrial exploration through Martian and lunar rocks (Li and Lewis, 2022)

(**Figure 1**). In such scenarios, current robots often face challenges. They may risk losing stability or even flipping over (Guizzo and Ackerman, 2015a; Li et al., 2017).

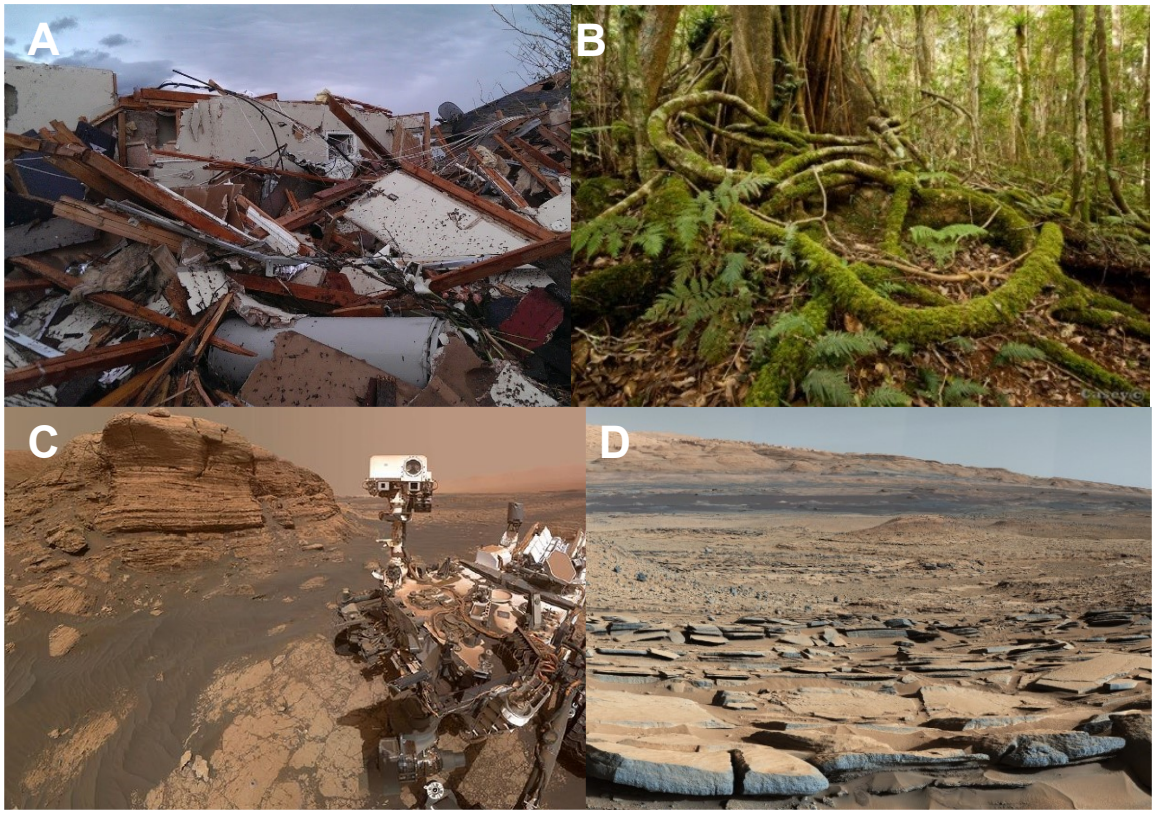

Figure 1. Robots' applications on complex terrain. (A) Search and rescue through earthquake rubble. Reproduced from (Othayoth et al., 2020). (B) Environmental monitoring through dense vegetation. Images courtesy of Luke Casey. (C, D) Extraterrestrial exploration (Curiosity Rover on Mars). Images courtesy of NASA (https://photojournal.jpl.nasa.gov/catalog/PIA24543; https://mars.nasa.gov/resources/7505/strata-at-base-of-mount-sharp/).

Planetary exploration stands as a particularly practical and urgent task, attracting significant investment in terms of time and resources to enhance robotic mobility. Reflecting this priority, mobile planetary exploration robots have steadily improved their ability to maneuver on extraterrestrial surfaces (Ellery, 2015; Gao, 2016). The Rover Opportunity, for example, set a record by driving over 45 km on Mars (NASA/JPL-Caltech,

2019). However, there are still scientifically interesting sites that remain challenging for rovers to access. This is largely due to significant mobility constraints, especially when encountering large, cluttered obstacles. These obstacles not only limit movement but also pose a risk of damaging the wheels. For instance, as shown in **Figure 1**C, the Curiosity Rover approached a 4 m-high outcrop known as “Mont Mercou,” characterized by stiff, large rocks; in **Figure 1**D, the Curiosity Rover was at the “Square Top” outcrop, where the terrain features a dense clutter of rocks. Although these sites are scientifically interesting, the Rover chose not to move closer to protect its wheels.

The wheeled-based design limits a rover's locomotion capabilities. Therefore, some newer rover platforms have incorporated leg-like degrees of freedom to control wheels, enabling gaits akin to legged motion (Shrivastava et al., 2020). More research has been conducted to study legged robotics, with the RHex robot standing as a notable example (Altendorfer et al., 2001; Saranli et al., 2001). This six-legged robot is known for its versatility and agility, enabling it to traverse a wide variety of terrains. For instance, it can run on rocky ground (Saranli et al., 2001), climb high steps (Moore et al., 2002), traverse sandy terrain (Li et al., 2009) and water surfaces (Kim et al., 2016), and leap over sizable obstacles (Chou et al., 2015). While this legged robot shows greater adaptability to varied terrains than wheeled robots, using specific modes for different locomotor challenges, it still faces difficulties in traversing highly complex terrains that require transitioning between these modes. This difficulty arises primarily from the lack of a comprehensive understanding of how to compose these mode transitions (Othayoth et al., 2020; Othayoth et al., 2021).

More advanced robots have been developed with the capability to traverse complex terrains and perform various tasks. Examples like Big Dog (Raibert, 2008), ANYmal (Hutter et al., 2016), MIT's Cheetah (Bledt et al., 2018) and DRC Hubo (Wang et al., 2014)

showcase this capability. Early research on leg-ground interaction over flat, rigid surfaces with small obstacles has revealed key principles for achieving stable, limit-cycle locomotion like walking and running (Blickhan, 1989; Blickhan and Full, 1993; Holmes et al., 2006; Koditschek et al., 2004; Kuo, 2007; Saranli et al., 2001). Recent deep learning techniques have helped multilegged robots traverse easier terrains by focusing on keeping their bodies upright. However, this deep learning approach is like a "black box," making it hard to understand or predict how it would work in new situations not covered in training, unlike methods based on physics. Also, the strategies learned mainly support upright walking and running, and try to stabilize this steady-state, limit cycle-like locomotion, limiting the robots to handling obstacles much smaller than themselves (Choi et al., 2023; Hwangbo et al., 2019; Tan et al., 2018). Thus, when traversing large obstacles (larger or comparable to their body size), these robots still encounter limitations in basic physical movement skills, where they lag behind animals. This was evident in the DARPA Robotics Challenge (DRC), where tasks simple for humans proved challenging for these robots, with many of them struggling and even falling (Guizzo and Ackerman, 2015a; Guizzo and Ackerman, 2015b), especially when traversing through rubble terrain filled with large and cluttered obstacles. The RHex usually moves slowly over large obstacles due to its complex controls (Chou et al., 2012), and despite adding a rounded shell, it still falls short of animals in traversing narrow spaces between large beams (Li et al., 2015).

Modern mobile robots demonstrate lower mobility on complex terrains filled with large and cluttered obstacles compared to animals. These challenging conditions are typical in scenarios such as search and rescue operations in earthquake rubble (Pratt, 2014; Reddy et al., 2015), environmental monitoring in dense vegetation (Oliveira et al., 2021), and exploration on Mars and Moon (Li and Lewis, 2022). Consequently, biological organisms have become a rich source of inspiration for improving robotic mobility in these

challenging environments (Clifton et al., 2023). However, due to the high complexity of biological systems, deriving fundamental locomotion principles for robotics often requires starting with simpler models (Aguilar et al., 2016). Recent work using simple models to study animal locomotion on a wide range of complex terrain and understand the principle mechanism have shown promising outcomes (Aguilar et al., 2016; Holmes et al., 2006; Li et al., 2013; Maladen et al., 2011). For instance, researchers investigating locomotion on granular media have not only designed simple systems (robot, simulation, and physics model), but also, through systematic examination, uncovered the fundamental mechanisms of leg-granular media interaction (the resistive force theory in granular locomotion) (Li et al., 2013). This method has been applied to locomotion on terrains featuring large, cluttered obstacles (Gart et al., 2018; Han et al., 2021; Li et al., 2015). My work builds on this approach, concentrating on the development of the physics model and the simulation aspects.

Simulations and physics-based models serve as foundational tools to study locomotion on complex terrains. For instance, simplified spring-mass models effectively capture the running movements of animals of various sizes and shapes (Blickhan, 1989; Blickhan and Full, 1993; Farley et al., 1993). Simulations offer a means to coordinate and control joints with multiple degrees of freedom in legged motion (Coros et al., 2011; Mckenna and Zeltzer, 1990). Additionally, the RHex robot serves as a practical platform for studying and realizing stable and efficient running capabilities in real-world scenarios (Altendorfer et al., 2001; Saranli et al., 2001).

By combining the creation of simplified models with a deep understanding of the underlying principles, we have an iterative development process. This process involves creating simple models to enhance our understanding of locomotion, and in turn, using this knowledge to develop more advanced and capable systems. For example, to study

the dynamics of legged locomotion, a template model called the spring-loaded inverted pendulum (SLIP) was introduced. It is the simplest model of rapid running behavior used as a target for control. It enhanced our understanding of legged locomotion. Building upon this, a more advanced model, the anchor model, was developed to reveal more complex mechanisms by adding legs, joints, and muscles back (Holmes et al., 2006). Drawing from these insights, legged robots were then designed, reflecting the natural dynamics of running. Likewise, for other complex systems, starting with a simple model and progressively addressing realistic challenges can be valuable. Such an approach promises the development of robots that can traverse diverse challenging terrains, thereby broadening their potential applications across multiple societal sectors. Additionally, as engineers enhance robot mobility in real-world scenarios through machine learning based on simulations, the fundamental principles and mechanisms from modeling retain their importance (Alber et al., 2019; Li and Qian, 2023). This is due to the potential limitations in scalability with machine learning, and the fact that simulations might not fully represent real-world conditions. Research has demonstrated that integrating machine learning with modeling can enhance the performance of a four-legged robot, enabling it to move faster across deformable terrain (Choi et al., 2023).

As highlighted earlier, traversing complex terrains with large and cluttered obstacles, similar to those depicted **Figure 1**, presents a significant challenge. Most robots are designed and controlled to stabilize a single locomotor mode (such as walking or running) in an upright posture, that can achieve stable, limit-cycle locomotion to traverse terrain with small obstacles effectively (Blickhan, 1989; Blickhan and Full, 1993; Choi et al., 2023; Holmes et al., 2006; Hwangbo et al., 2019; Koditschek et al., 2004; Kuo, 2007; Saranli et al., 2001; Tan et al., 2018). However, this approach becomes impractical when encountering large, cluttered obstacles. In such situations, the robot must rotate and

employ different locomotor modes, like rolling, pitching, and climbing, to overcome obstacles that are larger or comparable to their body size. Therefore, understanding how to destabilize the limit cycle and transition to a different locomotor mode is crucial. In the recent research on multilegged locomotion, people have uncovered fundamental principles to control physical interactions, allowing for locomotor transitions to traverse various large obstacles, like beams (Li et al., 2015), pillars (Han et al., 2021), gaps (Gart et al., 2018), or bumps (Gart and Li, 2018). These large obstacles comparable to robots' body size and can be simplified into abstract forms (**Figure 2**). The potential energy landscape framework (Othayoth et al., 2020; Othayoth et al., 2021) shows that the locomotor-environment interaction leads to stereotyped locomotor modes because the self-propelled system is attracted to distinct basins of an underlying potential energy landscape (**Figure 3**). Transitioning between locomotor modes requires escaping from these energy basins, a process that involves destabilizing maneuvers away from the stable limit-cycle system. Failure to escape these basins can result in the robot becoming trapped or flipping over. Consequently, it is crucial for mobile robots to develop the ability to recover from failures.

Discoid roaches serve as excellent biological organisms to study because of their remarkable mobility and self-righting ability. They can traverse a diverse range of obstacles, from climbing tall steps to squeezing through tight spaces (Goldman et al., 2006; Li et al., 2015; Sponberg and Full, 2008). Additionally, they can rapidly self-right from the ground (Li et al., 2019a). For cockroaches, achieving a high success rate and rapid self-righting is vital for reducing the risk of predation. Given their capabilities of locomotion failure recovery, we have chosen cockroaches as our model organism to explore how they

escape potential energy basins in the energy landscape, particularly under strenuous conditions.

As noted earlier, the complexity of biological organisms can make it challenging to extract fundamental locomotion principles for robotic systems. To investigate the complex mechanisms underlying cockroaches' self-righting and cluttered, large obstacle traversal behavior, we developed template models and physics-based simulation as simple models to start with.

The template model effectively captures the fundamental characteristics of motion by employing lower-dimensional models to represent the essentials of complex systems, aiding in the understanding of their mechanisms and control (Full and Koditschek, 1999). For instance, in self-righting processes, a 2D template model has been developed, enabling the analytical calculation of potential energy barriers and uncovering the coordination between wings and legs in self-righting actions. Similarly, in beam traversal, a template model for a legless robot is utilized, driven by forward forces and oscillation actuators. This model simplifies joint complexity but focuses on the interaction between the robot's body and beam obstacles, emphasizing the importance of body force sensing in effective traversal. Template model effectively captures and focuses on key elements, deliberately omitting less crucial details, thereby ensuring that the results are broadly applicable across various systems. This focused approach offers clear insights, ensuring a comprehensive understanding of the system's behavior.

When diving into more complex mechanisms, using a simulation engine became essential. It enables a greater degree of freedom in motion, along with enhanced dynamics and control capabilities. Simulations offer a refined tool for accurately modeling systems, capturing their detailed aspects. Additionally, simulations can validate results from

template models and test them under various conditions to ascertain their general applicability. Although simulations are a simplified representation of the real world, often based on numerous assumptions and unable to capture every detail of reality, we employ them for a specific purpose. Our aim is to explore the randomness of self-righting movements. Simulations offer ideal repeatability and precise control over randomness, an aspect where the real world falls short due to its inherent and uncontrollable noise. The randomness in motion was set from none to extensive levels in simulation. Therefore, we developed bio-inspired simulation robots with Chrono, an open-source, high-fidelity multi-body dynamics engine (Mazhar et al., 2013; Tasora et al., 2015).

Using both physics-based modeling and simulation, we obtain a better understanding of the strenuous behaviors to escape the local energy basin and draw solid conclusions from model analysis and simulation results, which informed strategies to enhance robot control and design.

1.2 Background

1.2.1 Distinct locomotor challenges abstracted from complex terrain

In complex environments, animals employ a variety of locomotor modes, such as walking, running, crawling, climbing, flying, swimming, and jumping, often transitioning between them as needed. Similarly, to search and rescue a trapped person in earthquake rubble, the legged robots must be versatile, transitioning across various locomotor modes such as rolling, walking, bridging, and climbing (**Figure 2**). However, despite significant advancements in robot design, actuation, and control for multi-modal locomotion (Lock et al., 2013), current robots still struggle with these challenging tasks.

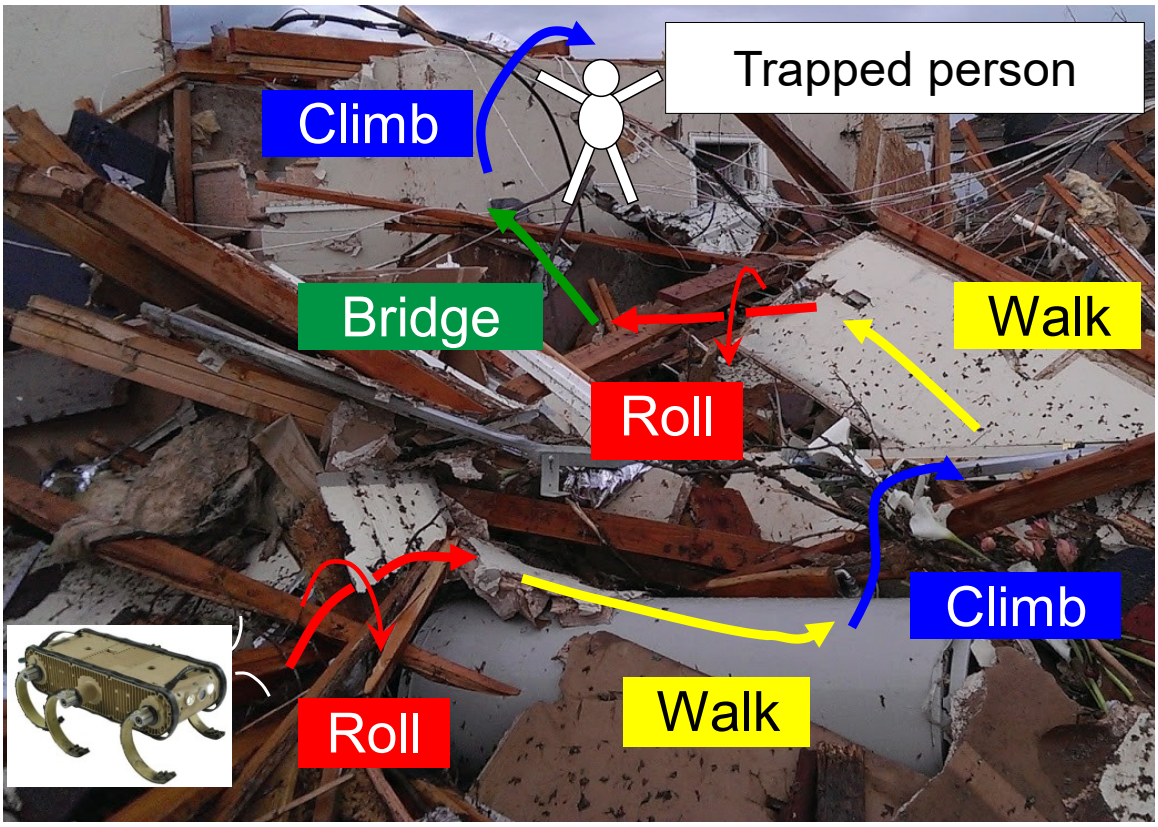

Figure 2. A schematic representation of a legged robot's locomotion during search and rescue in earthquake rubble. Reproduced from (Othayoth et al., 2020).

The discoid cockroach can naturally traverse complex terrain, such as cluttered vegetation in forest (**Figure 3**A). Its capability has inspired our research, allowing us to understand from it and apply those insights to robotic designs. To begin to understand complex physical interaction during locomotion in nature, we simplified complex 3-D terrains by viewing them as a collection of diverse, large obstacles (**Figure 3**B). This allowed us to break down the overall movement into a combination of distinct locomotor challenges such as compliant beams (Othayoth et al., 2020; Wang et al., 2022), rigid pillars (Han et al., 2021), gaps (Gart et al., 2018), and bumps (Gart and Li, 2018). The discoid cockroach transitions between them for traversal (Othayoth et al., 2021) (**Figure**

3C). In addition, given that animals and robots frequently flip over when traversing large obstacles (Li et al., 2015; Li et al., 2017), we also explored the self-righting behavior.

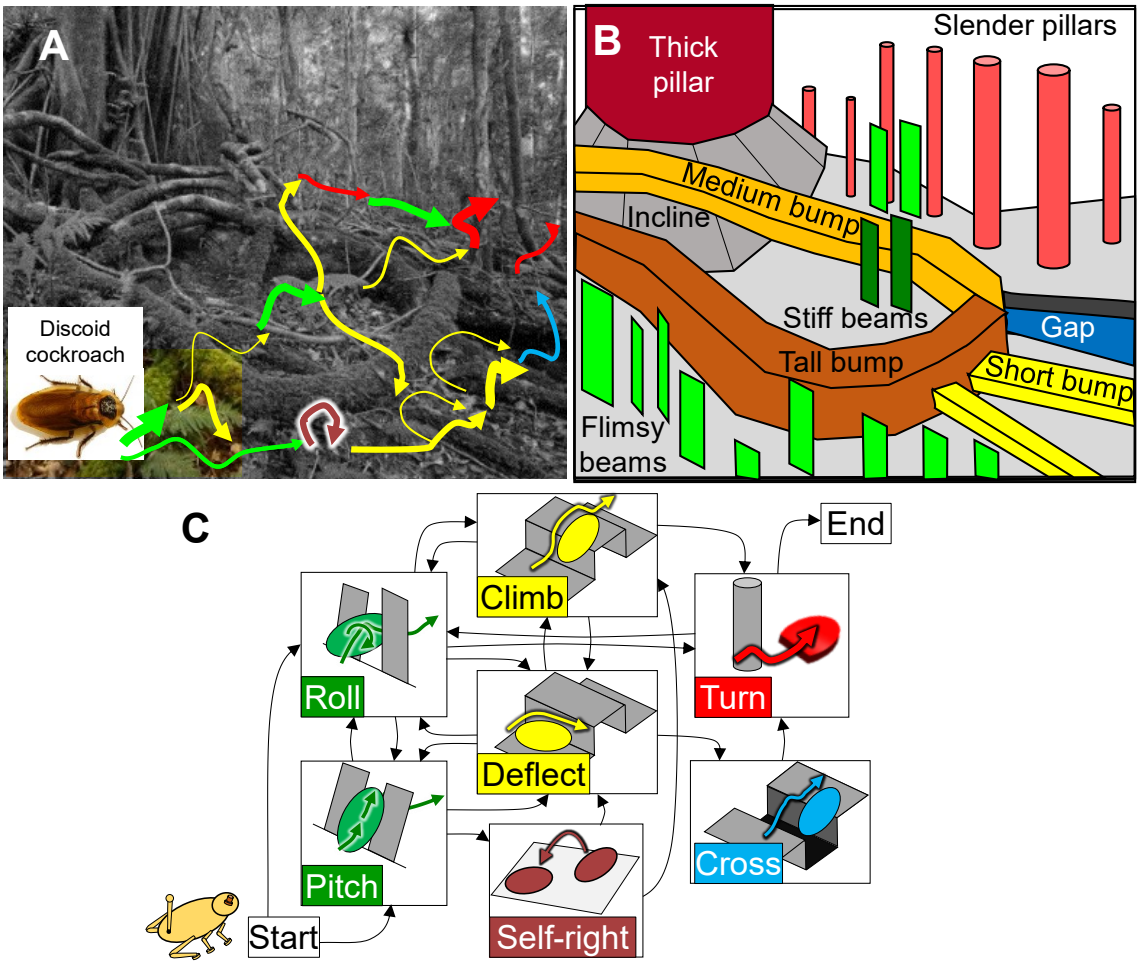

Figure 3 Transitions between locomotor challenges to avoid and traverse obstacles. (A) Envisioned capability of discoid cockroach traversing complex environments with many obstacles as large as itself. (B) Abstracted diverse large obstacles from complex environments. (C) Envisioned multi-pathway locomotor transitions. Reproduced from (Othayoth et al., 2021).

1.2.2 Potential energy basins in terrains can cause animals/robots to get stuck, making locomotion strenuous

To study the transitions between locomotor modes, a potential energy landscape framework was employed (Othayoth et al., 2020). Research discovered that when animals and robots traverse through complex 3-D terrains, their locomotor transitions correspond to the crossing of barriers on this energy landscape.

During traversal, animals and robots could get stuck in a stereotype locomotor mode. Analyzed from a potential energy landscape perspective, it is because that the system is attracted to the landscape basin separated by potential energy barriers (Othayoth et al., 2021). Escaping this basin presents a challenge as it requires overcoming an energy barrier (**Figure 4**A). To overcome this challenge, one strategy involves altering the morphology of animals or robots, which has the potential to reshape the energy landscape and, in turn, reduce or even eliminate the energy basin. For instance, using a streamlined rounded shell allows both the cockroach and robot to traverse through pillars or cluttered beams more effectively (Han et al., 2021; Li et al., 2015), reducing the chances of getting stuck compared to a rectangle shell. Another strategy is to leverage kinematic energy fluctuations to surpass the energy barrier. For instance, during beam traversal and ground self-righting, the robot would become stuck in an energy basin. Utilizing kinetic energy fluctuation from oscillatory self-propulsion, the system could stochastically transition from one basin to another (**Figure 4**). In beam traversal, this means transitioning from pitch mode to roll mode, and in ground self-righting, it is the transition from an upside-down position to an upright pose (Othayoth and Li, 2021; Othayoth et al., 2020).

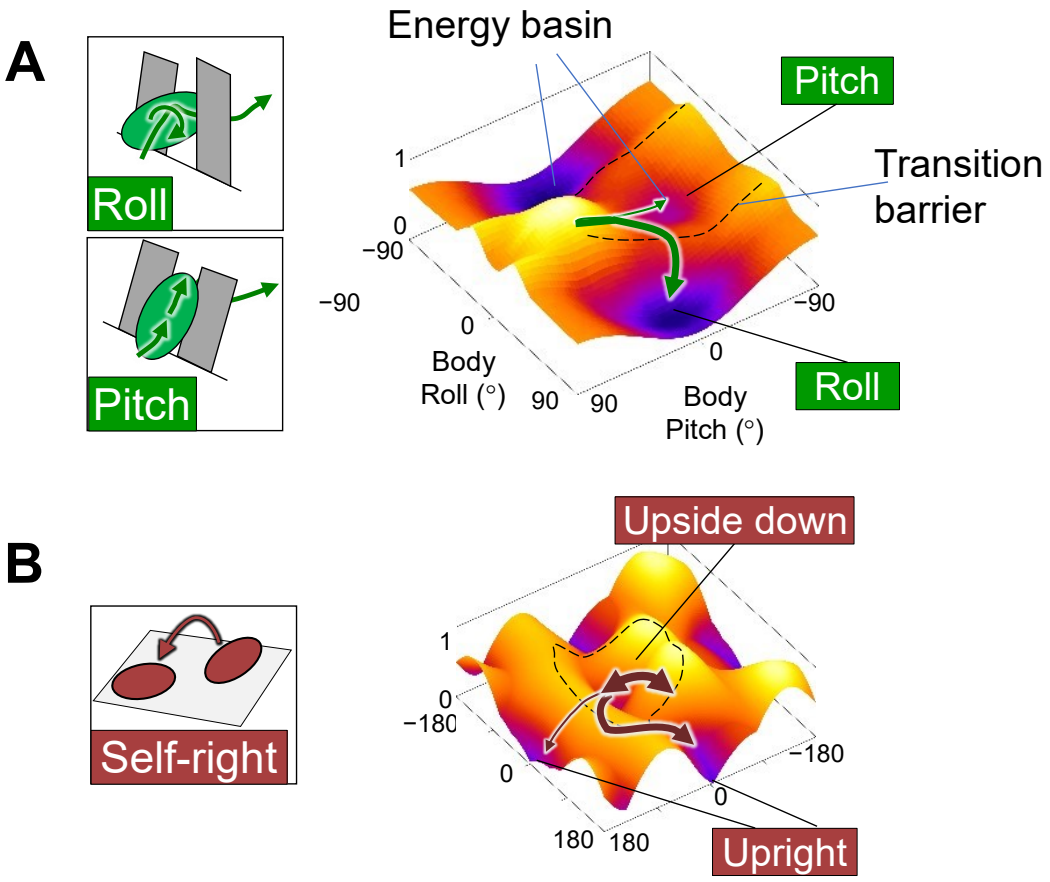

Figure 4 Locomotor transitions on potential energy landscapes. (A) In beam traversal, this system transitions from pitch mode to roll mode. (B) In ground self-righting, the system transitions from an upside-down position to an upright pose. Reproduced from (Othayoth et al., 2021).

However, relying solely on these strategies did not entirely capture locomotion mechanism of cockroaches. For instance, a self-propelled robot equipped with a rounded shell could roll to traverse beams narrower than their body width (Li et al., 2015). However, the success rate was lower than that of animals, and the robot frequently flipped upside down (**Figure 5**). While animals could traverse beams with lateral spacing at just 42% of their body width, robots struggled with beams only slightly narrower than their body width (83% of body width) (Li et al., 2015). Regarding self-righting, even with added mass to

generate a lager lateral kinematic energy fluctuation, the robot often struggled to self-right and frequently failed, especially when the wing opening amplitude was insufficient (Othayoth and Li, 2021).

Inspired by the remarkable traversal and quick self-righting abilities of animals, we began to uncover underlying mechanisms to escape energy basins beyond just stochastic kinematic energy fluctuations. In Chapter 2-4, we discuss more strategies to overcome energy barrier during the strenuous ground self-righting and the cluttered beam traversal. In Chapter 2, we discuss how randomness in wing and leg coordination facilitates the robot in overcoming the energy barrier to self-right. In Chapter 3, by using a template model, we reveal the mechanism of wing-leg self-righting and show that good wing-leg coordination can accumulate more mechanical energy to overcome the energy barrier. This model also aids in robot design to reduce the energy barrier, and model-based feedback control further enhances self-righting performance. In Chapter 4, we demonstrate that sensory force feedback facilitates the robot in better understanding environmental physics and traversing cluttered beam obstacles.

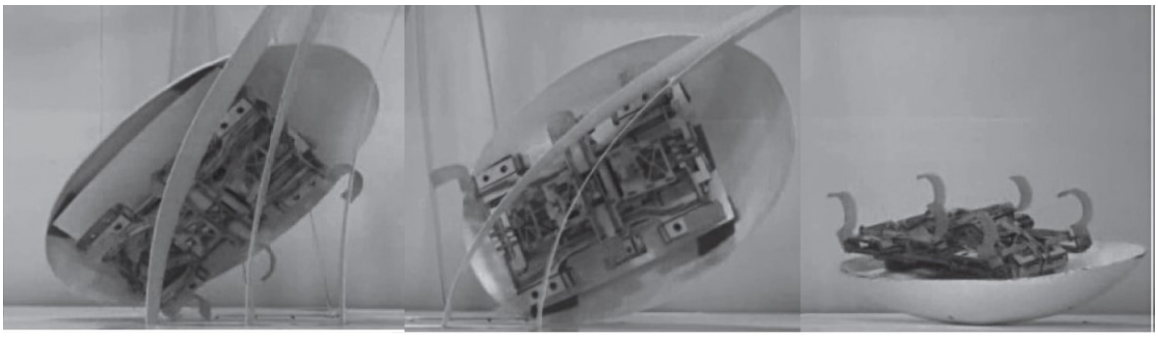

Figure 5 A small legged robot with a cockroach-inspired shell can traverse cluttered obstacles but struggles to self-right when flipped over. Reproduced from (Li et al., 2017).

1.2.3 Wing-assisted ground self-righting

As the cockroach traversed challenging terrain, it occasionally encountered instability that caused it to flip over. In such situations, the cockroach was consistently able to self-right itself and resume its movement.

Researchers observed that discoid cockroaches employ diverse strategies for self-righting on flat ground. These strategies include utilizing their wings against the ground (winged self-righting) and leveraging their legs to push off the ground (legged self-righting) (Li et al., 2019b). The focus of this particular study is on winged self-righting, which had previously been investigated using a simplified robotic model and a basic physics model (Li et al., 2016).

A closer study of the self-righting process revealed that the fluctuation of kinetic energy generated by this leg movement actually assists the cockroach and robot in their self-righting efforts (Othayoth and Li, 2021). When sufficient energy is available, the mere act of wing-opening can successfully right the body. However, in instances when the wing opening speed is slow and wing opening angle is small, the process becomes more strenuous and requires the involvement of the legs for additional support. Consequently, both the wings and legs play roles in this self-righting strategy and the coordination between them could be important.

In previous study (Othayoth and Li, 2021), a winged robot reproduced the self-righting behavior observed in cockroaches. But the robot control is periodic and feedforward. However, real animal movement could exist randomness and feedback control. To further improve the self-righting performance of the winged robot, it is crucial to explore these factors and understand the coordination between wings and legs.

1.2.4 Cluttered beam obstacle traversal

In a previous investigation (Li et al., 2015), researchers studied the locomotive capabilities of cockroaches as they traversed through compliant beams with gaps narrower than their body width.

This initial study uncovered that cockroaches employ various modes of locomotion in beam traversal, such as climbing up the beams, rolling between beam gaps, pushing against the beams, falling forward, or moving laterally. Building on these findings, a subsequent study employed a robotic system to further investigate locomotion (Othayoth et al., 2020). The robotic physical modeling showed that the kinetic energy fluctuation due to body oscillation from self-propulsion can assist in overcoming the potential energy barrier. However, it was noted that the animal could traverse even when the potential energy barrier was larger than the kinetic energy fluctuation. To answer this, further studies were conducted to understand if and how the cockroach actively adjusts to traverse through cluttered beams (Wang et al., 2022). When maneuvering, the cockroach consistently bent its head and abdomen, reduced hindleg sprawl, and lowered one hindleg while raising the other. These behaviors were not observed when the animal ran on a flat surface. These results indicate that incorporating these active adjustments could enhance the traversal capabilities of earlier open-loop control robots.

1.2.5 Template model for analyzing complex locomotion dynamics

Locomotion dynamics, whether in animals or robots, arise from complex interactions with their surrounding environment. These interactions are usually non-linear, high-dimensional, and coupled. To study it, we can use simple models, called templates,

to resolve the redundancy of multiple legs, joints, and muscles/motors by identifying underlying mechanisms. A template is the simplest dynamical model with the least number of components and degrees of freedom to realize the most fundamental dynamics of a targeted locomotor behavior (Full and Koditschek, 1999). Template models simplify the study of locomotion by reducing the complexity of movements in organisms, focusing on essential behaviors and ignoring redundant details like multiple legs and joints. They serve as a minimal framework to develop control strategies, which are then tested against detailed "anchor models" incorporating specific biological and mechanical details.

Templates have been developed for walking (Cavagna et al., 1977), upright (Blickhan and Full, 1993) and sprawled (Schmitt and Holmes, 2000) running, climbing (Goldman et al., 2006), tail-assisted aerial self-righting (Libby et al., 2016), multi-legged ground self-righting (Saranli et al., 2004), and dynamic large gap traversal (Gart et al., 2018). Although they lose details, templates are quantitatively predictive and useful for not only explaining biological phenomena but also predicting design, control, and planning for robots (Holmes et al., 2006).

1.2 Research questions and objectives

To enhance our understanding of animal locomotion across complex terrains, researchers identified specific locomotor challenges within these environments (Sec. 1.2.1) and developed biological and robotic modeling systems for investigation correspondingly (Gart and Li, 2018; Gart et al., 2018; Han et al., 2021; Othayoth et al., 2020; Wang et al., 2022).

In the present research, researcher has already developed corresponding physical robots for different challenges (**Figure 6**). This approach simplified the system,

highlighting the essential features of traversal to uncover the underlying mechanisms. However, in many previous studies, bio-inspired robots operated mostly on open-loop control, leading them to frequently become trapped by obstacles. To further uncover underlying mechanisms to escape energy basins, particularly in a strenuous condition, we employed physics-based simulations to systematically test hypotheses that emerged from both animal and robotic experiments (**Figure 6**).

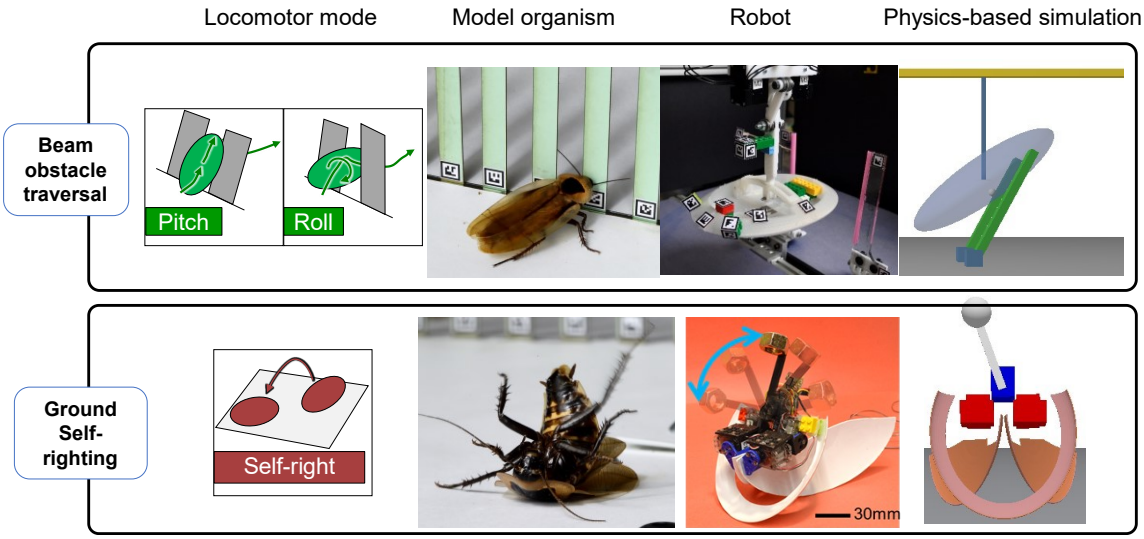

Figure 6 Exploring the mechanisms of locomotor mode transitions in beam obstacle traversal and ground self-righting through animal studies, robotic experiments, and physics-based simulations. Images courtesy of Will Kirk and Ratan Othayoth.

1.3.1 Influence of randomness in appendage coordination on self-righting

Randomness, originating from environmental variability (Bovet and Benhamou, 1988) and internal organismal noise in biological systems (Faisal et al., 2008; Van Beers et al., 2002), is similarly present in man-made systems due to sensor inaccuracies and environmental factors (Byl and Tedrake, 2009; How and Tillerson, 2001). This

randomness generally impairs system performance, affecting stability in both biological (Roos and Dingwell, 2010) and technological locomotion, and poses challenges to control mechanisms (Nilsson et al., 1998). Effective mitigation of randomness is usually essential for efficient movement. Although typically considered as a nuisance, randomness can be useful for locomotor systems (Bartumeus, 2009; Moore et al., 2017; Reynolds and Rhodes, 2009; Sutantyo et al., 2010).For instance, its inherent unpredictability can be strategically employed to facilitate an escape from undesired states, introducing dynamic variability that enhances adaptability in these systems. This aspect of randomness, leveraging its potential to disrupt predictable patterns such as limit cycles that may otherwise trap motion in a repetitive loop.

Randomness is also observed in neural control and motor patterns of self-righting. Unlike the more rhythmic neural signals observed in walking and running, self-righting exhibits considerably greater randomness (Camhi, 1977; Delcomyn, 1987; Reingold and Camhi, 1977; Sherman et al., 1977). Additionally, our experiments have revealed a notable variation in the oscillation periods of both wing and leg movements during self-righting.

For ground self-righting, earlier robots utilized feedforward control to manage wing opening and closing, as well as leg oscillation, based on a periodic actuation profile (**Figure 7**), which proved to be a strenuous task (Othayoth and Li, 2021). When the wings are open, the head and two wings form a triangular contact with the ground, creating a potential energy basin. Leg flailing generates kinetic energy fluctuations, aiding the robot in escaping the basin. However, the coordination between the wing and leg is predefined by periodic actuation, causing the robot to repeatedly perform the same motion.

To enhance the robot's self-righting performance, we drew inspiration from animals. Considering the significant randomness observed in insects' neural control of self-righting compared to walking and running, it appears to be an intentional strategy to incorporate randomness into the self-righting motion. Thus, our primary objective is to investigate whether this large randomness in wing and leg motion is beneficial to self-righting, and if so, under what circumstances. We hypothesized that this randomness in appendage coordination might aid in the strenuous ground self-righting. We then developed physics-based simulations to investigate this theory, as detailed in Chapter 2. By testing this hypothesis, we hope to advance our understanding of the role of randomness in locomotor control and facilitate the development of more effective control strategies for artificial systems.

1.3.2 Coordination between wings and legs in roach-inspired robots

In the robot's design, with its open-loop setup and a periodic actuation profile, the opening of the wings elevates the body's center of mass, producing upward kinematic energy; the leg oscillation shifts the center of mass, generating lateral kinematic energy (**Figure 7**). These effects are coupled in the dynamic system. The robot works well when the wing opening amplitude and the leg oscillation amplitude are sufficiently large. However, when they are insufficient, the robot falls back to the ground and continues this motion repeatedly. In this process, the mechanical energy is dissipated, and the system could not overcome the energy barrier.

To better use the energy input from wing and leg, we need to understand dynamics of the system and identify a good coordination between them. To achieve this, we aim to develop a physics-based model that can explore the relationship between wing and leg coordination (**Figure 7**). By gaining insight into the underlying principles governing self-

righting behavior, we hope to identify generalizable strategies that can be applied to a variety of robotic systems, regardless of their specific parameters.

In addition, we hope this model could aid in robot design to reduce the energy barrier, and model-based feedback control further enhances self-righting performance.

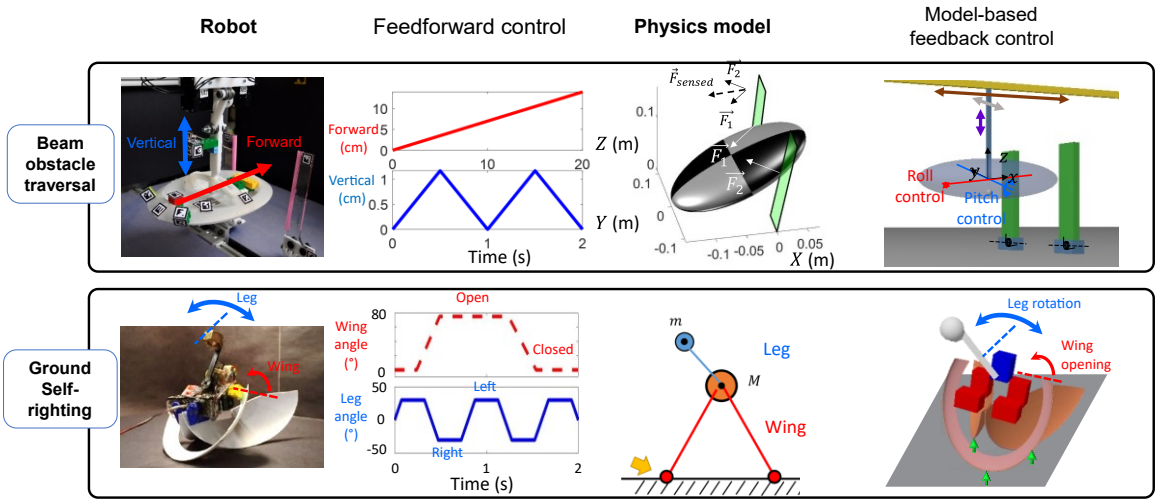

Figure 7 Study on beam obstacle traversal and ground self-righting: The prior feedforward control constrained the robot's performance. Leveraging a physics model, the present model-based feedback control has enhanced performance, which was confirmed through simulation. Images courtesy of Ratan Othayoth.

1.3.3 Cluttered beam traversal with physical interaction

In addition to randomness, animals also leverage abundant sensory information from interacting with their surroundings when escaping from a trapped state. In contrast, our current robot did not utilize this information and only performed feedforward control (Li et al., 2015; Li et al., 2017; Othayoth and Li, 2021; Othayoth et al., 2020) (**Figure 7**). Given this, we hypothesized that integrating sensory feedback could significantly improve the robot's capabilities.

When cockroaches are traversing beams with varying stiffness, they use different strategies. For flimsy beams, the animal typically pitches its body upwards to push over, while for stiff beams, it tends to roll into a gap for maneuvering. Given that animals are unlikely to discern beam stiffness visually, they do not preselect a traversal strategy. This suggests that their approach is influenced by their physical interaction with the beams. We hypothesize that sensory feedback from the body's contact with obstacles aids traversal through feedback control.

To integrate sensory feedback into our earlier open-loop control, transitioning to a sensory feedback control system (**Figure 7**), understanding system dynamics through a physics model is essential. Therefore, we crafted a template model for the system, delved into the mechanisms, and implemented sensory feedback control for enhanced performance (**Figure 7**), as detailed in Chapters 4.

Chapter 2

Randomness in appendage coordination facilitates strenuous ground self-righting

This chapter was previously published as an article entitled *Randomness in appendage coordination facilitates strenuous ground self-righting*, authored by Qihan Xuan and Chen Li, in *Bioinspiration and Biomimetics* (Xuan and Li, 2020a). We re-used the article in this chapter with slight changes of the format under CC BY 4.0 and with permissions from both authors.

2.1 Author contributions

Qihan Xuan designed study, developed simulation, performed experiments, analyzed data, and wrote the paper; Chen Li designed and oversaw study and revised the paper.

2.2 Acknowledgements

We thank Ratan Othayoth, Shai Revzen, Noah Cowan, Simon Sponberg, Greg Chirikjian, Yang Ding, Avanti Athreya, and three anonymous reviewers for discussion and suggestions; Ratan Othayoth for providing data of physical robot experiments; Soowon Kim for early simulation development; Arman Pazouki and Dan Negrut for technical assistance on Chrono; and Zhiyi Ren for measuring Young's modulus.

This work was supported by an Army Research Office Young Investigator award (grant # W911NF-17-1-0346), a Burroughs Wellcome Fund Career Award at the Scientific

Interface, and The Johns Hopkins University Whiting School of Engineering start-up funds to C.L.

2.3 Summary

Randomness is common in biological and artificial systems, resulting either from stochasticity of the environment or noise in organisms or devices themselves. In locomotor control, randomness is typically considered a nuisance. For example, during dynamic walking, randomness in stochastic terrain leads to metastable dynamics, which must be mitigated to stabilize the system around limit cycles. Here, we studied whether randomness in motion is beneficial for strenuous locomotor tasks. Our study used robotic simulation modeling of strenuous, leg-assisted, winged ground self-righting observed in cockroaches, in which unusually large randomness in wing and leg motions is present. We developed a simplified simulation robot capable of generating similar self-righting behavior and varied the randomness level in wing-leg coordination. During each wing opening attempt, the more randomness added to the time delay between wing opening and leg swinging, the more likely it was for the naive robot (which did not know what coordination is best) to self-right within a finite time. Wing-leg coordination, measured by the phase between wing and leg oscillations, had a crucial impact on self-righting outcome. Without randomness, periodic wing and leg oscillations often limited the system to visit a few bad phases, leading to failure to escape from the metastable state. With randomness, the system explored phases thoroughly and had a better chance of encountering good phases to self-right. Our study complements previous work by demonstrating that randomness helps destabilize locomotor systems from being trapped in undesired metastable states, a situation common in strenuous locomotion.

2.4 Introduction

Randomness is common in biological systems, resulting either from stochasticity of the environment (Bovet and Benhamou, 1988) or noise in organisms themselves (for example, in sensing, information processing, and movement) (Faisal et al., 2008; Van Beers et al., 2002). Randomness is also common in man-made dynamical systems, which can come from sensors (How and Tillerson, 2001), information transfer (Nilsson et al., 1998), motor control (Ho, 1997), mechanical properties (Marti, 2003), and the environment (Byl and Tedrake, 2009). Typically, randomness degrades system performance and needs to be mitigated. For example, stochasticity in the terrain (surface slope variation) can drift the limit cycles of a passive dynamic walker, breaking the dynamic stability found in idealized, flat terrain and leading to metastable (locally attractive) behaviors (Byl and Tedrake, 2009). Neuromuscular noise also decreases walking stability (Roos and Dingwell, 2010). Sensory noise can overwhelm weak signals (Faisal et al., 2008) and compromise motion planning (How and Tillerson, 2001; Osborne et al., 2005). Inherent random time delay in communication and computation degrades the performance of control systems (Nilsson et al., 1998). All these problems can pose challenges to locomotion.

Although typically considered as a nuisance, randomness can be useful for both biological and artificial locomotor systems. Over large spatiotemporal scales, many animals move in stochastic trajectories (e.g., Lévy flight (Bénichou et al., 2005; Reynolds and Rhodes, 2009), correlated random walk (Bergman et al., 2000)) which increases the efficiency of searching for resources and mates (Reynolds and Rhodes, 2009) and decreases the risk of encountering predators (Bergman et al., 2000) or conspecifics that compete for the same resources (Reynolds and Rhodes, 2009). Over smaller spatiotemporal scales, stochasticity in the velocity of prey animals increases the

probability of avoiding ballistic interception by predators (Moore et al., 2017). In biological sensing, weak periodical signals can be amplified via stochastic resonance with noise (under a threshold) (McDonnell and Ward, 2011; Wiesenfeld and Moss, 1995). Inspired by these biological systems, randomness has been leveraged to improve the performance of artificial systems, such as random search for optimization (Sutantyo et al., 2010), weak signal detection using stochastic resonance (Kurita et al., 2013) or resonant trapping (Gammaitoni and Bulsara, 2002).

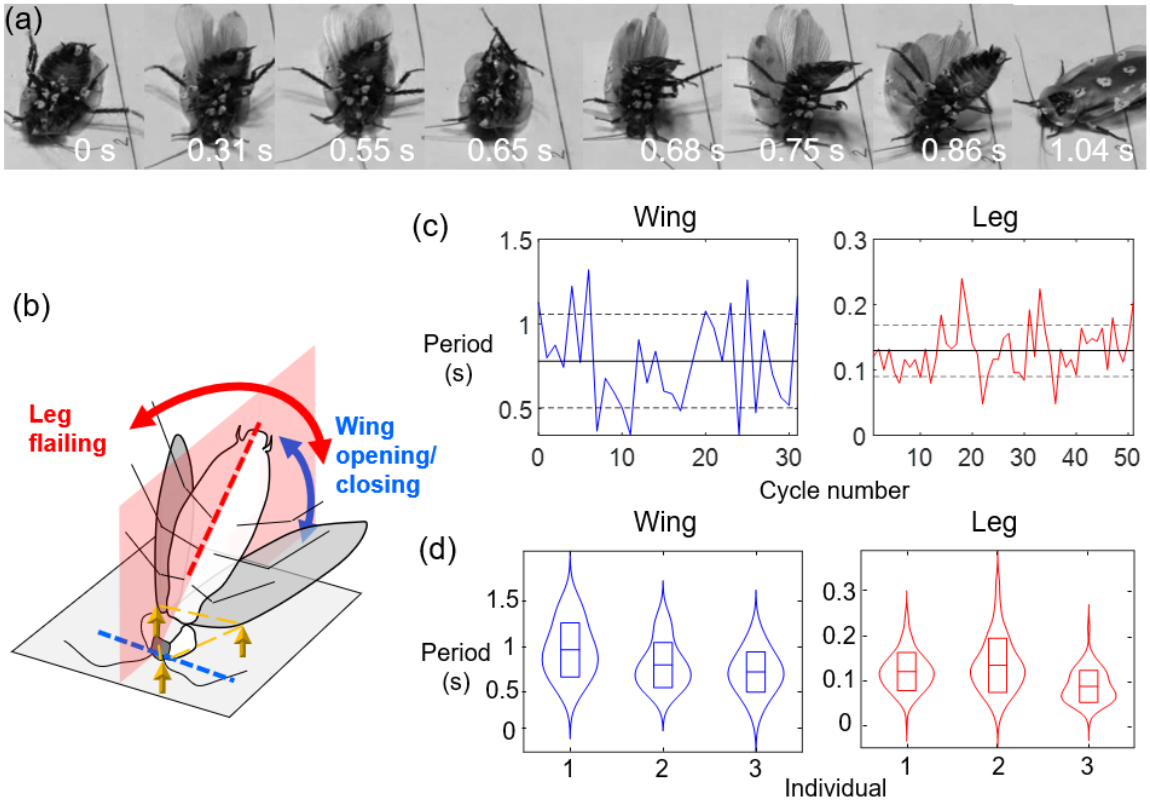

Figure 8. Discoid cockroach's strenuous, leg-assisted, winged ground self-righting. (a) Snapshots of a discoid cockroach self-righting. In this trial, the animal succeeds after two attempts of wing opening. (b) Schematic of animal in metastable state. Yellow arrows and triangle show head and two wings in contact with ground, forming a triangular base of support. Blue and red arrows show wing and leg oscillations. Blue and red dashed lines show approximate axes of rotation of body during wing oscillation and legs during flailing. Translucent red plane shows sagittal

plane. (c) Left: periods of wing oscillation in a trial with 32 cycles. Right: periods of a hind leg's oscillation in a trial with 51 cycles. Solid and dashed lines show mean ± s.d. (d) Violin plots of wing and leg oscillation periods for three individuals (n = 3 trials for each; 679 leg cycles and 59 wing cycles in total). Local width of graph shows the frequency of data along each value of y-axis. Inner rectangle shows mean ± s.d.

Inspired by these ideas, here we studied whether randomness in motion is beneficial for strenuous locomotor tasks. Our study was motivated by recent observation of the discoid cockroach (*Blaberus discoidalis*) self-righting from an upside-down orientation on a level, flat surface (**Figure 8** (a), Movie 1) (Li et al., 2019a). One strategy of the animal is to push both its wings together against the ground in an attempt to pitch over its head (**Figure 8**(b), blue arrow) (Li et al., 2019a). However, such a somersault has a large potential energy barrier, which the animal can rarely generate sufficient kinetic energy to overcome (Othayoth et al., 2017). Thus, the animal is often trapped in a metastable state (Hanggi, 1986), where its center of mass projection falls within a triangular base of support formed by the head and outer edges of two wings in contact with the ground (**Figure 8**(b), yellow arrows and triangle) (Othayoth et al., 2017). Meanwhile, the animal often flails its legs laterally (**Figure 8**(b), red arrow) and flexes and twists its abdomen (Li et al., 2019a). These motions induce kinetic energy fluctuation to perturb the body to roll, which overcomes a smaller potential energy barrier (Othayoth et al., 2017). Thus, when the animal does eventually self-right, often after multiple wing opening attempts, it almost always rolls to one side (Li et al., 2019a).

During each wing opening attempt, while mechanical energy is injected by wing and leg motions, it is dissipated via collision and friction against the ground and internal collision (wings and legs stop moving relative to the body). Thus, coordination between wing and leg oscillations may be critical for self-righting. Curiously, compared to cockroach

walking (Watson and Ritzmann, 1997) and running (Full and Tu, 1990), in strenuous, leg-assisted, winged self-righting, both wing and leg oscillations are much less periodic, with large randomness present in their amplitudes, directions, speeds, and periods. For example, the periods of leg and wing oscillations are highly variable, with a coefficient of variation (standard deviation divided by mean) of C_v = 25% for leg and C_v = 36% for wing (**Figure 8**(c, d)). In addition, the animal appears to randomly flex and twist its abdomen and scrape or hit its flailing legs against the ground by chance (Li et al., 2019a). All these large random motions are absent during walking and running.

We hypothesize that the unusually large randomness in motions is beneficial for strenuous, leg-assisted, winged ground self-righting, by allowing random search in appendage configuration space to find an appropriate appendage coordination. We chose to focus on leg-assisted, winged self-righting among the diverse strategies observed in the cockroaches (Li et al., 2019a), because it is a strenuous behavior where coordination between different appendages is likely to be critical. As described above, this self-righting behavior is complex, with the head, two wings, multiple legs, and abdomen all playing a role (Li et al., 2019a). Studying randomness in the coordination of all these body parts together poses a significant challenge. As a first step, we focused on the randomness in the coordination between wings and legs.

To test our hypothesis, we took an approach of robotic modeling and created a simplified computational model—a cockroach-inspired simulation robot—to perform systematic in silico experiments (**Figure 9**(b)). We chose to use a simulation robot here because it allowed precise control of randomness and large-scale, systematic parameter variation not practical in physical experiments. Our simulation robot followed the design and control of a recent physical robot that we developed to understand the role of kinetic energy fluctuation in leg-assisted, winged self-righting (Othayoth et al., 2017). The robot

has two wings, a pendulum “leg”, and a body with a head that protrudes beyond the anterior end of the wings (mimicking the cockroach’s head). The two wings open and close symmetrically, and the single leg swings side to side to generate lateral perturbation. Although these motions are much simplified relative to the animal’s, they can generate body motions representative of the animal’s strenuous self-righting behavior that we are interested in (Othayoth et al., 2017), while also providing the simplest model system, with only two degrees of freedom in actuation.

As a first step to understand the role of randomness in wing-leg coordination, we added Gaussian noise of variable levels to wing oscillation period (**Figure 9**(c)). During each wing oscillation cycle, between wing opening and closing, the wings are held open or closed for some time (Movie 1). We chose to only add noise to the time that wings are held closed, so that other parameters (wing opening/closing speed, wing opening amplitudes, wing opening time) were kept constant. In addition, we varied wing opening and leg flailing amplitudes (**Figure 13**) to study the effect of randomness over a wide range of parameter space. Then, we studied how randomness in the phase between wing and leg oscillations affected self-righting outcome of a single wing opening attempt, and we used this single attempt phase map (**Figure 14**) to predict the outcome of multiple attempts (**Figure 15**). These analyses helped reveal how randomness in phase was beneficial for self-righting.

We emphasize that we deliberately designed and controlled our robot to serve as a physical model to generate strenuous self-righting similar to the animal’s, so that we could study appendage coordination. Our goal is not to simply achieve successful self-righting, which can be done in many other, and often simpler, ways in a robot (for a review, see (Li et al., 2017)). For example, a previous cockroach-inspired robot with wings and no legs (Li et al., 2017) was capable of self-righting by a somersault using wings only. It could

also open the left and right wings asymmetrically to roll the body to self-right. In both cases, the wings opened sufficiently to generate sufficient rotational kinetic energy to overcome the potential energy barrier. By contrast, the discoid cockroach's wing opening alone was rarely sufficient (Othayoth et al., 2017) and must be supplemented by the perturbating motions of the legs and abdomen. In addition, this previous robot did not have a protruding head that adds to the potential energy barrier and makes self-righting strenuous. Thus, although this previous robot self-rights easily, it is not suitable for studying the behavior we are interested in here.

2.5 Methods

2.5.1 Design and actuation of simulation robot

Our simulation robot was created using Chrono, an open-source, high-fidelity, multi-body dynamics engine (Mazhar et al., 2013; Tasora et al., 2015). Besides the head, two wings, single pendulum leg (consisting of a lightweight rod and an added mass), the robot also had five cuboidal motors (**Figure 9**(a); see mass distribution in **Table 1**). The wings and head were cut from a thin ellipsoidal shell. We carefully matched the simulation robot's geometry and mass distribution. We created CAD models of these parts in SolidWorks and assembled them using the relative position and orientation of each part measured from the physical robot. We then exported the assembled CAD model into Chrono to create the simulation robot. We rounded the edges of each part to make the contact forces change more smoothly in simulation and considering that we used the Hertzian contact model (see below) which is developed for rounded shapes.

Table 1. Mass distribution of the simulation robot.

Component	Mass (g)

Head	13.4
Leg rod	4.3
Leg added mass	51.5
Leg motor	28.6
Two wings	57.4
Two wing pitch motors	56.0
Two wing roll motors	48.8
Total	260

Each wing could both pitch and roll relative to the body, actuated by two motors with orthogonal axes of rotation (**Figure 9**(a)). We defined wing pitch and roll (**Figure 9**(b)) as the angles rotated by the pitch motors (3, 4) and roll motors (1, 2). Because the cockroach's two wings open and close together during self-righting, we controlled the robot's two wings to move symmetrically. We also constrained wing pitch and roll angles to always be the same to simplify experiments and analysis. Thus, wings motion was effectively one degree of freedom, which we described with wing angle θ_w (**Figure 9**(b)). The robot's pendulum leg was actuated by a separate motor (**Figure 9**(a), motor 5). We defined leg angle θ_l as the angle between the pendulum and body midline (**Figure 9**(b)).

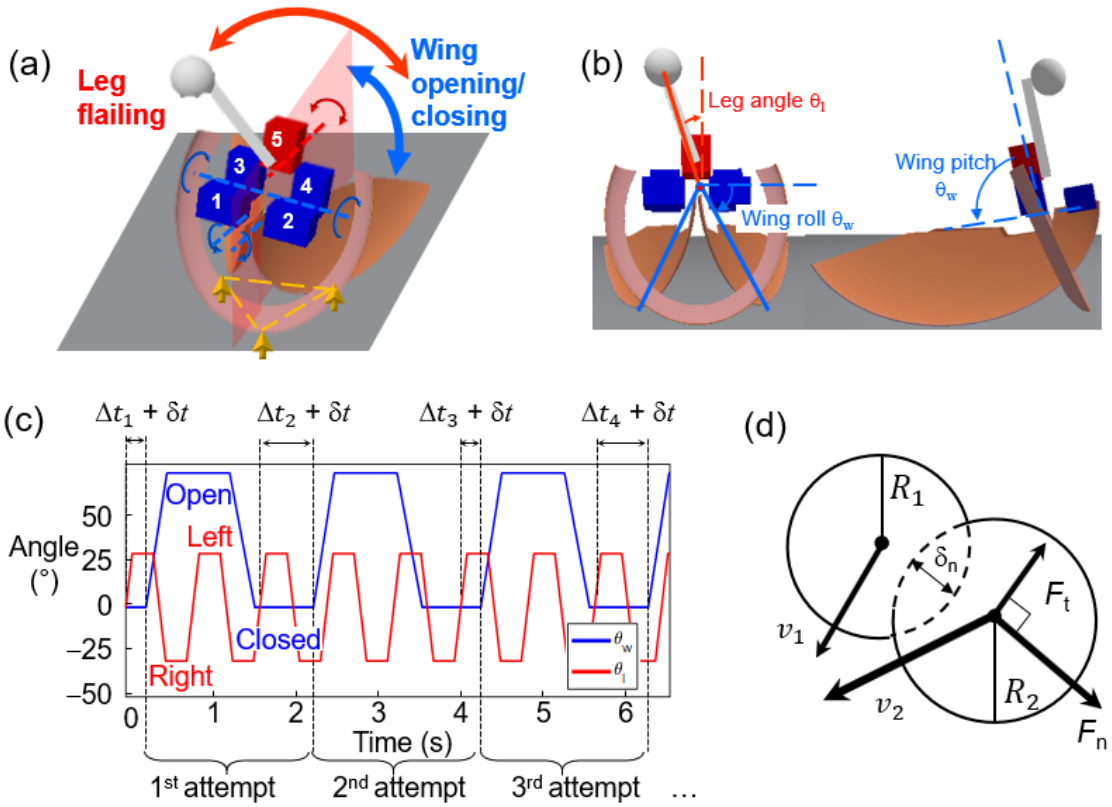

Figure 9. Cockroach-inspired, leg-assisted, winged self-righting simulation robot. (a) Simulation robot with a head, two wings, five motors, and a pendulum leg, in metastable state. Yellow arrows and triangle show head and two wings in contact with ground, forming a triangular base of support. Red and blue arrows show wing and leg oscillations. Translucent red plane shows sagittal plane. (b) Frontal and side views of simulation robot to define leg angle (red) as well as wing roll and wing pitch (blue). (c) Actuation profiles of wings (blue) and leg (red). Δt_i is the time delay of the i^{th} wing opening attempt, defined as the time interval between wing opening moment and the start of the preceding leg oscillation. A Gaussian noise δt is added to Δt in simulation experiments with randomness. (d) Hertzian contact model used in multi-body dynamics simulation. δ_n is virtual overlap (deformation) between two rigid bodies. F_n and F_t are normal and tangential contact forces. R_1 and R_2 are local radii of curvature at contact.

Our physical robot's wing and leg oscillations were controlled using simple actuation profiles, with actuation parameters deliberately chosen to generate strenuous leg-assisted, winged self-righting behavior similar to the animal's (Othayoth et al., 2017). Thus, we simply designed the simulation robot's wing and leg actuation profiles (**Figure 9**(c)) to approximate those of the physical robot and used similar actuation parameters. For both the physical and simulation robots, wing and leg oscillation periods were T_w = 2 s and T_l = 0.8 s (except in phase-based prediction where we varied T_w and T_l, see Section 2.6.6). T_w was chosen to be greater than T_l as observed in the animal. Although there may be an optimal frequency (close to the natural frequency in the body roll direction) for leg flailing to induce resonance, we did not study it here because we focused on the randomness in wing-leg coordination. For the simulation robot, wing opening and closing speeds were 300 °/s and 250 °/s, and the time for the leg to move from one side to the other was t_l = 0.15 s. Thus, the angular speed of leg rotation was $2\theta_l/t_l$. Note that these were slightly different from the physical robot, whose values were 266 ± 19 °/s, 375 ± 14 °/s, and 0.143 ± 0.038 s. In particular, the slower wing closing speed in simulation was chosen to better match the physical robot. The physical robot's thin wings and head were deformable, and its 3-D printed plastic joints between the body and wings had a slight give under load, both of which quickly damped out body oscillation on the ground after the wings closed. The simulation robot's thin wings and head were rigid, and slower wing closing reduced body oscillation and simulated this effect. In physical/simulation robot experiments, we defined the time interval between two consecutive instants when the wings began to open as one wing opening attempt.

2.5.2 Contact mechanics model

To solve for dynamics, we used the discrete-element method via penalty (DEM-P) in Chrono, which models contact by a viscoelastic force model (Fleischmann, 2015; Tasora et al., 2015) (**Figure 9**(d)):

$$\begin{cases} \boldsymbol{F}_n = f(\bar{R}, \delta_n)(k_n \boldsymbol{\delta}_n - \gamma_n \bar{m} \boldsymbol{v}_n) \\ \boldsymbol{F}_t = f(\bar{R}, \delta_n)(-k_t \boldsymbol{\delta}_t - \gamma_t \bar{m} \boldsymbol{v}_t) \end{cases} \quad (1)$$

where $\boldsymbol{\delta} = \boldsymbol{\delta}_n + \boldsymbol{\delta}_t$ is the displacement vector of the contact point between two bodies, which represents their overlap if no deformation occurs, and the subscripts "n" and "t" represent normal and tangent components, respectively. The scalars $m_1 m_2/(m_1 + m_2)$ and $\bar{R} = R_1 R_2/(R_1 + R_2)$ are the effective mass and effective radius of curvature of the two interacting bodies. The vector $v = \boldsymbol{v}_n + \boldsymbol{v}_t$ is the relative velocity between the two bodies. $k_n, k_t, \gamma_n, \gamma_t$ are the normal and tangential stiffness and damping co, and material properties (Young's modulus *E*, Poisson's ration ν, and coefficient of restitution CoR) of the two bodies. Assuming Coulomb friction (with coefficient μ), sliding happens if $|\boldsymbol{F}_t| > \mu|\boldsymbol{F}_n|$ and stops otherwise. During sliding, kinetic friction is set to be $|\boldsymbol{F}_t| = \mu|\boldsymbol{F}_n|$. Here we chose Hertzian contact theory (Ding et al., 2012; Popov, 2010), i.e., in Eqn. 1:

$$f(\bar{R}, \delta_n) = \sqrt{\bar{R}\delta_n} \quad (2)$$

2.5.3 Material property characterization

To validate our simulation robot, we performed experiments to characterize material properties for the physical robot (Othayoth et al., 2017). This is important because the viscoelastic model (Eqn. 1) includes Young's modulus *E*, coefficient of friction μ, coefficient of restitution CoR, and Poisson's ratio ν as parameters. In physical robot experiments, before self-righting, only the wings and head of the robot (made of

polystyrene) contact the ground (Othayoth et al., 2017). Thus, we measured or estimated the material property of polystyrene for model input.

To measure coefficient of friction, we set the physical robot upside down on a rigid plate with the sandpaper surface used in robot experiments (Othayoth et al., 2017). Then we slowly increased the slope angle α until the robot started to slip. The critical angle α_c was used to calculate the coefficient of friction via $\mu = \tan\alpha_c$. From this experiment (5 trials), $\mu = 1.00 \pm 0.04$ (mean $\pm$ s.d.). Thus, we used $\mu = 1$ in simulation.

To measure Young's modulus, we did extension experiments using an Instron universal testing machine (34TM-10, Norwood, MA, US). We tested three polystyrene beams with different thicknesses, with each beam tested five times. We found that $E = 0.78 \pm 0.04 \times 10^9$ Pa for polystyrene (mean $\pm$ s.d.). However, with such a high E, a simulation time step of $< 10^{-7}$ s was required for numerical convergence, leading to an impractical time to complete our simulation experiments (over one day to run 1 trial on a 3.4 GHz 16-core workstation). A common practical solution to this problem is to reduce Young's modulus in simulation so that numerical convergence can be achieved with a larger time step (Maladen et al., 2011; Pazouki et al., 2017; Tasora et al., 2015). We found that, with a sufficiently small simulation time step (10^{-5} s), simulation results were not sensitive to E within 10^5 Pa to 10^7 Pa (e.g., the measured self-righting time changed by less than 10%). Thus, we used a smaller $E = 1 \times 10^5$ Pa.

To obtain numerical convergence for this chosen E while keeping simulation time practical, we varied time step from 10^{-3} s to 10^{-7} s. We found that using a larger time step of 10^{-4} s only resulted in a small error from using a smaller time step of 10^{-6} s (e.g., pitch, roll, and yaw angles of the robot changed less than 0.2° over 10 seconds of simulation). In addition, it reduced simulation time to yield a practical time to complete our simulation

experiments (one day to run 1000 trials on a 3.4 GHz 16-core workstation). Thus, we used a time step of 10^{-4} s for all simulation experiments. The numerical convergence was not sensitive to other parameters (μ, ν, CoR), which only led to changes of smaller than an order of magnitude in the choice of time step.

In addition, we found that simulation results were insensitive to Poisson's ratio (e.g., pitch, roll, and yaw angles of the robot changed less than 0.5° over 10 seconds of simulation as ν varied from 0 to 0.5). Thus, we chose $\nu = 0.35$, close to that of polystyrene (Bangs Laboratories, 2015).

Because CoR was a function of the collision velocity, geometry, and material composition of both objects in contact (Ramírez et al., 1999), it was difficult to measure experimentally. We found that CoR had a small effect (e.g., self-righting time increased by 18.4% as CoR increased from 0 to 0.5). We chose CoR = 0.1 to achieve large dissipation in simulation to better match that the high damping of body oscillations of the physical robot on the ground after wings closed, as mentioned above.

2.5.4 Validation of simulation against physical robot experiments

We performed simulation experiments to verify that our simulation robot was reasonable in physics. In both physical and simulation robot experiments, we varied wing opening and leg oscillation amplitudes, θ_w and θ_l, and measured self-righting time. The physical robot had a naturally occurring randomness in wing oscillation period of $C_v = 1.3\%$. For the simulation robot, we added a randomness of $C_v = 2.9\%$ to wing oscillation period. This was set to be larger than that in the physical robot to account for other randomness in the system, such as randomness in θ_w and θ_l, leg actuation, and the environments. For both the simulation and physical robots, we performed five trials at each combination of θ_w and θ_l. We recorded the first 10 seconds of each trial. The 10 seconds time limit was

chosen to save simulation time, considering that in most trials, self-righting occurred within 10 seconds. If the robot could not self-right within 10 seconds, we defined it to have failed. For failed trials, we set self-righting time as 10 seconds. This was considering that, if we did not consider failed trials in averaging self-time, the few successful trials were not representative.

2.5.5 Randomness in simulation robot motion

To introduce randomness in wing oscillation period (and thus randomness in wing-leg coordination), we added Gaussian noise with variance σ^2 (using C++) to the time when wings are held closed. To isolate the effect of coordination, we chose to add randomness rather than vary T_w and T_l directly, because doing so would affect the mechanical energy injected by changing the speed and duration of motor actuation. To isolate the effect of randomness in actuation, we did not introduce noise in the mechanical system (e.g., morphology, physical property, the environment) that is inevitable in the physical robot and animal (see discussion in Section 2.7.2). For simulation experiments, we measured the level of randomness using coefficient of variation, C_v, defined as the ratio between standard deviation σ and leg period T_l. We chose to normalize σ by T_l because phase φ, which we used to measure wing-leg coordination, was normalized by T_l. To study the effect of randomness, we varied C_v (0%, 5%, 10%, 15%, 20%, and 25%) in simulation experiments. For each combination of θ_w (70°, 72°, 74°, 76°) and θ_l (20°, 30°, 40°, 50°) and a given C_v, we performed 40 simulation trials. This resulted in a total of 3840 trials.

2.5.6 Phase between wing and leg oscillations

Because we only added randomness to wing oscillation period while keeping everything else constant (Section 2.5.5), the only thing that changed was the phase between wing and leg oscillations at each wing opening attempt (**Figure 9**(c)). For each

wing opening attempt i, we defined the phase φ between wing and leg oscillations as the ratio of time delay Δt_i to leg period T_l. The initial phase was thus $\varphi_1 = \Delta t_1 / T_l$. To study the effect of phase for a single wing opening attempt (Section 2.5.5), we varied φ from 0% to 100% with an increment of 5% for each combination of θ_w and θ_l tested, without adding randomness. To test the predictive power of phase-based prediction method (Section 2.6.6), we varied φ from 0% to 100% with an increment 5% for each combination of wing period (2 s, 2.5 s, 3 s) and leg oscillation period (0.6 s, 0.8 s, 1 s, 1.2 s, 1.4 s) tested. We note that the animal's phase also varied from 0% to 100% (Appendix).

2.5.7 Potential energy barrier calculation

Self-righting requires overcoming a potential energy barrier (Domokos and Várkonyi, 2008). As a proxy to quantify the difficulty of self-righting over the range of θ_w and θ_l tested, we calculated how the minimal potential energy barrier to self-right changed with θ_w and θ_l. When the wings were fully open, the center of mass (CoM) was at a local minimum on the potential energy landscape, which corresponded with the metastable state with triangular base of support (yellow arrows and triangle). If the robot pivots over an axis formed by the edge of head and a wing to self-right (**Figure 10**), it overcomes a minimal potential energy barrier $\Delta E = mg\Delta h$. The simulation (and physical) robot did not always do so when self-righting, as its head or wing edge may lift off briefly during pivoting during dynamic rotation, and the actual barrier overcome may be slightly higher. However, the minimal barrier still provided a measure of how challenging it was to self-right.

To calculate the minimal barrier as a function of θ_w and θ_l, we first calculated the gravitational potential energy landscape of the robot over body pitch and roll space (Othayoth et al., 2017), for the range of θ_w and θ_l tested above. We imported the robot

CAD model in MATLAB and varied body pitch and roll from −180° to 180° for each combination of θ_w and θ_l to calculate its gravitational potential energy (we did not vary body yaw because it did not affect gravitational potential energy). Then, for each combination of θ_w and θ_l, we searched for the minimal potential energy barrier using a Breadth-first search method. Note that the potential energy landscape here is different and an advancement over the simplistic landscape in previous studies (Li et al., 2017; Li et al., 2019a), which only considered the body.

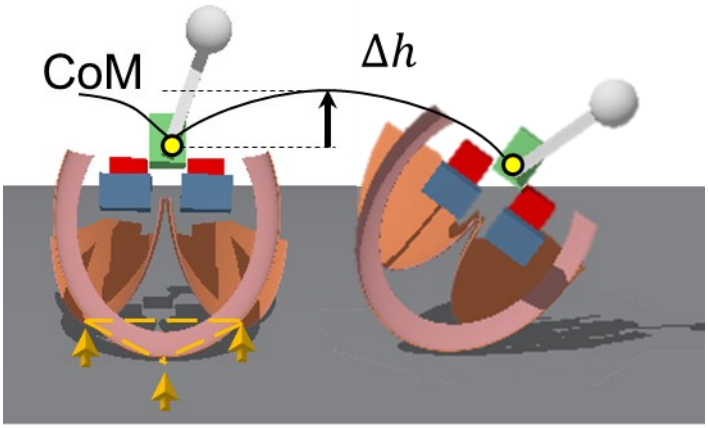

Figure 10. Snapshots of simulation robot during self-righting. Left: robot in metastable state, with two wings fully open and forming a triangular base of support (yellow arrows and triangle) with head on the ground. Right: robot pivoting over edge of head and right wing, overcoming the minimal potential energy barrier. Yellow dot is center of mass (CoM). Black curve is CoM trajectory. Δh is the height lifted (exaggerated) and defines gravitational potential energy barrier $E_{\text{barrier}} = mg\Delta h$, where m is robot mass and g is gravitational acceleration.

2.6 Results

2.6.1 Comparison between simulation and physical robot experiments

Qualitatively, the simulation robot displayed similar self-righting motion as the physical robot (**Figure 11**(a, b); Movie 2). In addition, the dependence of self-righting time on θ_w and θ_l was qualitatively similar between the two—it took both a shorter time to self-right as θ_w and/or θ_l increased (**Figure 11**(c)). This qualitative similarity meant that the simulation had the fundamental physics correct.

However, for a given θ_w and θ_l, it was easier for the physical robot to self-right than the simulation robot. This quantitative discrepancy was not surprising and likely due to several differences between the simulation and physical robots. First, the physical robot's thin wings and head likely deformed and decreased its potential energy barrier to self-right, compared to the simulation robot's rigid ones. In addition, the physical robot's left and right motors had small differences in actuation profiles (due to manufacturing variation). This lateral asymmetry may make it easier to self-right (Li et al., 2017). Furthermore, the Hertzian contact model used in simulation was developed for simple, ideal object shapes such as sphere and half-space (Popov, 2010). Contact mechanics modeling for objects with complex geometry is still an open area of research (Popov, 2010). Due to all these model approximations, quantitative match between the simulation and physical robots was difficult to achieve even after large scale parameter variation in simulation.

Our purpose is to study general principles of wing-leg coordination in leg-assisted, winged self-righting. Chrono Engine, as a matured physical engine, has been validated by some studies (Rieser et al., 2019; Tasora et al., 2016). Although there were quantitative discrepancies, our simulation still provided a useful tool to study the principles of how appendage coordination affected self-righting.

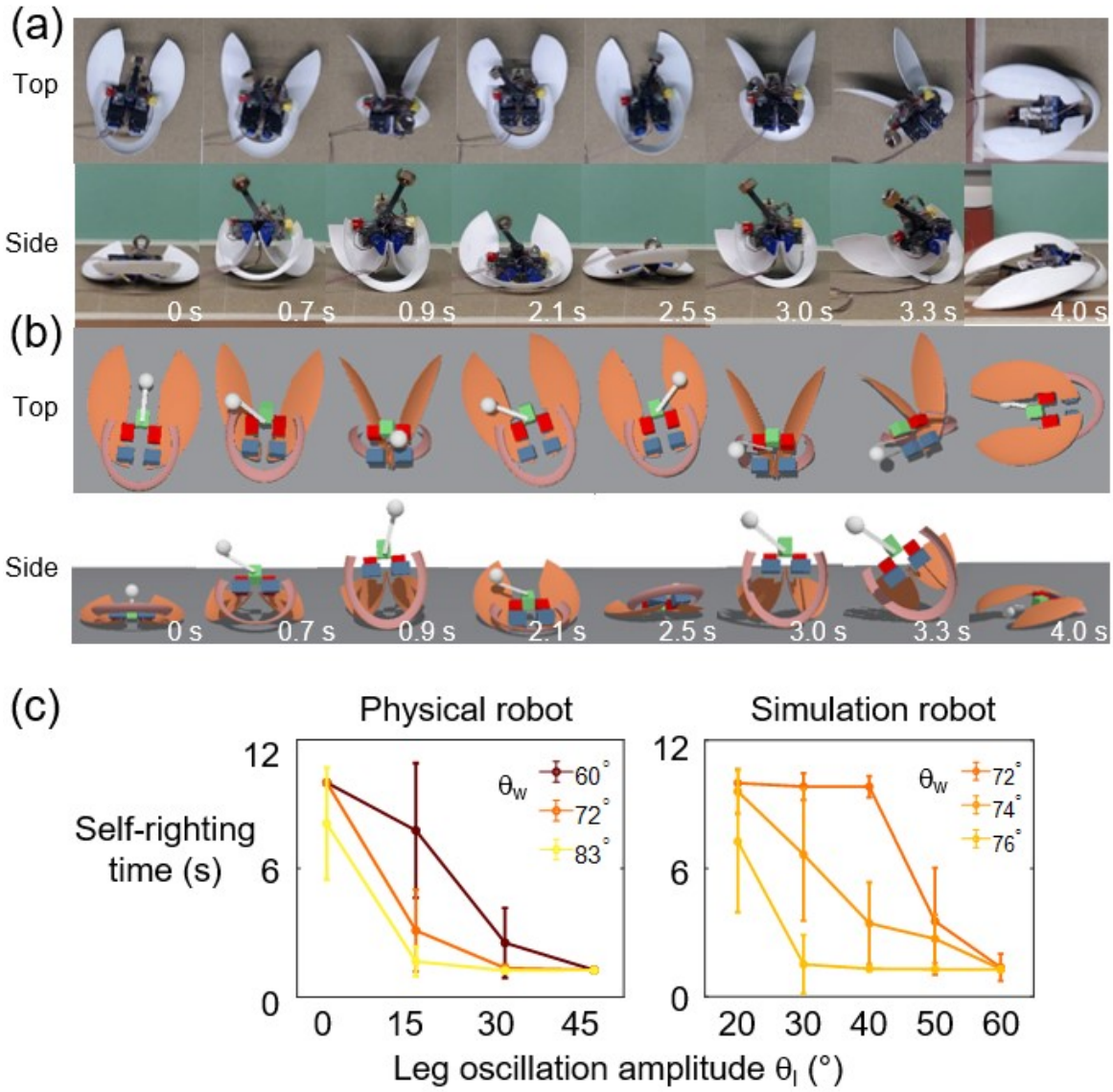

Figure 11. Validation of simulation robot against a physical robot. (a, b) Representative snapshots of physical (a) and simulation (b) robot experiments. (c) Self-righting time as a function of wing opening and leg oscillation amplitudes θ_w and θ_l, comparing between physical and simulation robots. Error bar are ± s.d. *n* = 5 trials at each combination of θ_w and θ_l for each robot.

2.6.2 Multiple attempts to self-right from metastable state

Similar to the animal (Li et al., 2019a) and physical robot (Othayoth et al., 2017), the simulation robot's self-righting often required multiple wing opening attempts (**Figure**

11(b); Movie 2). If the simulation robot could not self-right upon the first attempt, it kept opening and closing its wings to make more attempts, until it either succeeded or failed to self-right within 10 s. This was because, like the animal and physical robot, the simulation robot was also often stuck in a metastable state with a triangular base of support, formed by the head and outer edges of two wings in contact with the ground (**Figure 10**(a), yellow arrows and triangle). With sufficient perturbation from the leg, the simulation robot could escape from the metastable state, often after multiple attempts. These observations verified that our simulation robot displayed the strenuous leg-assisted, winged self-righting behavior that we are interested in.

2.6.3 Potential energy barrier

As wing opening amplitude θ_w increased, minimal gravitational potential energy barrier decreased (**Figure 12**), because center of mass (CoM) height at the metastable state increased. As leg oscillation amplitude θ_l increased, minimal gravitational potential energy barrier also decreased (**Figure 12**), because the CoM moved closer to the boundary of the triangular base of support (yellow triangle in **Figure 10**(a)) when the leg rotated to one side. Thus, we should expect it to become easier for the robot to self-right as wing opening and leg oscillation amplitude increased, with everything else being equal.

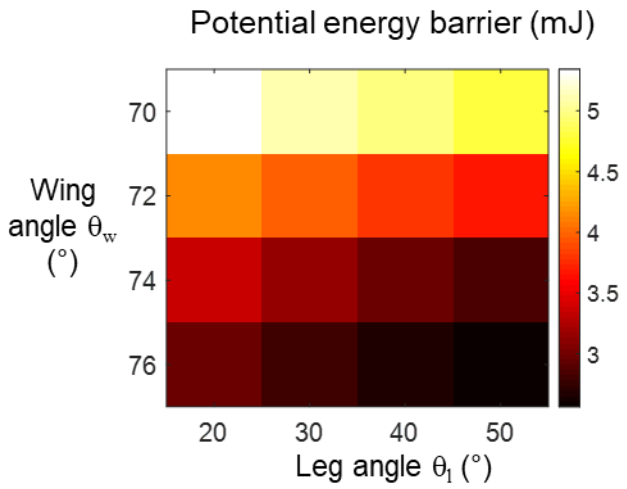

Figure 12. Minimal gravitational potential energy barrier as a function of wing and leg angles, which is the minimal energy barrier to escape the local potential energy minimum (Section 2.5.7).

2.6.4 Randomness in coordination increases self-righting probability

Without randomness in wing-leg coordination, self-righting outcome of the robot was deterministic. The robot either always succeeded or always failed to self-right for a given set of parameters (**Figure 13**, $C_v = 0\%$). With randomness, self-righting outcome became stochastic (**Figure 13**, $C_v > 0\%$). At each C_v, self-righting probability increased with wing opening and leg oscillation amplitudes (**Figure 13**), as expected from the decreasing potential energy barrier (**Figure 12**). Besides reducing the barrier, another reason that increasing leg oscillation amplitudes facilitated self-righting was that it increased leg rotation angular velocity and thus the kinetic energy that the leg injected.

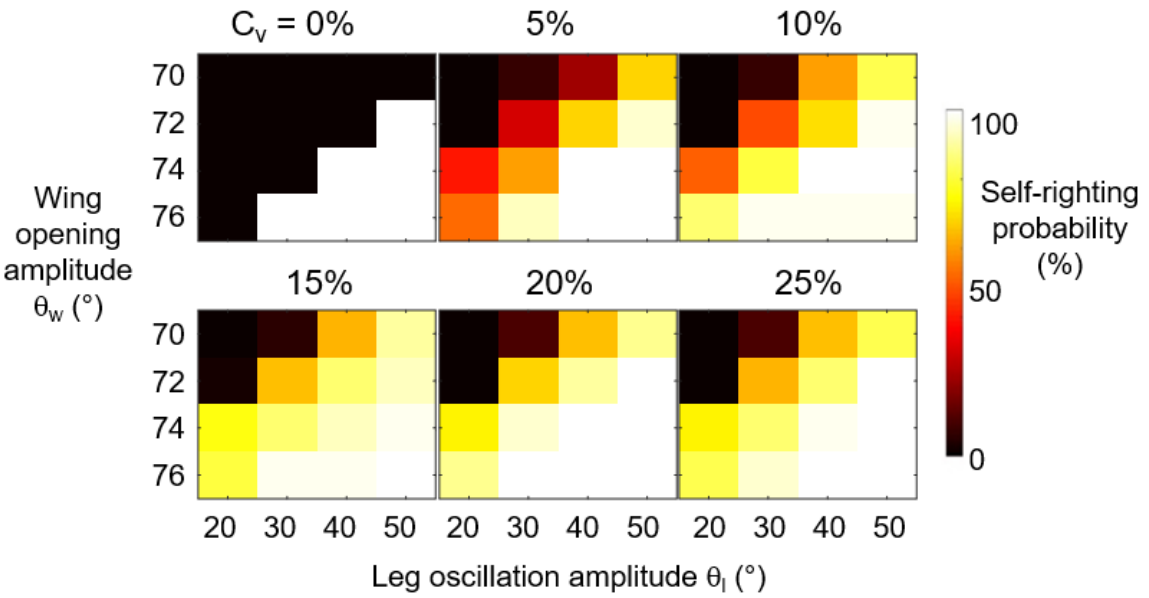

Figure 13. Effect of randomness in phase on self-righting probability within 10 s for each trial. Self-righting probability as a function of wing opening and leg oscillation amplitudes from simulation experiments, comparing across different levels of randomness C_v in wing-leg coordination. Data shown are for initial phase φ_1 = 70%. *n* = 40 trials at each combination of θ_w and θ_l.

When θ_w and θ_l were too small or too large, self-righting probability was nearly always zero or one, not strongly affected by randomness (**Figure 13**). However, at intermediate θ_w and θ_l near the boundary between success and failure without randomness (C_v = 0%), increasing level of randomness in wing-leg coordination significantly increased the robot's self-righting probability (**Figure 13**, C_v = 0-25%). For θ_w and θ_l slightly above the boundary, probability decreased slightly, but this was outweighed by the substantial increase in probability for θ_w and θ_l slightly below the boundary.

These results suggested that, when a cockroach is too tired (weak wing pushing and/or leg flailing), randomness does not help; when it is very energetic (strong wing pushing and/or leg flailing), randomness does not matter. However, when an animal is

nearly or barely able to self-right (intermediate wing pushing and leg flailing), which is frequent in strenuous self-righting, randomness in coordination significantly increases its chance of success. In addition, when randomness was sufficiently large, further increasing randomness did not significantly increase self-righting probability (**Figure 13**, $C_v \geq 15\%$).

We note that the initial phase φ_1 shown in this example happened to be a bad phase ($\varphi_1 = 70\%$, **Figure 13**; see definition in Section 2.6.5). However, if φ_1 happens to be a good phase, adding randomness may lead to requiring more attempts to self-right and thus decrease self-righting probability within a finite time.

2.6.5 Randomness in coordination changes phase between wing and leg oscillations

The phase between wing and leg oscillations had a strong impact on self-righting outcome at intermediate wing opening and leg oscillation amplitudes. This could be clearly seen from our results of self-righting outcome after a single attempt without randomness in coordination (**Figure 14**, hereafter referred to as the single-attempt phase map). When θ_w and θ_l were sufficiently large (e.g., $\theta_w = 76°$, $\theta_l = 50°$), the simulation robot self-righted at nearly all φ. When θ_w and θ_l were sufficiently small (e.g., $\theta_w = 72°$, $\theta_l = 20°$), the robot never self-righted at any φ. When θ_w and θ_l were intermediate (e.g., $\theta_w = 76°$, $\theta_l = 20°$), phase became important. Empirically, some “good” phases led to success (e.g., phases around $\varphi = 0\%$, 50%, and 100%), whereas other “bad” phases led to failure (e.g., phases around $\varphi = 25\%$ and 80%).

The change of self-righting outcome from success to failure at higher wing opening or leg oscillation amplitudes (e.g., lower probability at $\theta_l = 50°$ than at $\theta_l = 40°$ for $\theta_w = 70°$, $\varphi = 40\%$) was likely because, besides changing the potential energy barrier, changes in

wing opening and leg oscillation amplitudes also affected the energy injected and dissipated.

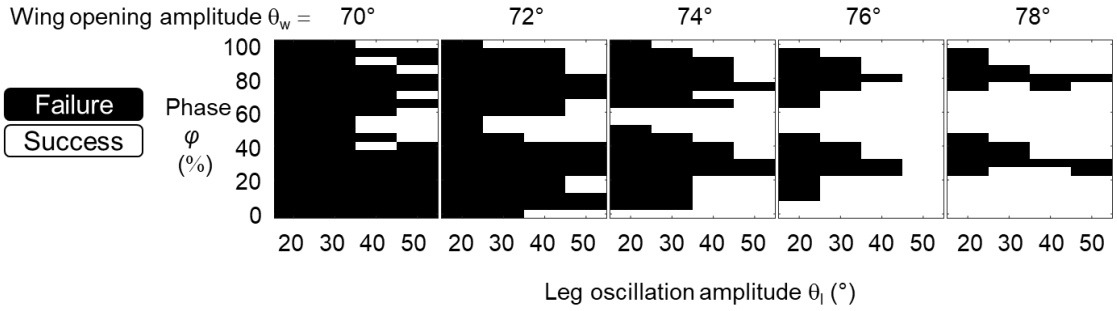

Figure 14. Dependence of self-righting outcome of a single attempt on phase (single-attempt phase map), without randomness in motion. Self-righting outcome as a function of φ and θ_l, comparing across θ_w.

2.6.6 Single attempt phase map predicts consecutive attempts outcome

After each failed attempt, the simulation robot oscillated little on the ground, because most of its kinetic energy was quickly dissipated (this was similar to the physical robot, see Section 2.6.1). Thus, consecutive attempts should be nearly independent of each other. Thus, we expected that the dependence of self-righting outcome on phase (phase map) was the same for every attempt. Then, we could use the phase map of a single attempt (**Figure 14**) to predict the self-righting outcome after multiple consecutive attempts, by evaluating how phase evolved over attempts. If there is a strong history dependence between consecutive attempts, we cannot use the single-attempt phase map to make prediction, but we expect that randomness in coordination would still help because it extends the coordination space.

To test how well this worked, we predicted the number of attempts to achieve successful self-righting for various initial φ_1 and wing period T_w without randomness

(**Figure 15**(a), right). Given initial φ_1, wing period T_w, and leg period T_l, we calculated how φ evolved for subsequent attempts (Section 2.6.7). We predicted that the attempt whose phase first reached the good phases in the single attempt phase map (Section 2.6.5) would be successful. Hereafter, we refer to this as the phase-based prediction method. The prediction of this method (**Figure 15**(a), right) matched well with simulation results (**Figure 15**(a), left) over the T_w and φ_1 space. For a broader range of T_w and T_l (**Figure 15**(b)), the phase-based prediction method achieved a high accuracy of 91 ± 6% (mean ± s.d.) in predicting the self-righting outcome observed in simulation experiments. We also used the phase-based method to predict self-righting probability with different levels of randomness C_v (**Figure 13**(c)), which well matched the results from simulation experiments (**Figure 15**(c)).

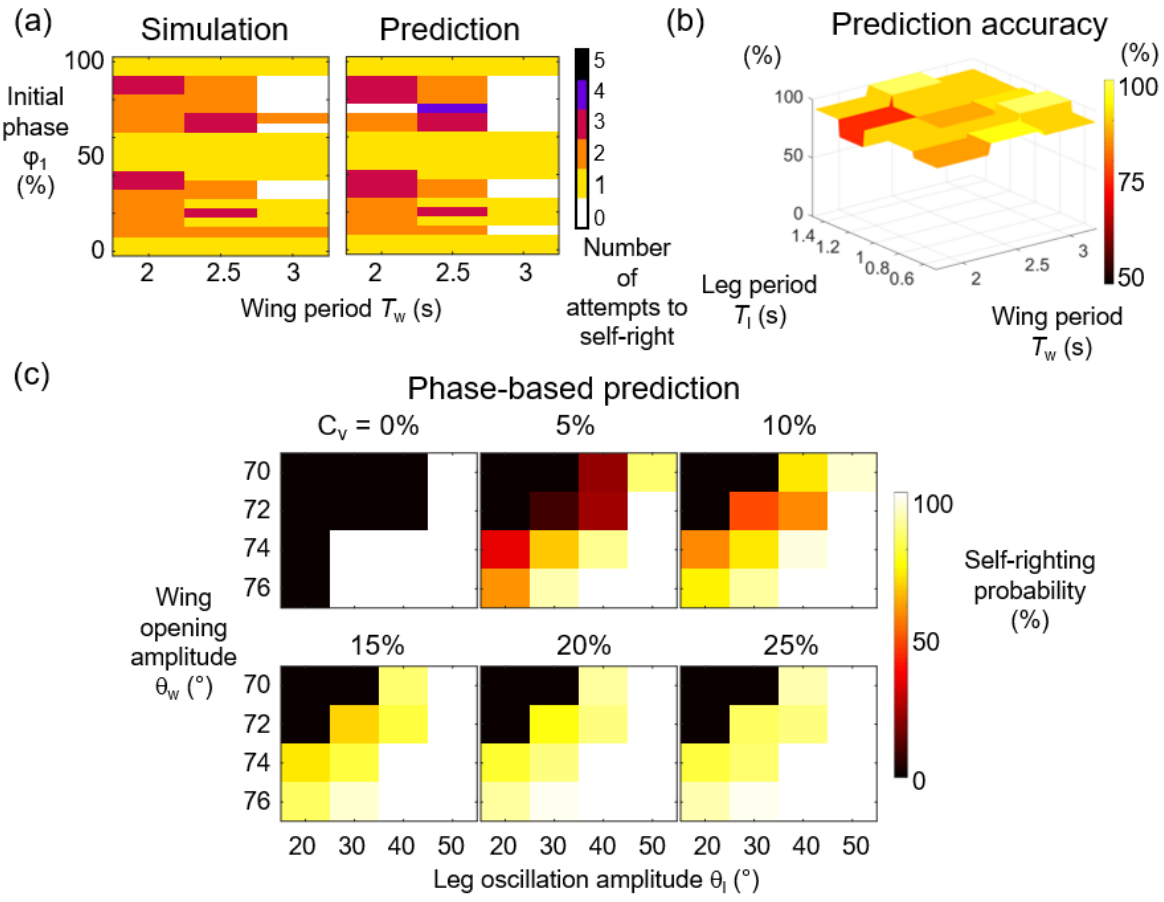

Figure 15. Using phase map from a single attempt to predict self-righting outcome after multiple attempts. (a) Prediction without randomness: Number of attempts required to self-right as a function of φ_1 and T_w, comparing between phase map prediction and simulation experiments. Failure to self-right is shown as number of attempts = 0. Data shown for T_l = 0.6 s, θ_w = 75°, θ_l = 30°. (b) Prediction without randomness: Prediction accuracy as a function of T_l and T_w. Prediction accuracy is percentage of phases at which phase-based prediction matches simulation experiments. Data shown for θ_w = 75°, θ_l = 30°. (c) Prediction with randomness: Self-righting probability as a function of θ_w and θ_l predicted by phased-based method, comparing across randomness C_v of coordination. n = 40 trials at each combination of θ_w and θ_l.

2.6.7 Randomness allows stochastic visits of good phases

Because the phase of each attempt was a good predictor of its outcome, we examined how phase evolved over consecutive attempts to understand how randomness affected self-righting performance. Without randomness, wing and leg actuation were periodic. This resulted in a limited number of phases that could be visited during consecutive attempts. If the phases that could be visited happened to be bad for the wing and leg oscillation periods given, self-righting was never successful. For example, for wing period T_w = 2 s and leg period T_l = 0.8 s, the least common multiple of both periods was LCM(2, 0.8) = 4 s. Thus, the robot could only visit n = LCM(2, 0.8)/2 = 2 different phases (e.g., **Figure 16**(a, c) with an initial phase of φ = 30%, followed by φ = 80%, and so on and so forth). Both these two phases happened to be bad, and the robot was trapped in bad phases forever (Movie 3).

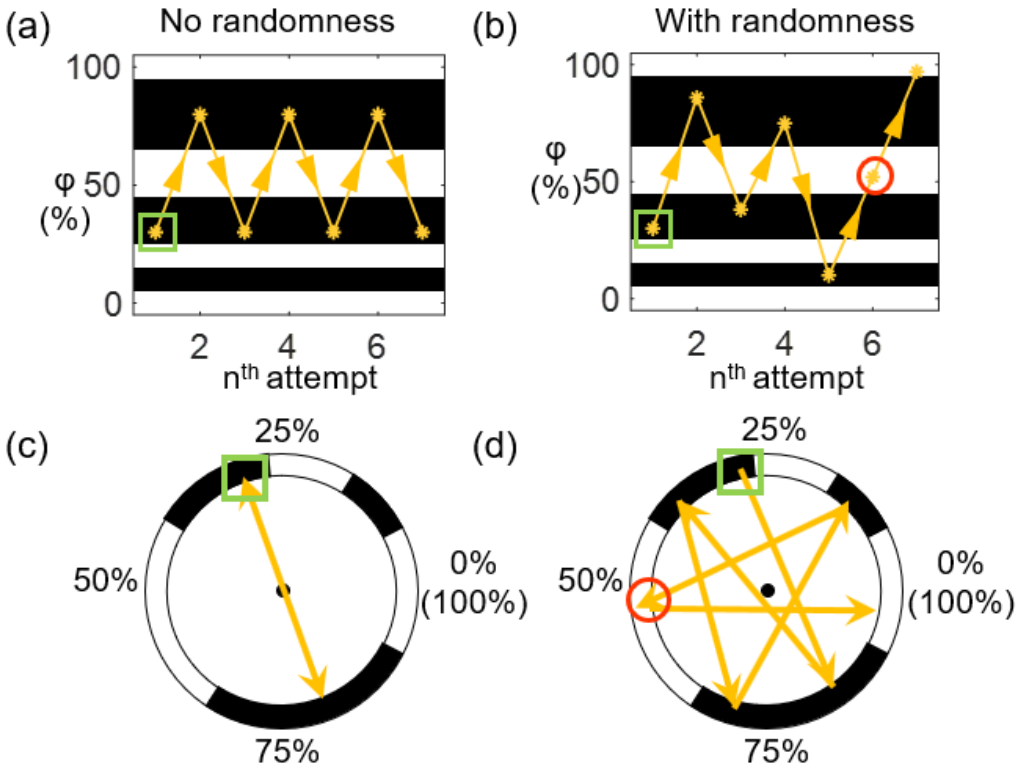

Figure 16. Phase evolution without and with randomness. Phase evolution over consecutive attempts (yellow points connected by arrows) on phase map (white: good phases, black: bad phases), without randomness (a, c) and with randomness (b, d). Phase map is from a single attempt in simulation experiments, assuming that it does not change over attempts. Green box shows initial phase at the first attempt. Red circle shows the first good phase reached with randomness. Data shown for $\theta_w = 75°$, $\theta_l = 30°$, $T_w = 2$ s, $T_l = 0.8$ s.

With randomness added to the motion, the phase evolution was no longer periodic (**Figure 16**(b, d)). Instead, the system could visit an infinite number of phases (any value from 0% to 100%) and was thus impossible to be trapped in bad phases, as long as there were good phases in the phase map (Movie 3). For the example case, as soon as it visited a good phase (the 6th attempt, **Figure 16**(b, d)), the robot self-righted. This is true for all trials because the Gaussian noise that we added has a non-zero probability to reach any value.

2.7 Discussions

In summary, we studied the impact of randomness in coordination between appendages during strenuous, leg-assisted, winged self-righting. We developed a simulation robot following the design and control of a recent physical robot to generate the strenuous self-righting behavior, and we used it to conduct systematic simulation experiments and analyses. We discovered that randomness in wing-leg coordination facilitated self-righting, especially at intermediate wing opening and leg oscillation amplitudes, when the system's kinetic energy was about to overcome the potential energy barrier. Randomness allowed the system to explore various phases more thoroughly between wing and leg oscillations, thereby increasing the chance of finding a good coordination between them.

Although we did not systematically vary wing opening and leg oscillation periods, our phase-based prediction test results for different periods (**Figure 15**a, b) indicated that randomness should facilitate self-righting by finding a good coordination even for different periods. Admittedly, the number of different phases accessible without randomness, $n = \mathrm{LCM}(T_w, T_l)/T_w$, can be made larger by choosing T_w and T_l, which increases the chance of finding a good coordination. However, without randomness, the system still searches for a good phase over the phase space with a constant increment every attempt, which is a grid search over the phase space that covers only a finite number of phases. By contrast, adding randomness to the system results in a random search that is more thorough (can cover any phase) and efficient than a grid search (Bergstra and Bengio, 2012; Lerman, 1980).

Our work focused on the effect of randomness in its simplest form, in the phase between a pair of oscillating wings and a single leg, and only gave a glimpse into a very

complex noisy system. Additional randomness may exist in the amplitudes, directions, and speed of the motions of multiple wings and legs, in the motions of other body parts such as the abdomen, as well as in the mechanical system itself (e.g., morphology, physical property, the environment), which may also be beneficial (see discussion in Section 2.7.2).

2.7.1 Implications for biological locomotion

Our results suggested that the large randomness in coordination during self-righting (as opposed to more periodic motion during walking and running) in the discoid cockroach and other species may be an adaptation to strenuous maneuvers. We speculate that animals may respond by moving their body and appendages more randomly when they encounter strenuous, emergency situations, such as being unable to self-right after multiple attempts, or becoming trapped by obstacles when moving in complex terrain (Gart and Li, 2018; Gart et al., 2018; Li et al., 2015; Othayoth et al., 2020).

Our study revealed the usefulness of randomness in biological and artificial system at the intermediate scale (body and appendage motion within a movement cycle), adding to previous knowledge at larger scales (e.g., trajectory over many body lengths and movement cycles) (Bénichou et al., 2005; Hoffmann, 1983; Reynolds and Rhodes, 2009) and smaller scales (e.g., sensory systems) (Gammaitoni and Bulsara, 2002; McDonnell and Ward, 2011; Wiesenfeld and Moss, 1995).

Our work complemented previous work on mitigating the negative impact of randomness to stabilize locomotion around limit cycles (Byl and Tedrake, 2009). In dynamic walking, randomness in terrain surface slope breaks the dynamic stability, which must be mitigated to maintain metastable locomotion (Byl and Tedrake, 2009). However, as we demonstrated, randomness in motion can also help escape being trapped in an undesired metastable state. This is especially useful if the locomotor task is strenuous.

This insight may have broader implications. For example, when moving through complex terrain with large obstacles, animals and robots must often dynamically transition across distinct locomotor modes (Li et al., 2015; Othayoth et al., 2020). Our group's recent work demonstrated that, in different modes, their states are strongly attracted to different basins of an underlying potential energy landscape (Gart and Li, 2018; Han et al., 2017; Othayoth et al., 2020). Our study suggested that body and appendage coordination is crucial for quickly escaping from these attractive landscape basins and having large randomness in coordination is beneficial.

2.7.2 Implications for robotics

Our simulation robot differed from the physical robot in that it did not have noise in the mechanical system which is inevitable in the physical robot. Without random time delay in actuation, the result of simulation experiments is deterministic, whereas the result of the physical robot experiments is stochastic. Despite this difference, we expect that our conclusion also applies to physical robots, because randomness should help explore the coordination space and find a good coordination regardless. In fact, we expect having randomness in coordination to be even more useful for real, stochastic physical robots because, unlike the deterministic simulation for which good phases can be identified in advance, good coordination is unknown in a stochastic system and must be searched every time.

We speculate that randomness in coordination could also improve the performance of robots in other strenuous locomotor tasks. When robots are trapped in undesirable metastable states, such as in complex terrain (Gart and Li, 2018; Gart et al., 2018; Li et al., 2015; Othayoth et al., 2020), their normal gait (walking, running, etc.) may

no longer work. Having or eliciting randomness in motions between body parts may help find a good coordination to escape from such unexpected emergencies.

Besides informing robot control, our discovery of the usefulness of randomness may also be useful for the mechanical design of self-righting robots. For example, one can use flexible and/or under-actuated appendages (e.g., using soft material and springs, or a hollow appendage with a heavy ball inside) to add stochasticity to the passive mechanics and dynamics.

2.7.3 Future work

Our study only discovered the usefulness of randomness but did not uncover the physical mechanism. Because successful dynamic self-righting requires sufficient mechanical energy to overcome potential energy barriers, wing and leg coordination influences self-righting probability presumably by changing the mechanical energy injected into system during each attempt. We are developing a simple template (analogous to (Libby et al., 2012; Patel and Braae, 2014; Saranli et al., 2004)) to model the hybrid dynamics of leg-assisted, winged self-righting to understand the physical mechanism (Xuan and Li, 2020b). In addition, it would be interesting to test a suggestion from our study—that energetic animals should have less randomness in motion whereas fatigues animals should have more. Finally, it would be intriguing (but perhaps difficult (Heams, 2014)) to tease apart how much the randomness in animal self-righting (and other forms of strenuous locomotion) is uncontrolled and unintentional, and how much may be deliberate, controlled randomness as a form of behavioral adaptation.

Chapter 3

Coordinated appendages help accumulate more energy to self-right on the ground

This chapter was previously published in *Robotics and Automation Letters* as an article entitled *Coordinated appendages help accumulate more energy to self-right on the ground* authored by Qihan Xuan and Chen Li (Xuan and Li, 2020b). We re-used the article in this chapter with the permission from the publisher and all the authors.

3.1 Author contributions

Qihan Xuan designed study, built physics model and simulation, analyzed data, and wrote the paper; Chen Li designed and oversaw study and revised the paper.

3.2 Acknowledgments

We thank Ratan Othayoth, Tom Libby, Shai Revzen, Simon Sponberg, Yifeng Zhang, and Yaqing Wang for discussion and three anonymous reviewers for suggestions. This work was supported by an Army Research Office Young Investigator award, a Burroughs Wellcome Career Award at the Scientific Interface, and The Johns Hopkins University Whiting School of Engineering start-up funds to C.L.

3.3 Summary

Animals and robots must right themselves after flipping over on the ground. The discoid cockroach pushes its wings against the ground in an attempt to dynamically self-right by a somersault. However, because this maneuver is strenuous, the animal often fails to overcome the potential energy barrier and makes continual attempts. In this process, the animal flails its legs, whose lateral perturbation eventually leads it to roll to the side to self-right. Our previous work developed a cockroach-inspired robot capable of leg-assisted, winged self-righting, and a robot simulation study revealed that the outcome of this strategy depends sensitively on wing-leg coordination (measured by the phase between their motions). Here, we further elucidate why this is the case by developing a template to model the complex hybrid dynamics resulting from discontinuous contact and actuation. We used the template to calculate the potential energy barrier that the body must overcome to self-right, mechanical energy contribution by wing pushing and leg flailing, and mechanical energy dissipation due to wing-ground collision. The template revealed that wing-leg coordination (phase) strongly affects self-righting outcome by changing mechanical energy budget. Well-coordinated appendage motions (good phase) accumulate more mechanical energy than poorly-coordinated motions (bad phase), thereby better overcoming the potential energy barrier to self-right more successfully. Finally, we demonstrated practical use of the template for predicting a new control strategy to further increase self-righting performance and informing robot design.

3.4 Introduction

Animals and mobile robots must right themselves when flipped over on the ground (Domokos and Várkonyi, 2008; Frantsevich, 2004; Guizzo and Ackerman, 2015a). How likely and how quickly they can self-right is important for survival or continuing operation.

Animals and robots self-right using many strategies. Most robots use a single morphological feature or one type of appendages to self-right (for a review, see (Li et al., 2017)), such as adopting an unstable body shape when upside down (Kovač et al., 2010), adding an extruding appendage (Casarez and Fearing, 2017), jumping with elastic energy storage and release (Fiorini and Burdick, 2003), and co-opting rounded wings intended for terradynamic streamlining (Li et al., 2015; Li et al., 2017). Few robots have used multiple appendages together to self-right (Saranli et al., 2004). By contrast, some animals have evolved more complex strategies that combine different body parts to self-right dynamically (for a review, see (Li et al., 2019a)). This is especially the case when self-righting is strenuous. For example, on slippery surfaces, insects use wings and legs together (Li et al., 2019a); turtles with a rigid, flattened shell uses legs and neck together (Domokos and Várkonyi, 2008).

Coordination between appendages is important in locomotion such as walking (Collins et al., 2009), running (Seay et al., 2006), swimming (Kwak and Bae, 2017), and self-righting (Frantsevich, 2004), for energetic efficiency, recovery from perturbation, maintaining steady-state movement, and faster escaping. Coordinated appendage motions from a central pattern generator also helps simplify the generation of compound movement (Tresch et al., 2002).

Our study focuses on appendage coordination in leg-assisted, winged ground self-righting (Li et al., 2019a; Othayoth et al., 2017; Xuan and Li, 2019), a strategy observed in the discoid cockroach (Sec. 3.5). In a recent study, we discovered that wing-leg coordination strongly affects the outcome of this strategy (Xuan and Li, 2019) (Sec. 3.5). Here, we take the next step in understanding the mechanism by developing a template of leg-assisted, winged self-righting (Sec. 3.6) to model its complex hybrid dynamics (Sec. 3.7). We used the template to analyze mechanical energy budget during self-righting (Sec. 3.8)—whether the total mechanical energy accumulated (injection by wings and legs minus dissipation) exceeds the potential energy barrier. We discovered that well-coordinated wing opening and leg flailing motions help accumulate more mechanical energy than poorly-coordinated ones, making it easier to overcome the potential energy barrier. In addition, we used the template to devise a new control strategy to coordinate wing and leg motions, which further improved self-righting performance (Sec. 3.9), and we used template analysis to inform robot design (Sec. 3.10). Finally, we summarize our contributions and discuss future directions (Sec. 3.11).

3.5 Model system & previous work

When flipped over on a level, flat surface, the discoid cockroach often opens its wings to push against the ground, in an attempt to self-right by a somersault (pitching over the head) (Li et al., 2019a). However, because the potential energy barrier in doing so is great (seven times the mechanical energy generated per stride during medium-speed running at 5 body length/s (Li et al., 2019a)), wings pushing rarely generates sufficient mechanical energy (Othayoth et al., 2017) to complete a somersault (Li et al., 2019a). While the wings are open and body is pitched up, the animal often flail its legs in the air laterally (**Figure 17**A), as well as twist and bend its raised abdomen (Li et al., 2019a).

These secondary motions perturb the body laterally and facilitate self-righting, by adding kinetic energy (Othayoth et al., 2017) and shifting the center of mass. As a result, the animal often eventually self-rights by body rolling after the initial pitching up (**Figure 17**B) (Li et al., 2019a). For this leg-assisted, winged self-righting strategy, flailing legs is an interval motion which does not change total angular momentum directly. Thus, the animal often makes multiple wing opening attempts (Li et al., 2019a) before it accumulates sufficient mechanical energy to overcome the barrier to self-right.

In recent studies, we developed a cockroach-inspired self-righting robot (Othayoth et al., 2017) and a multi-body dynamics simulation robot (Xuan and Li, 2019) (**Figure 17**C; Movie 4). We performed simulation experiments to empirically study how wing-leg coordination affects self-righting outcome (Xuan and Li, 2019). The robot has two wings that open symmetrically and a pendulum leg that flails laterally, as well as a curved head that protrudes forward. Its configuration can be defined by wing and leg angles (**Figure 17**D). The wings and leg are controlled by motors to oscillate with simple actuation profiles (**Figure 17**E). For every wing opening attempt (every cycle of wing oscillation), wing-leg coordination can be measured by the phase φ between wing and leg oscillations (defined in **Figure 17**E caption). We varied phase to test whether the robot self-righted. Unless leg oscillation amplitude was very small or very large, for given leg oscillation amplitude, self-righting was always more successful at some phases (e.g., φ = 0%, 50%, and 100%) than others (e.g., φ = 25% and 80%) (**Figure 17**F) (Xuan and Li, 2019). Note that in our previous work, random noise was added to the period of wing oscillation during each cycle to change the phase in every wing opening attempt (Xuan and Li, 2019). Here, we focused on understanding of the role of phase during a single attempt, and random noise was not added.

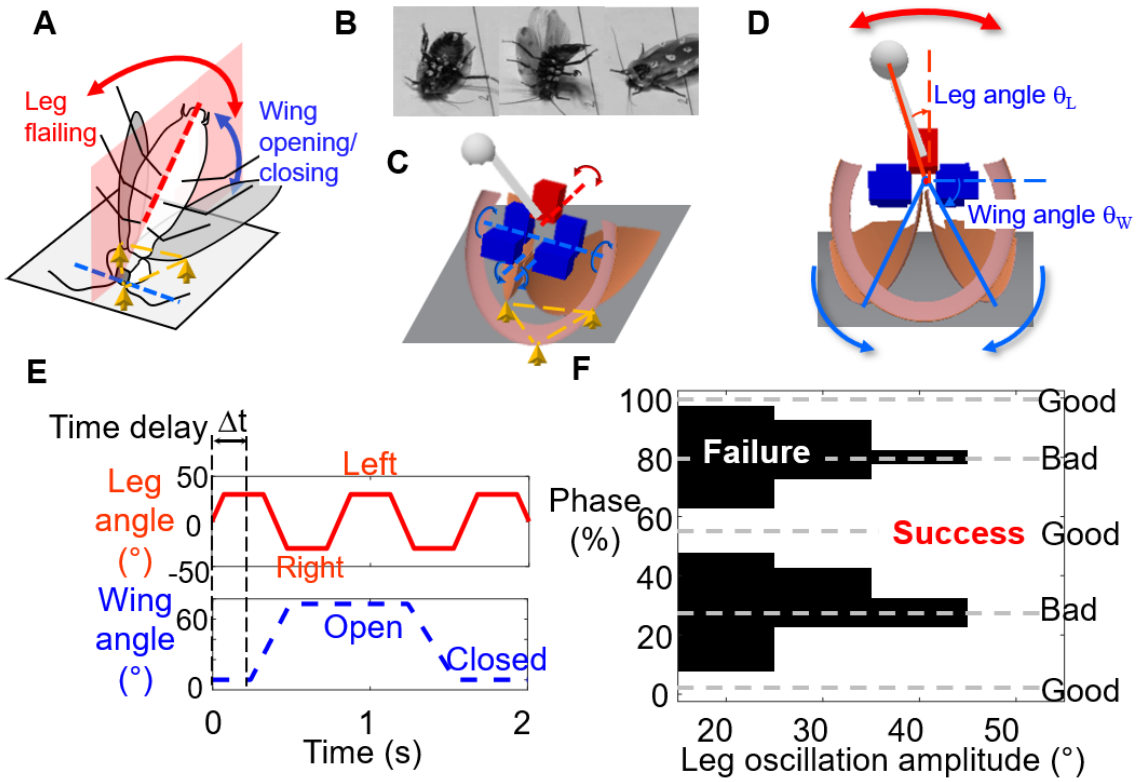

Figure 17. Leg-assisted, winged self-righting on the ground and previous observations. (A) Schematic of strategy in a discoid cockroach. Yellow arrows and triangle show metastable triangular base of support formed by head and two wings in contact with ground. (B) Snapshots of a cockroach self-righting. (C) Simulation robot with a head, two wings and a pendulum leg. (D) Definition of wing and leg angles. (E) Actuation profiles of wing and leg oscillations. Wing-leg coordination is measured by phase $\varphi = \Delta t/T_{leg}$, where Δt is time delay of start of wing opening from start of the first leg oscillation, and T_{leg} is leg oscillation period. Wing opening amplitude is the maximal wing opening angle. Leg oscillation amplitude is the maximal leg angle (absolute value) to either side from middle. Leg starts from the middle (leg angle = 0) at time $t = 0$. (F) Self-righting outcome (white: success, black: failure) as a function of phase and leg oscillation amplitude at a given wing opening amplitude (76°), from simulation experiments in previous study (Xuan and Li, 2019).

3.6 Template

Here, to understand the mechanism of how the phase between wing and leg actuation affects self-righting outcome, we developed a template of leg-assisted, winged self-righting (**Figure 18**; Movie 4).

A template is the simplest dynamical model with the least number of components and degrees of freedom to realize the most fundamental dynamics of a targeted locomotor behavior (Full and Koditschek, 1999). Templates have been developed for walking (Cavagna et al., 1977), upright (Blickhan and Full, 1993) and sprawled (Schmitt and Holmes, 2000) running, climbing (Goldman et al., 2006), tail-assisted aerial self-righting (Libby et al., 2016), multi-legged ground self-righting (Saranli et al., 2004), and dynamic large gap traversal (Gart et al., 2018). Although they lose details, templates are quantitatively predictive and useful for not only explaining biological phenomena but also predicting design, control, and planning for robots (Holmes et al., 2006).

Our template is novel in that it studies active coordination between different types of appendages. Although appendage coordination is clearly important in the locomotion where more than one appendage is involved, few of the models above systematically studied how appendage coordination affects movement. Arm-leg coordination was studied in walking models, but the arms are passive (not actuated) and active coordination was not studied (Collins et al., 2009). The multi-legged ground self-righting model optimally controls the torques of three well-coordinated pairs of legs to maximize thrust and impact kinetic energy recovery (Saranli et al., 2004); however, such coordination is between appendages of the same type.

For simplicity, our template only models planar dynamics in the transverse plane (**Figure 18**), considering that leg-assisted, winged self-righting eventually succeeds by body rolling (see Sec. 3.5). Our template has six simplifying approximations:

(1) The body is a point mass *M*, and the leg mass *m* is concentrated at its tip.

(2) The wings and leg linkage are massless links only for support and connection.

(3) Wing-ground contact is a point contact. It slides during wing opening but stays fixed when the body rotates around it.

(4) The wings and leg linkage are straight and rigid.

(5) Wing-ground collision is instantaneous and inelastic.

(6) Wing and leg motors start and stop instantaneously.

In our template each contacting wing tip can slide on the ground. From Approximations 5 and 6, wing-ground collision forces and motor torques are infinite (very large compared to robot weight) at the instances of collision and motor starting/stopping.

Although the three-link bipedal walking model (Grizzle et al., 2001) appears similar to our template, its targeted locomotor behavior is stable walking as opposed to escaping from a metastable state (Othayoth et al., 2017; Xuan and Li, 2019), its ground contact point is unable to slide, and it has different mass properties.

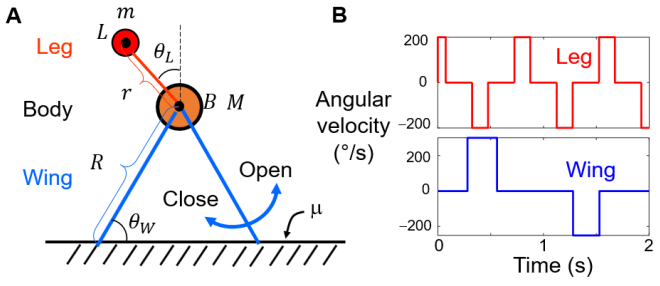

Figure 18. Template. (A) Schematic of template. Two point masses represent body (orange, B, mass M = 210 g) and leg pendulum mass (red, L, m = 50 g). Three massless links represent wings (blue segments, R = 12 cm) and leg linkage (red segment, r = 7 cm). θ_W and θ_L are wing and leg angles. Increasing and decreasing θ_W correspond with wing opening and closing, respectively. $\mu = 1.0$ is coefficient of friction between wing and ground measured from experiment using inclined plane method. (B) Actuation profiles of template. Angular velocities of wings (blue) and leg (red) as a function of time.

We designed the template to match the robot (Othayoth et al., 2017; Xuan and Li, 2019) in geometry and mass distribution (**Figure 18**A), and we used the measured coefficient of friction. We also used the same wing and leg actuation profiles as in the simulation robot (**Figure 17**E), as shown by their angular velocity profiles (**Figure 18**B) (Othayoth et al., 2017). A difference is that motor starting and stopping are instantaneous in the template (**Figure 18**B), whereas they take a short time (< 0.04 s) in the robot. We used constant wing opening (300°/s) and closing (250°/s) angular velocities and a constant leg rotation duration (0.15 s), the same as those of the simulation robot. To test the predictive power of the template over a broad range of parameter space, we varied the amplitudes of wing opening (66° to 80° with an increment of 2°) and leg oscillation (20° to 60° with an increment of 10°). Given the constant leg rotation duration, a larger leg oscillation amplitude corresponds with a larger angular velocity. Wing oscillation periods (2.0 s) and leg oscillation periods (0.8 s) are both constant.

3.7 Dynamics

The template is a hybrid dynamical system (Caines, 2002) because of discontinuity in wing and leg velocities (instantaneous actuation states) and hybrid contact between the wings and ground (instantaneous contact states):

(1) Actuation states. With the prescribed actuation profiles (**Figure 18**B), both the wing motor (which opens or closes both wings symmetrically) and leg motor can be in four states—starting, stopping, rotating at a constant angular velocity, and holding an angle. Both wing and leg motor states are prescribed functions of time.

(2) Contact states. Each wing tip can be in four contact states with the ground—no contact, collision, fixed contact, and sliding contact. Given contact states at each time step, we can use the current configuration, position, velocity, and motor states to determine contact states at the next time step.

The actuation and contact states that the system is in affects the forces and external constraints act on it, which often results in different equations of motion.

Some of the states above are continuous motions (e.g., motor rotating or holding an angle in actuation states; fixed or sliding contact and no contact in contact states). Others are instantaneous events (motor starting and stopping in actuation states, collision in contact states). The hybrid dynamics comprises dynamics of continuous motions (e.g., **Figure 19**Ai-iii and that of instantaneous events (e.g., **Figure 19**Bi-iii).

For continuous motions, we used forces to solve for dynamics. For instantaneous events, we used impulse to solve for the change of velocity via conservation of angular momentum (see Sec. 3.7, Aiii, Biii).

Below, we describe how we solve the dynamics for six representative cases (**Figure 19**), organized into continuous motions (**Figure 19**A) and instantaneous events (**Figure 19**B). These six cases encompass almost all possible cases of the system, except for when wing motor starts. We write equations in the general form by always including leg rotation angular velocity ω_L; when the leg is holding an angle, we set $\omega_L = 0°/s$. Initially

(t = 0 s), the system is static on the ground with the wings fully closed ($\theta_W = 0°$) and leg in the middle ($\theta_L = 0°$). As time elapses, it transitions between different states.

Although the model is 2-D, angular velocity vectors are orthogonal to the transverse plane (i.e., they are along *y* axis, with +*y* pointing into the paper). For simplicity, we write equations using 3-D vector format (e.g., $\overrightarrow{\omega_L} = (0, \omega_L, 0), \vec{g} = (0, 0, -\mathrm{g}), \overrightarrow{AB} = (x_B, y_B, z_B) - (x_A, y_A, z_A), \overrightarrow{v_B} = (v_{xB}, 0, v_{zB})$).

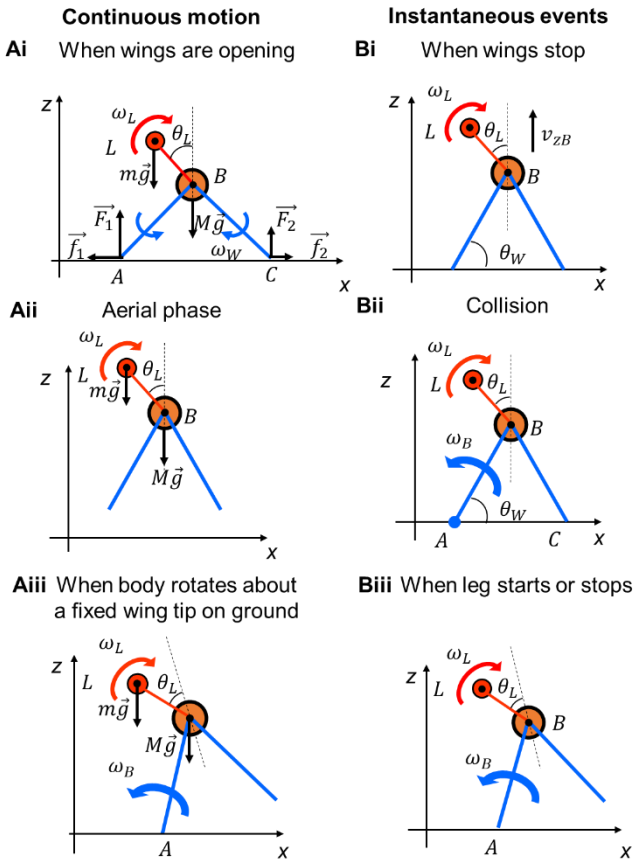

Figure 19. Hybrid dynamics. We show six representative cases with different actuation and contact states, with definitions of forces (F_1, F_2, f_1, f_2, *mg*, *Mg*), wing tips (point A, C), and angular velocity (ω_L, ω_B). (Ai-iii) Continuous motions. (Bi-iii) Instantaneous events.

A. Continuous motions

i. When wings are opening

When the wings are opening, both wings slide on the ground (**Figure 19**Ai). Both wing and leg angular velocities are constant during moving (wing opening or leg rotation) (**Figure 18**B):

$$\dot{\theta}_W(t) = \omega_W,\ \dot{\theta}_L(t) = \pm\omega_L \tag{3}$$

where +/– is clockwise/counterclockwise for leg rotation.

Given the angle actuation profiles (**Figure 18**B), we can calculate body and leg mass motion in the vertical *z* direction. Vertical position, velocity, and acceleration of the body are:

$$z_B(t) = Rsin\theta_W(t) \tag{4}$$

$$v_{zB}(t) = \omega_W\, Rcos\theta_W(t) \tag{5}$$

$$a_{zB} = \ddot{z_B}(t) = -R{\omega_W}^2 sin\theta_W(t) \tag{6}$$

Those of the leg mass are:

$$z_L(t) = z_B(t) + rcos\theta_L(t) \tag{7}$$

$$v_{zL}(t) = v_{zB}(t) - \omega_L\, rsin\theta_L(t) \tag{8}$$

$$a_{Lz} = \ddot{z_L}(t) = a_{zB} + {\omega_L}^2 rcos\theta_L(t) \tag{9}$$

From the center of mass theorem, vertical acceleration a_{zCoM} of the center of mass (CoM) is:

$$(M+m)a_{zCoM} = Ma_{zB} + ma_{zL} \tag{10}$$

However, motion in the horizontal *x* direction cannot be directly calculated from the actuation profiles, and we need to calculate horizontal forces. Below we use “1/2” to refer to the left/right wing. Because of lateral asymmetry in actuation and mass distribution from a single leg rotation, leg torque and gravitational force are asymmetric. Thus, the normal

forces F_1, F_2 and frictional forces f_1, f_2 at two wing tips are different. This gives the robot center of mass a non-zero lateral velocity.

From Newton's second law, CoM acceleration a_{xCoM} and a_{zCoM} can be solved from:

$$(M+m)a_{xCoM} = f_1 + f_2 \tag{11}$$

$$(M+m)a_{zCoM} = F_1 + F_2 - Mg - mg \tag{12}$$

During wing opening, either both wing tips in contact with the ground slide, or only one slides while the other is fixed. When both slide, frictional forces are:

$$f_1 = \pm\mu F_1 \tag{13}$$

$$f_2 = \pm\mu F_2 \tag{14}$$

where +/– is to the right/left, with frictional force opposite to wing tip horizontal velocity, and μ the coefficient of friction. When only one wing tip slides while the other is fixed, the frictional force on the fixed wing tip does not satisfy Eqns. 13, 14. But because it is fixed, we can calculate the body horizontal velocity directly from wing actuation profile:

$$v_{xB}(t) = \pm\omega_W R sin\theta_W(t) \tag{15}$$

where +/– is when the right/left wing tip is fixed.

From the center of mass theorem, horizontal acceleration a_{xCoM} of CoM is given by:

$$(M+m)a_{xCoM} = Ma_{xB} + ma_{xL} \tag{16}$$

Applying Newton's second law in the vertical direction:

$$F_1 + F_2 - (m+M)g = Ma_{zB} + ma_{zL} \tag{17}$$

and about the rotation axis (y):

$$\overrightarrow{AC} \times \overrightarrow{F_2} + \overrightarrow{AB} \times M(\vec{g} - \vec{a}_B) + \overrightarrow{AL} \times m(\vec{g} - \vec{a}_L) = 0 \tag{18}$$

With seven equations (Eqns. 11-14, 16-18), we can solve for the seven unknown variables (F_1, F_2, f_1, f_2, a_{xCoM}, a_{xB}, a_{xL}). Thus, we can obtain horizontal motion of the system.

ii. Aerial phase

During aerial phase, the only external force is gravitational force (**Figure 19**Aii, Mg and $m\vec{g}$). Thus, the CoM moves like a projectile. CoM velocity $\overrightarrow{v_{CoM}}(t)$ can be calculated as a function of time given initial CoM velocity (Sec. 3.7, Bi). Because the leg is rotating with a constant angular velocity $\overrightarrow{\omega_L}$, the velocities of the leg mass and body follow:

$$\overrightarrow{v_L} - \overrightarrow{v_B} = \overrightarrow{\omega_L} \times \overrightarrow{BL} \tag{19}$$

Further, from the center of mass theorem:

$$(M+m)\overrightarrow{v_{CoM}} = M\overrightarrow{v_B} + m\overrightarrow{v_L} \tag{20}$$

Thus, we can solve these two equations for $\overrightarrow{v_L}$ and $\overrightarrow{v_B}$ during the aerial phase to obtain the projectile dynamics. Because the internal rotational kinetic energy and mechanical energy of CoM are both conserved, the rotating leg motor does no work in the aerial phase.

iii. When body rotates about a fixed wing tip on ground

In this case, only gravitational force changes the angular momentum of the system about the contacting wing tip (**Figure 19**Aiii). Applying Newton's second law along the rotational direction (*y* axis), we can solve for body angular velocity $\overrightarrow{\omega_B}(t)$ relative to the contacting wing tip via:

$$(M+m)\vec{g} = \frac{d\vec{L}(t)}{dt} \tag{21}$$

where angular momentum about the contacting wing tip is:

$$\vec{L}(t) = M\overrightarrow{AB} \times \left(\overrightarrow{\omega_B}(t) \times \overrightarrow{AB}\right) + m\overrightarrow{AL} \times \left(\overrightarrow{\omega_B}(t) \times \overrightarrow{AL} + \overrightarrow{\omega_L} \times \overrightarrow{BL}\right) \tag{22}$$

B. Instantaneous events

i. When wings stop

When wing opening stops, there is no external impulse to change the velocities of body and leg mass (**Figure 19**Bi). Thus, because of inertia, both wings lift off the ground with a finite upward body velocity (**Figure 19**Bi, v_{zB}), which can be calculated by applying

Eqn. 5 at the instance of wing stopping. The body horizontal velocity remains unchanged at this instance.

ii. Collision

At collision, two external forces act on the system—gravitational force at the CoM and a collision force at the colliding wing tip (**Figure 19**Bii, contact point A). Because the event is instantaneous, the angular impulse generated by the gravitational force can be neglected. In addition, because center of rotation is at the contact point, collision force has no moment arm. Thus, the collision force generates no angular impulse. Therefore, the angular momentum of the system about the instantaneous center of rotation is conserved at collision. We can use this to solve for angular velocity $\overrightarrow{\omega_B}$ of the body:

$$M\overrightarrow{AB} \times \left(\overrightarrow{\omega_B} \times \overrightarrow{AB}\right) + m\overrightarrow{AL} \times \left(\overrightarrow{\omega_B} \times \overrightarrow{AL} + \overrightarrow{\omega_L} \times \overrightarrow{BL}\right) = \quad \vec{L} \tag{23}$$

where the left side is the angular momentum after collision and $\vec{L}$ is the angular momentum before collision, which is solved from the dynamics before collision.

iii. When leg starts or stops.

Like during collision (Sec. 3.7, Bii), when the leg starts or stops, two external forces act on the system—gravitational force at the center of mass and contact force at the contacting wing tip (**Figure 19**Biii, contact point A). The contact force is infinite because of infinite leg motor torque. Thus, we can also use Eqn. 23 to solve for the dynamics of leg starting and stopping. For leg stopping, we set $\overrightarrow{\omega_L} = (0, 0, 0)$.

We applied the Euler method to numerically integrate forward in time to calculate the dynamics of the system (both in translation and rotation, with time step Δt = 0.0001 s). To obtain velocities (both in translation and rotation), we can calculate directly from actuation

profiles (Sec. 3.7), integrate from the acceleration (Sec. 3.7, Ai-iii), or calculate from the conservation of angular momentum (Sec. 3.7, Bi-iii).

3.8 Mechanical energy budget

The robot and the discoid cockroach often struggled for multiple attempts before they could self-right (Li et al., 2019a; Othayoth et al., 2017; Xuan and Li, 2019). Although the motors/muscles do positive work when the robot or animal opens the wings and flails the leg(s) (**Figure 17**A, C), the mechanical energy injected may not be sufficient to overcome the potential energy barrier. For the robot, this is because mechanical energy is dissipated at collision and motor stopping. To understand how wing-leg coordination affects self-righting outcome, we used the template to calculate how mechanical energy is accumulated from energy injection minus energy dissipation, and we compared cumulative mechanical energy with the potential energy barrier to assess whether self-righting is successful or not.

A. Potential energy barrier

First, we calculated the potential energy barrier of the template. Consider two snapshots during self-righting (**Figure 20**A), with CoM at a local minimum (left) and a local maximum (right). A potential energy barrier is the increase in gravitational potential energy from the local minimum to maximum, $E_{\text{barrier}} = (M + m)g\Delta h$. Because of lateral asymmetry in mass distribution from a single leg rotation, rotating to the left and right sides have different potential energy barriers (**Figure 20**A). We defined the lower of the two as the potential energy barrier to self-right, as it is the minimal mechanical energy that that must be accumulated. We found that the potential energy barrier decreases with both wing and

leg angles (**Figure 20**B), consistent with the 3-D robot (Othayoth et al., 2017; Xuan and Li, 2019). For given mechanical energy, the smaller the barrier, the easier it is to self-right.

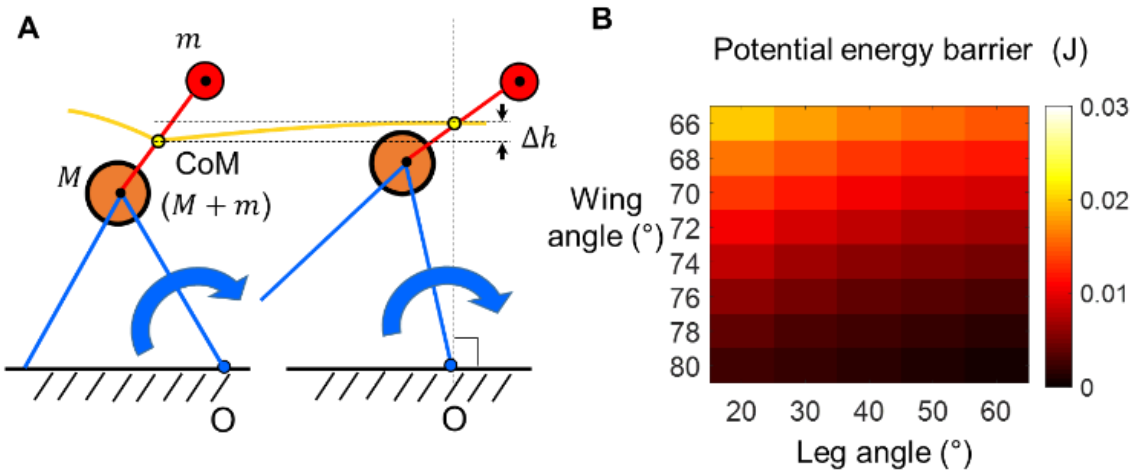

Figure 20. Potential energy barrier. (A) Two snapshots of template rotating about a fixed wing tip O. Yellow curve is CoM trajectory. Δh is CoM height increase between snapshots. (B) Potential energy barrier from template as a function of wing and leg angles.

B. Mechanical energy evolution

Next, we used the template to calculate mechanical energy evolution of the system over the potential energy landscape. We used body roll γ to define system orientation (**Figure 21**A) and calculated the potential energy landscape over body roll (**Figure 21**C-E, blue curve). The system's mechanical energy (**Figure 21**C-E, red dot) evolves (red trajectory) over the changing potential energy landscape (blue curve; see Movie 4). It is always on or above the potential energy landscape because kinetic energy cannot be negative.

Both wing opening and leg stroke do work to change mechanical energy. In simulation experiments, self-righting always occurs after wing opening stops (Xuan and Li, 2019), so we consider subsequent mechanical energy accumulation (**Figure 21**C-E).

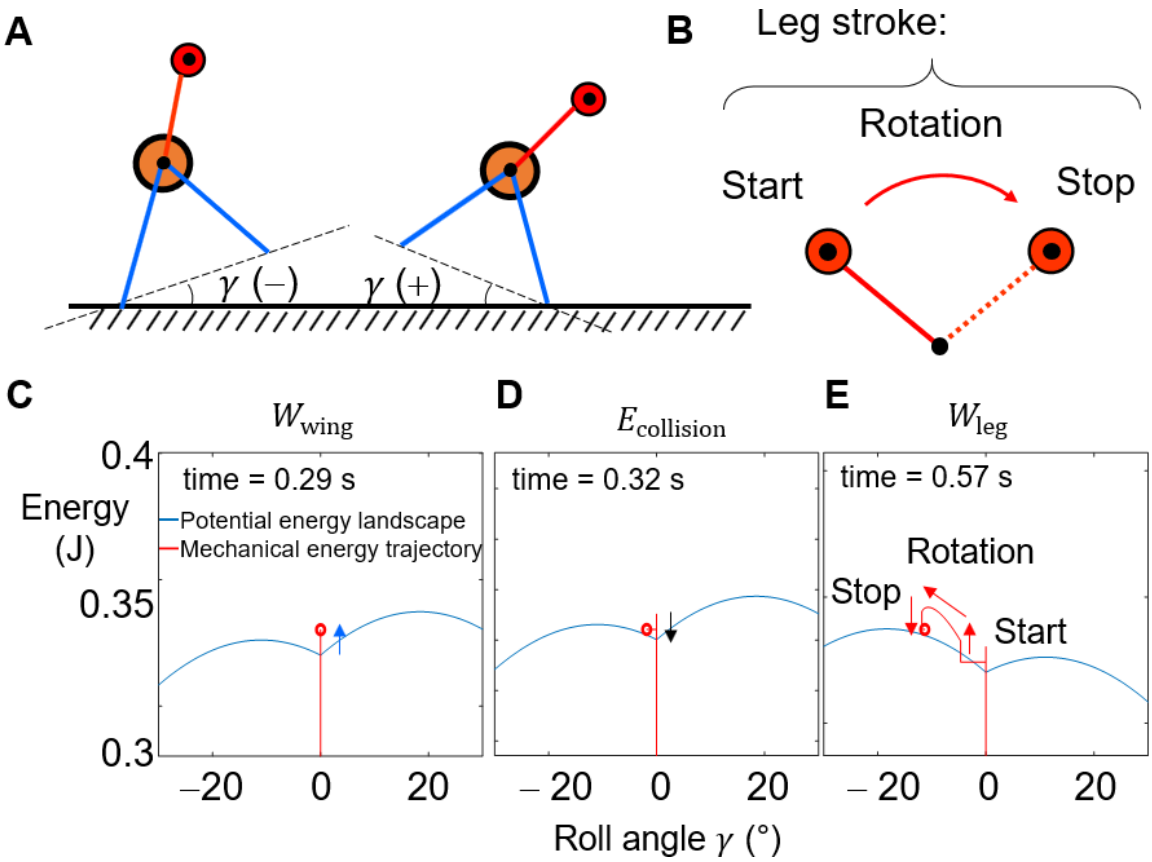

Figure 21. Mechanical energy evolution of system from template. (A) Definition of roll angle. +/– is clockwise/counterclockwise rolling. (B) Definition of a leg stroke. Stroke direction can be reversed. (C-E) Example snapshots of system mechanical energy (red dot) evolution (red trajectory) over changing potential energy landscape over body roll (blue curve). C: When wing opening stops. D: When one wing collides with ground. E. When leg stops. Red curve is trajectory of system state from the beginning (t = 0 s).

We defined wing work W_{wing} as the work done by the wing motors minus the increase of potential energy and frictional dissipation before wing opening stops. For good phases, $W_{wing} = E_0 - E_{min}$, where E_0 is the mechanical energy at the instance when wing opening stops and E_{min} is the local minimum in potential energy landscape. W_{wing} equals the kinetic energy when wing opening stops (**Figure 21**C, blue arrow). For bad phases, $W_{wing} = E_0 - E_{min} - W_{leg\text{-}before}$, where $W_{leg\text{-}before}$ is the work done by the leg motor before wing

opening stops, which is part of the leg work during a stroke W_{leg} (defined below). A leg stroke consists of motor starting, rotation, and stopping (**Figure 21**B).

After wing opening stops, only the leg motor injects energy into the system. We defined leg work W_{leg} as the work done by the first leg stroke. In the example shown, both motor starting and rotation inject energy, whereas motor stopping dissipates energy (**Figure 21**E, red arrows).

After wing opening stops, there is a brief aerial phase. Leg rotation in the aerial phase does not change mechanical energy (Sec. 3.7, Aii). After the aerial phase, mechanical energy is dissipated at collision $E_{collision}$ (**Figure 21**D, black arrow). After the first leg stroke, the leg motor is static for 0.25 s (**Figure 18**B, top). If there is no second collision, the mechanical energy of the template is conserved. If there is a second collision, it further adds to energy dissipation $E_{collision}$.

We defined cumulative mechanical energy at the end of the first leg stroke as:

$$E_{cum} = W_{wing} + W_{leg} - E_{collision} \quad (24)$$

The mechanical energy difference between cumulative mechanical energy and potential energy barrier, $E_{cum} - E_{barrier}$, equals the excess kinetic energy with which the CoM can rotate in an attempt to overcome the potential energy barrier (**Figure 20**, $(M + m)g\Delta h$). Thus, self-righting succeeds if there is a mechanical energy surplus and fails if there is a deficit.

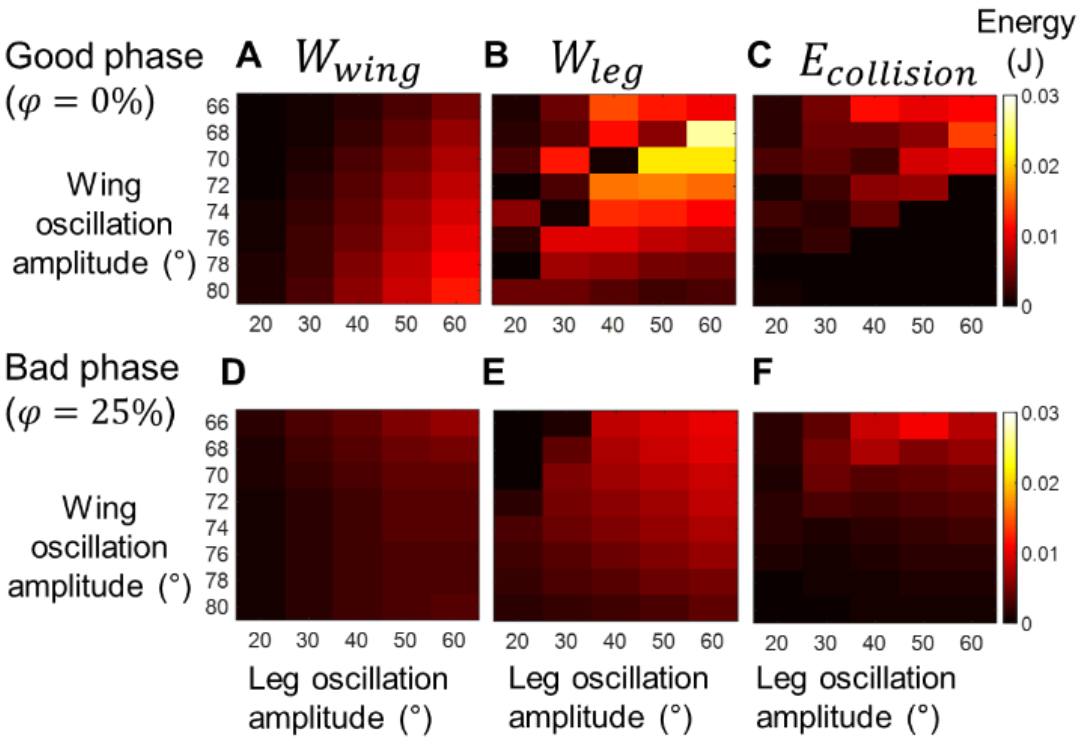

Figure 22. Mechanical energy contributions for example good (top) and bad (bottom) phases. (A, D) Wing work W_{wing} (see definition in text), (B, E) work done by the first leg stroke W_{leg}, and (C, F) energy dissipation at collision $E_{collisoin}$ (absolute value), all as a function of wing opening and leg oscillation amplitudes.

C. Effect of phase

To understand how phase affects system mechanical energy, we calculated contributions to cumulative mechanical energy from wings, leg stroke, and collision (**Figure 22**, W_{wing}, W_{leg}, and $E_{collision}$) for good and bad phases over a broad range of wing opening and leg oscillation amplitudes. Both W_{wing} and W_{leg} consist contributions from instantaneous events and continuous motions, whereas $E_{collisoin}$ is only from instantaneous events. Then, we evaluated mechanical energy budget, $E_{cum} - E_{barrier}$, to understand why good phases lead to more successful self-righting than bad phases.

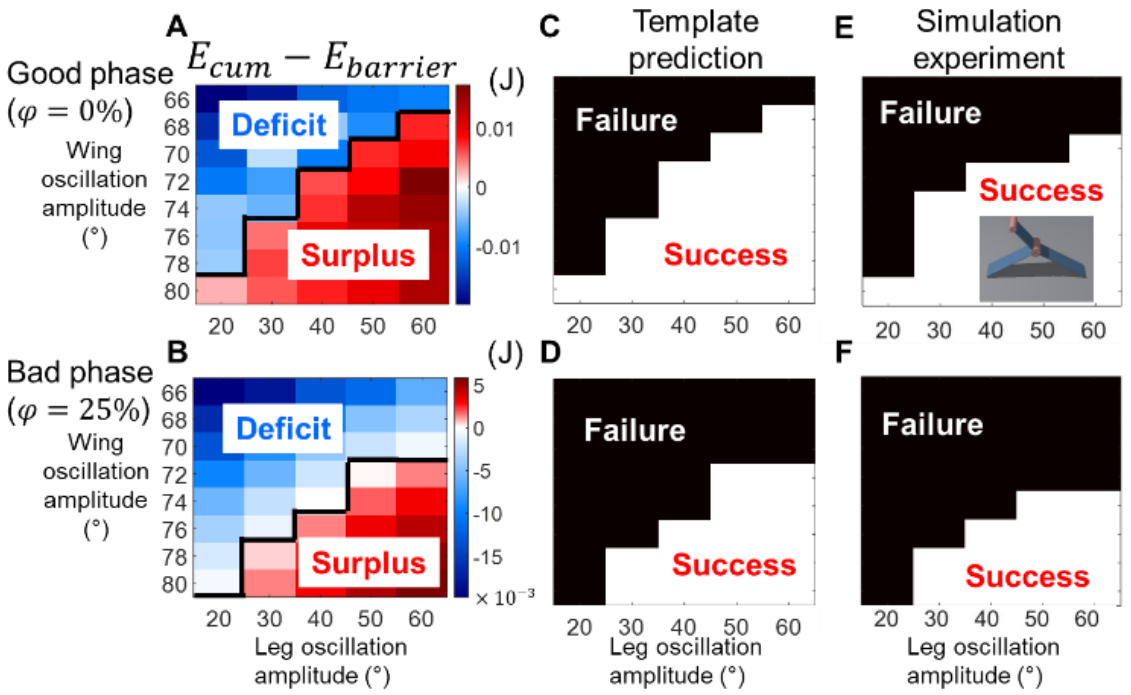

Figure 23. Mechanical energy budget from template predicts self-righting outcome. (A, B) Mechanical energy budget from template—cumulative mechanical energy minus potential energy barrier. (C, D) Self-right outcome predicted by energy budget from template. (E, F) Self-righting outcome of a "2-D" simulation robot (inset in E). Data are shown as a function of wing opening and leg oscillation amplitudes for good (top) and bad (bottom) phases.

For both good and bad phases, the system has an increasing mechanical energy deficit as wing opening and leg oscillation amplitudes decrease, and it has an increasing surplus as they increase (**Figure 23**A, B). Where the template transitions from having an energy surplus to a deficit (**Figure 23**A, B, black curve) predicts where it transitions from success to failure (**Figure 23**C, D). Clearly, good phases lead to greater mechanical energy surplus and smaller deficit than bad phases over the entire parameter space (**Figure 23**A vs. **Figure 23**B), resulting in successful self-righting over a larger range of wing opening and leg oscillation amplitudes (**Figure 23**C vs. **Figure 23**D). These

predictions of self-righting outcome (**Figure 23**C, D) are consistent with previous observations in the 3-D simulation robot (Xuan and Li, 2019).

Considering that our previous observations were made in a different, 3-D robot (Xuan and Li, 2019), to further validate the template, we developed a "2-D" multi-body dynamics simulation robot using Chrono (Tasora et al., 2015) (**Figure 23**B, inset; Movie 4). We chose Chrono because it is good at handling of complex dynamic systems with large number of rigid bodies that interact through repulsive, frictional contact (Tasora et al., 2015). The "2-D" robot has the same design as the template except that, to constrain motion within the transverse plane, it has a finite thickness into the plane. We used Young's modulus E = 1 × 10^5 Pa, Poisson's ration $\nu = 0.1$, coefficient of restitution CoR = 0, coefficient of friction μ = 1, and time step t = 0.00001 s.

By performing simulation experiments over the same range of parameter space, we found that where the "2-D" robot transitioned from success to failure (**Figure 23**E, F) well matched that predicted from mechanical energy budget from the template (**Figure 23**A, B), for both good and bad phases. The slight mismatch likely resulted from deviation from model approximations. For example, collision, acceleration, and deceleration are instantaneous in the template, whereas in simulation, these events are fast but still take time. In addition, there is an overlap at contact in simulation that models deformation, but this is not present in the template.

D. Effect of leg stroke

Our energy calculations also revealed that leg stroke plays a dominant role in self-righting. Although energy contributions from wing opening, leg stroke, and collision depended on phase in complex ways (**Figure 22**), work done by leg stroke W_{leg} is the most sensitive to phase (**Figure 22**B vs. 6E). In addition, the difference in W_{leg} between

good and bad phases (**Figure 22**B vs. **Figure 22**E) is the greatest around the transition boundary in mechanical energy budget (**Figure 23**A).

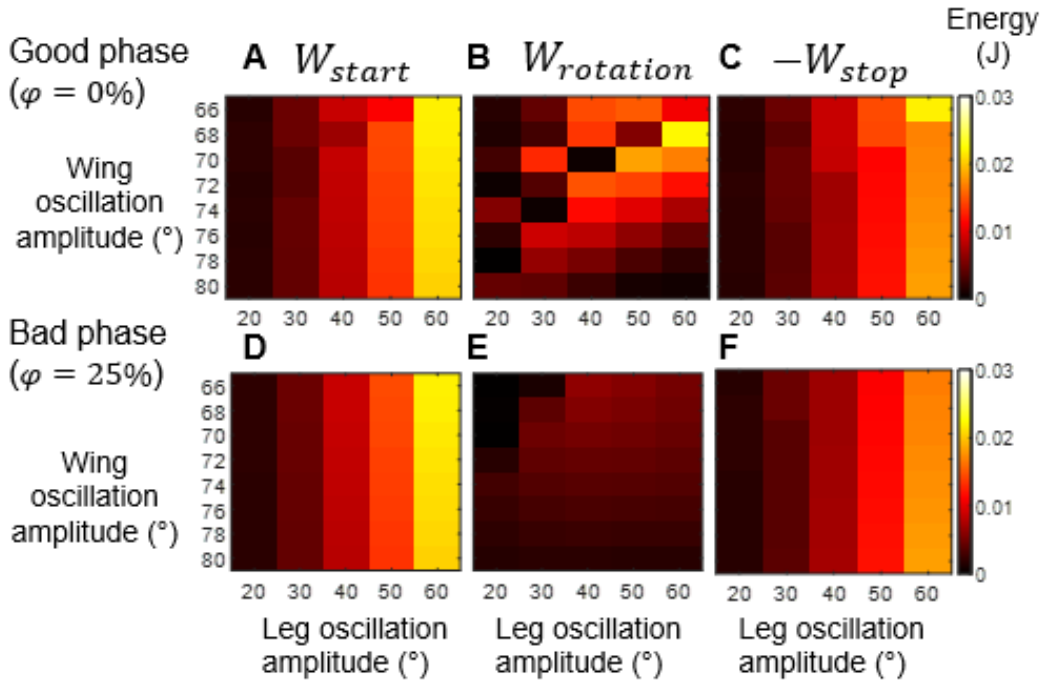

Figure 24. **Contributions to W_{leg} from leg starting W_{start}, rotation $W_{rotation}$, and stopping W_{stop} for example good (top) and bad (bottom) phases.**

W_{leg} has three contributions (**Figure 24**) from leg motor starting, stopping, and rotation (**Figure 21**B, E). W_{start} and W_{stop} are from instantaneous events, insensitive to phase (**Figure 24**A, C vs. D, F), and nearly cancel each other (**Figure 24**A, D vs. C, F). By contrast, $W_{rotation}$ depends sensitively on phase (**Figure 24**B vs. E).

3.9 Template-predicted control

Because the template describes system dynamics fully and was validated against simulation experiments, we can use it for predictive robot control. To demonstrate this, we

used the template to predict a new control strategy to further increase self-righting performance.

Because W_{rotation} plays a dominant role in mechanical energy budget (Sec. 3.8, D), our new control strategy maximizes work done by the leg during rotation:

$$W_{\text{rotation}} = \int_{-\theta_L}^{\theta_L} \tau_{leg} d\theta \tag{25}$$

where τ_{leg} is leg motor torque. We calculated leg torque as a function of time:

$$\tau_{leg}(t) = \frac{dW_{leg}(t)}{d\theta(t)} = \frac{dW_{leg}(t)}{dt}\frac{dt}{d\theta(t)} = \frac{dW_{leg}(t)}{\omega dt} \tag{26}$$

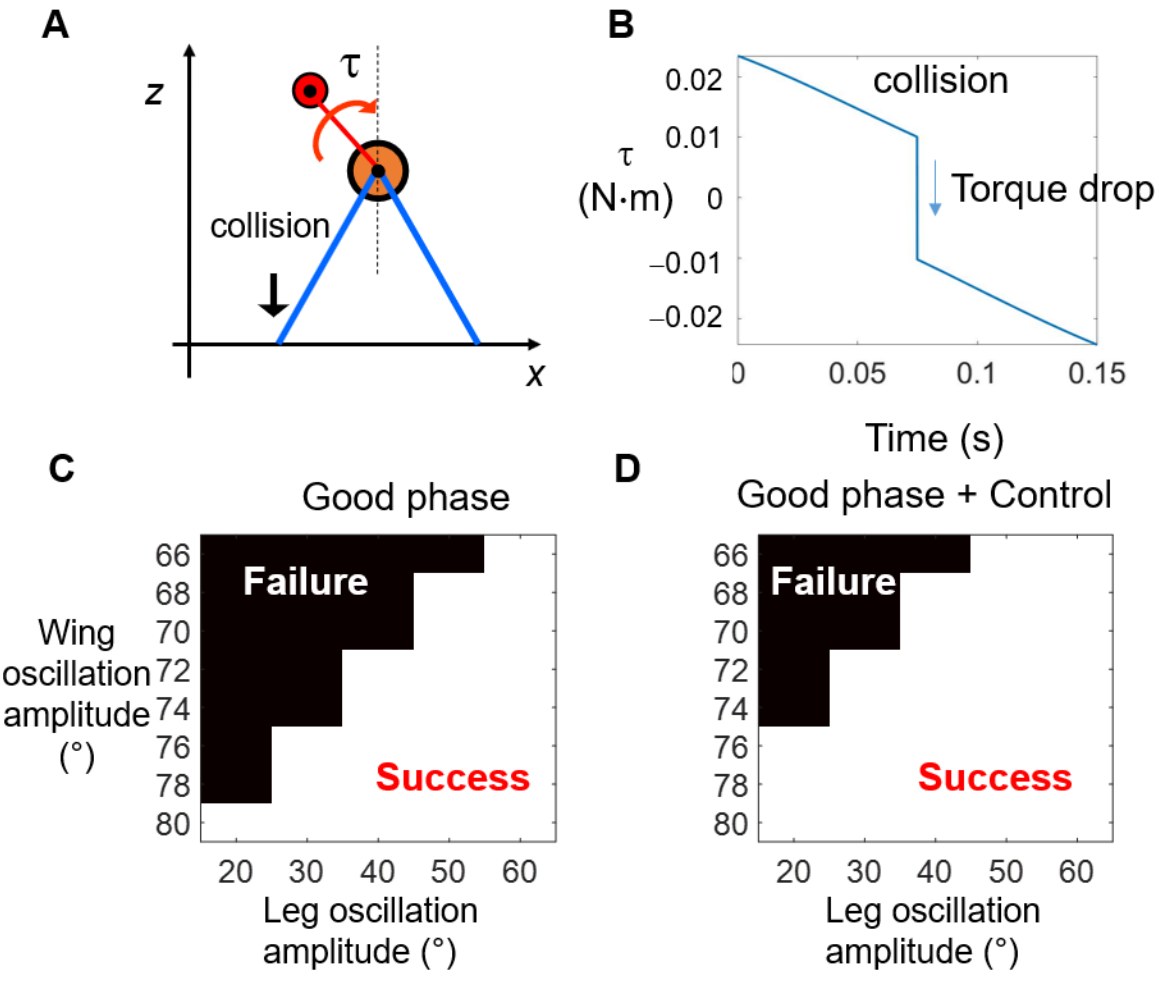

Figure 25. Template-predicted control. (A) A collision with ground occurs during a leg stroke. τ is leg motor torque. (B) Leg motor torque τ as a function of time during a leg stroke. Torque drops at collision. (C, D) Self-righting outcome predicted from template with (C) and without (D) control using a good phase (φ = 50%), both as a function of wing opening and leg oscillation amplitudes.

Our calculation revealed that, when a wing collides with the ground (**Figure 25**A), leg torque drops instantaneously (**Figure 25**B). From Eqn. 4, W_{rotation} is maximized when τ_{leg} is maximized, because integration interval is fixed. Thus, our control strategy maximized W_{rotation} by maximally delaying collision during leg stroke, or avoiding collision altogether.

To achieve this, we start the leg motor immediately after collision, so that the leg stroke does positive work for a longer time before the next collision. This is considering that the time interval between two collisions is nearly unaffected by leg motor starting, because CoM angular momentum relative to the contacting wing tip stays unchanged during leg motor starting (Sec. 3.7, Biii).

We used the template to test our control strategy. Indeed, self-righting performance was further improved (**Figure 25**D) beyond achievable by using good phase alone (**Figure 25**C).

3.10 Template-informed design

Next, we use the template to analyze how system parameters affect cumulative mechanical energy and the potential energy barrier to inform robot design.

First, the potential energy barrier is a function of six system parameters (wing and leg angles, body and leg pendulum masses, and body and leg lengths), i.e., $E_{\text{barrier}} = E\text{-}_{\text{barrier}}(\theta_W, \theta_L, M, m, R, r)$. If E_{barrier} is monotonic to a parameter, one can increase or decrease

this parameter to reduce $E_{barrier}$ for easier self-righting. Thus, we calculated the partial derivative of $E_{barrier}$ over each parameter. If the partial derivative is always ≥ 0 or ≤ 0, $E_{barrier}$ increases or decreases monotonically with this parameter regardless of other parameters. We randomly sampled 100 initial conditions and numerically searched for the maximum and minimum of each partial derivative, with the constraint that the projection of CoM on the ground is between two wing tips.

We found that $E_{barrier}$ decreases monotonically with wing angle θ_W and leg length r and increases monotonically with body mass M and wing length R, regardless of other parameters. However, $E_{barrier}$ does not always increase or decrease monotonically with leg angle θ_L and leg pendulum mass m regardless of other parameters.

Second, cumulative mechanical energy depends on nine system parameters, including wing opening speed ω_W, leg rotation speed ω_L, duration of leg rotation, and the six above. However, because cumulative mechanical energy does not have an analytical form because of the hybrid dynamics, we have not systematically studied how it depends on parameters. Considering that leg velocity is typically much larger than body velocity, kinetic energy of the leg pendulum is:

$$E_{kL} \sim \frac{1}{2} m r^2 {\omega_L}^2 \tag{27}$$

Thus, increasing m, r, ω_L will increase cumulative mechanical energy. In addition, increasing θ_W will reduce collision dissipation by reducing the moment arm of collision force and thus increase cumulative mechanical energy.

Based on the above, having wings that can open by a larger angle and longer legs that flail faster will likely make a good design for both robots and animals for leg-assisted, winged self-righting. These insights into appendage design added to our knowledge of

how body geometry (e.g. turtle shells (Domokos and Várkonyi, 2008), body aspect ratios (Li et al., 2019a)) affects ground self-righting.

3.11 Future work

We developed a template of leg-assisted, winged ground self-righting and used it to elucidate why wing-leg coordination affected self-righting outcome. With good coordination, the system better accumulates mechanical energy to overcome the potential energy barrier and thus self-rights more successfully. Besides providing mechanistic understanding of this complex hybrid dynamical system, we demonstrated practical usefulness of the template by predicting a new control strategy that further improves self-righting performance. We also used the template to examine how system parameters may affect cumulative mechanical energy and the potential energy barrier to inform robot design. More broadly, our study highlighted the importance of appendage coordination for appropriately cumulating mechanical energy to overcome potential energy barriers in strenuous locomotor transitions. An energy landscape approach to locomotor transitions (Othayoth et al., 2020) will facilitate this progress (Gart and Li, 2018; Han et al., 2017; Li et al., 2019a; Othayoth et al., 2017; Wang et al., 2020).

Our template opens an avenue for further studies of leg-assisted, winged ground self-righting. Morphological and actuation details can be added to create models anchored into the template (Full and Koditschek, 1999; Lee et al., 2008) for studying more complex self-righting strategies. For example, we can use two ellipses with distributed mass to model the body with bending abdomen observed in the animal (Li et al., 2019a) and add multiple oscillating pendulum legs to study how wings, legs, and abdomen coordinate together. We can also revise rigid wing links into wing springs to study how wing deformation affects energy cumulation, as the thin wings can deform under load. Finally,

it will be intriguing to use the template to study how animals and robots can sense their state and interaction with the ground to better coordinate appendages to self-right.

Chapter 4

Environmental force sensing helps robots traverse cluttered large obstacles

This chapter was previously posted on arXiv as a preprint entitled *Environmental force sensing helps robots traverse cluttered large obstacles* authored by Qihan Xuan and Chen Li. This work has also been submitted to *Bioinspiration and Biomimetics* and has been accepted at the time of submission of this dissertation.

4.1 Author contributions

Qihan Xuan designed study, developed simulation, performed experiments, analyzed data, and wrote the paper; Chen Li designed and oversaw study and revised the paper.

4.2 Acknowledgements

We thank Ratan Othayoth, Yaqing Wang, and Qiyuan Fu for discussion. This work was supported by an Arnold & Mabel Beckman Foundation Beckman Young Investigator Award, a Burroughs Wellcome Fund Career Award at the Scientific Interface to C.L.

4.3 Summary

Robots can traverse sparse obstacles by sensing environmental geometry and avoiding contact with obstacles. However, for search and rescue in rubble, environmental monitoring through dense vegetation, and planetary exploration over Martian and lunar rocks, robots must traverse cluttered obstacles as large as themselves by physically interacting with them. Previous work discovered that the forest floor-dwelling discoid cockroach and a sensor-less minimalistic robot can traverse cluttered grass-like beam obstacles of various stiffness by transitioning across different locomotor modes. Yet the animal was better at traversal than the sensor-less robot, likely by sensing forces during obstacle interaction to control its locomotor transitions. Inspired by this, here we demonstrated in simulation that environmental force sensing helps robots traverse cluttered large obstacles. First, we developed a multi-body dynamics simulation and a physics model of the minimalistic robot interacting with beams to estimate beam stiffness from the sensed contact forces. Then, we developed a force feedback strategy for the robot to use the sensed beam stiffness to choose the locomotor mode with a lower mechanical energy cost. With feedforward pushing, the robot was stuck in front of stiff beams if it has a limited force capacity; without force limit, it traversed but suffered a high energy cost. Using obstacle avoidance, the robot traversed beams by avoiding beam contact regardless of beam stiffness, resulting in a high energy cost for flimsy beams. With force feedback, the robot determined beam stiffness, then traversed flimsy beams by pushing them over and stiff beams by rolling through the gap between them with a low energy cost. Stiffness estimation based on force sensing was accurate over a wide range of robot body oscillation amplitude and frequency and position sensing uncertainty.

Mechanical energy cost of traversal increased with sensorimotor delay. Future work should demonstrate cluttered large obstacle traversal using force back in a physical robot.

4.4 Introduction

Mobile robots are becoming increasingly prevalent in society. Many robots already excel at navigating on flat surface and avoiding sparse obstacles by sensing environmental geometry, like robot vacuum cleaners (Tribelhorn and Dodds, 2007) and self-driving vehicles (Thrun et al., 2000). Sensors like cameras, radars, and LiDAR are used to create a geometric map of the surroundings, then a collision-free path is planned to avoid physical contact with obstacles (Borenstein and Koren, 1991; Elfes, 1989; Gamini Dissanayake et al., 2001; Khatib, 1985; Rimon and Koditschek, 1992). However, for search and rescue through earthquake rubble (Pratt, 2014; Reddy et al., 2015), environmental monitoring through dense vegetation (Oliveira et al., 2021), and extraterrestrial exploration through Martian and lunar rocks (Li and Lewis, 2022), robots often need to traverse complex 3-D terrain with densely cluttered obstacles as large as themselves by physically interact with the obstacles. In these situations, geometry-sensing based obstacle avoidance faces difficulties. Firstly, a collision-free path might not always be available. Secondly, even if such a path exists, it could be energetically costly or need an extended execution time, as the robot may need to take long detours to circumvent obstacles. Additionally, if the robot fails to avoid obstacles promptly, unexpected collisions and contact could cause it to flip over (Guizzo and Ackerman, 2015a; Li et al., 2017).

Understanding how to utilize and control physical interaction with the environment (environmental affordance (Gibson, 1979; Roberts et al., 2020)) is fundamental to locomotion. For example, understanding of terramechanics (Bekker, 1960; Wong, 2009)

has helped wheeled vehicles off-road deformable ground. Understanding leg-ground interaction on rigid ground (Blickhan and Full, 1993; Kuo, 2007; Raibert, 1986) has provided the foundation for legged robots to walk and run on flat surfaces with small unevenness. Recent research into leg interaction with granular media has facilitated the robotic design and control to improve legged and even (surprisingly) wheeled locomotion on deformable ground (Agarwal et al., 2021; Aguilar and Goldman, 2016; Li et al., 2013; Lynch et al., 2020; Qian et al., 2015; Shrivastava et al., 2020).

Biological organisms provide rich sources of inspiration for understanding and controlling the physical interaction of robots with obstacles to improve their traversal in complex 3-D terrains with cluttered large obstacles. An excellent model organism is the forest floor-dwelling discoid cockroach recognized for its exceptional ability to traverse vegetation, foliage, and rocky crevices (Li et al., 2015; Sponberg and Full, 2008). Recent studies have shed considerable light on how these creatures use effective body and leg interaction with obstacles to traverse cluttered large obstacles via integration of biological experimentation (Li et al., 2015; Othayoth and Li, 2021; Wang et al., 2022), robophysical modeling (Gart and Li, 2018; Gart et al., 2018; Han et al., 2021; Mi et al., 2022; Othayoth and Li, 2021; Othayoth et al., 2020), and theoretical and computational modeling (Zheng et al., 2021).

Prior research discovered that the discoid cockroach can traverse grass-like beam obstacles using and transitioning across different modes of locomotion (Li et al., 2015). For example, the animal simply pitches up the body to push over flimsy beams (**Figure 26**A, blue), whereas it often transitions (**Figure 26**A, yellow) to rolling (**Figure 26**A, red) into a gap to maneuver through stiff beams (Othayoth et al., 2020). Its legs continuously pushed against the ground, inducing oscillatory self-propulsion during traversal (Othayoth et al., 2020).

To study the principles of locomotor mode transitions, a sensor-less, feedforward, minimalistic robophysical model was developed (**Figure 26**B) (Othayoth et al., 2020). The robot, featuring an ellipsoid-like body without legs, was propelled forward at a consistent speed. Its body oscillated to emulate the oscillatory self-propulsion of the animal. This robot was free to pitch and roll in response to interaction with two beams. The grass-like beams were modeled as two plates with torsion springs at their base on the ground. Utilizing this robot, researchers discovered the mechanism of locomotor mode transitions under passive interaction with obstacles (Othayoth et al., 2020). A potential energy landscape model showed that the pitch and roll modes arose as the system was attracted to distinct pitch and roll basins on a potential energy landscape, respectively (Othayoth et al., 2020). Systematic experiments using this robot demonstrated that locomotor transition from pitch to roll mode occurred when kinetic energy fluctuation from body oscillations exceeded the potential energy barrier between the pitch and roll basins (Othayoth et al., 2020).

However, although both the animal and robot can traverse cluttered grass-like beam obstacles of a range of stiffness, the animal was still better at traversing. The animal often made the transition even when the kinetic energy fluctuation from body oscillations alone was insufficient for overcoming the potential energy barrier (Othayoth et al., 2020), possibly by utilizing force sensing during environmental interaction to actively control its locomotor mode transitions. This was partly substantiated by a subsequent study which found that the animal actively adjusted their body and appendages (e.g., head, abdomen, and legs) when transitioning from the pitch to the roll mode (Wang et al., 2022).

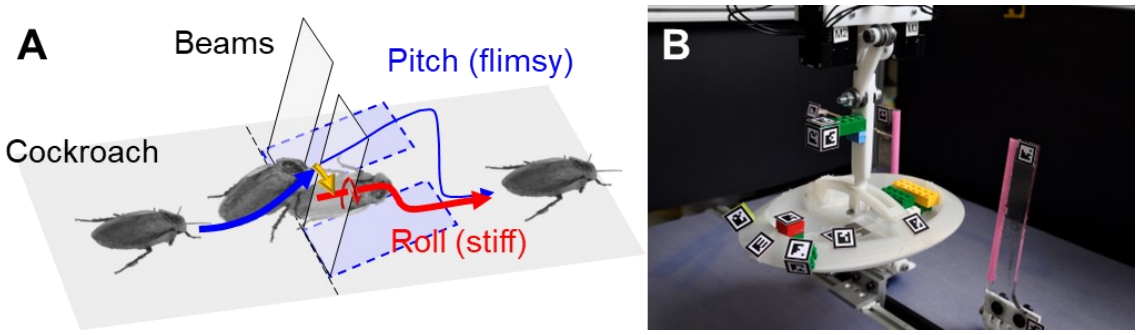

Figure 26. Discoid cockroach and robophysical model traverse grass-like beam obstacles using physical interaction. (A) For flimsy beams, the discoid cockroach predominantly uses a pitch mode (blue), while for stiff beams, it predominantly transitions (yellow) to a roll mode (red) (Othayoth et al., 2020). (B) A minimalistic robophysical model of cockroach beam traversal (Othayoth et al., 2020).

Here, we further studied how force sensing during body-obstacle interaction could help active locomotor mode transitions. We chose to use the minimalistic, legless robot design because it provides an ideal, simplified system to focus on sensing and controlling body-obstacle interaction, which is important to locomotor transitions through cluttered large obstacles (Othayoth et al., 2020). The potential energy landscape model in the previous study did not fully model the dynamics of the system (Othayoth et al., 2020), limiting our ability to explore the impact of force sensing. To address this, we developed a multi-body dynamics simulation of the minimalistic robot with force sensing and feedback (Sec. 4.5.1). While environmental force sensing capabilities have been developed for some bio-inspired legged robots (Arena et al., 2015; Bhattacharya et al., 2020; Kimura et al., 2001; Shill et al., 2015; Walas, 2013; Wu et al., 2016), they only detect contact force between the robot feet and the ground. Creating a refined robot capable of sensing body-obstacle contact forces and torques requires integrating distributed force sensors that cover the body surface and developing feedback control algorithms to control body

rotations. This is a major undertaking and is beyond the scope of this study.

We developed a force feedback strategy to use the robot's body force sensing to estimate the physical properties of the beams and alter the traversal method for different beams. In addition, we developed a physics model of the system that integrated a contact force model and the corresponding equations of motion (Sec. 4.5.2). The physics model allowed us to estimate the beam stiffness from the contact forces. We performed simulation studies to compare strategies with and without force sensing (Sec. 4.5.3). Our force feedback strategy first estimated beam stiffness based on force sensing and a contact force model (Sec. 4.5.4). We then used the potential energy landscape model to classify beams as either stiff or flimsy to guide the robot to choose a locomotor mode with a lower energy cost (Sec. 4.5.5). Using this information, we performed motion planning to generate robot trajectory (Sec. 4.5.6). Our simulation also allowed us to vary body oscillations and randomness during traversal to examine their influence on our strategy. Oscillation is a naturally occurring phenomenon during traversal. The discoid cockroach displays substantial body oscillations while traversing due to their legs periodically pushing against the ground (Othayoth et al., 2020). Oscillations lead to intermittent contact instead of steady contact, which can make position sensing less accurate and presents increased challenges in modeling contact forces and estimating stiffness.

To evaluate the usefulness of the force feedback strategy, we conducted a series of simulation studies. First, we analyzed simulations of a robot traversing both stiff and flimsy beams without force sensing and studied its three different strategies (Sec. 4.6.1). We studied feedforward pushing strategy (Sec. 4.6.1.1) and obstacle avoidance strategy (Sec. 4.6.1.3) to provide a baseline. Considering that in real-world scenarios both animals and robots have finite force/torque capacities, we next studied feedforward pushing

strategy with force/torque limits (Sec. 4.6.1.2). Second, we tested the robustness of the force feedback strategy against body oscillations with randomness and inaccuracies in position sensing (Sec. 4.6.2) to compare with the baseline. Third, to access the advantages of the force sensing and active feedback control, we conducted simulations with the force feedback control strategy and compared results with those from previous non-force sensing strategies (Sec. 4.6.3). Furthermore, as the sensorimotor delay is inevitable in both animals and robots, we used our simulation to study the influence of sensorimotor delay on traversal performance (Sec. 4.6.4). Finally, we discussed the limitations of our method, its broader applications, and future work (Sec. 4.7).

4.5 Methods

In this section, we first describe how we developed a physics-based simulation of a minimalistic robot interacting with beams, incorporating body force sensing (Sec. 4.5.1). Then, we define the physics model that integrated a contact force model along with the corresponding equations of motion (Sec. 4.5.2). Next, we describe how the force feedback strategy used force sensing and potential energy landscape to guide the robot to select a locomotor mode that minimized energy consumption (Sec. 4.5.4, 4.5.5, and 4.5.6). We formulated the energy cost during traversal and conducted simulations to compare strategies with and without force sensing (Sec. 4.5.3, 4.5.7, and 4.5.8). Lastly, we experimented with varying the sensorimotor delay in force feedback control (Sec. 4.5.9).

4.5.1 Simulation of robot traversing beams with body force sensing

We developed a physics-based simulation as a platform to explore the benefits of sensing contact forces between the robot body and obstacles and using this information to enhance its ability to traverse beams. The simulation robot (**Figure 27**A) was built in Chrono, an open-source multi-body dynamics engine (Mazhar et al., 2013; Tasora et al.,

2015), following the design in previous study (Othayoth et al., 2020). It was modeled as a rigid ellipsoidal body similar to the discoid cockroach's body, with principal axes lengths $2a = 0.22$ m, $2b = 0.16$ m, and $2c = 0.06$ m. An additional weight of 0.5 kg made it bottom-heavy, with the center of mass at $h_c = 0.01$ m below the geometric center (**Figure 28**A). The ellipsoidal body's total mass $M = 1$ kg and its moments of inertia along the three principal axes were $(I_x, I_y, I_z) = (3.9, 7.5, 10.9) \times 10^{-3}$ kg·m^2. The geometric center was $H_o = 0.105$ m from the ground before moving.

The ellipsoidal body had three degrees of freedom in translation and two degrees of freedom in rotation (**Figure 27**A). Although the robot was equipped with three linear actuators for 3-D translation, it was primarily propelled forward by a linear actuator along the *X*-axis. The lateral and vertical actuators only generated oscillations that allow for slight movements (~ 2 mm) along the *Y*- and *Z*-axes. In accordance with the previous design (Othayoth et al., 2020), two rotation axes, which were the roll axis (**Figure 27**, red dashed line) and the pitch axis (**Figure 27**, blue dashed line). Two motors controlled the ellipsoidal body's rotation to emulate the animal's active pitch and roll adjustments. The center of the rotation overlapped with the geometric center. Thus, body orientation can be represented by roll angle α and pitch angle β. The body was in static equilibrium when both its roll angle α and pitch angle β were 0°.

Following previous work (Othayoth et al., 2020), the grass-like beams were designed as rigid, vertical plates with torsion springs at their base, and they could deflect about *Y*-axis. The torque function of the spring was $\tau_s = k\theta - c_d\omega$, where *k* was stiffness, θ was the relative beam deflection angle, c_d was the damping coefficient ($c_d = 0.01\ N \cdot m \cdot s/rad$), and ω was the beam's deflection angular velocity. Note that here we added an additional damping term to represent the energy dissipation occurring during the beam's

motion. The mass of each beam was m = 1 g. The two torsion springs were symmetric about the *X*-*Z* plane. The two beams were vertical when there was no deflection. The gap width between the two beams was d = 0.138 m, which was narrower than the robot body width. Each beam's height, width, and thickness were L = 0.155 m, w = 0.04 m, and h = 0.01 m (**Figure 28**B).

We used the Discrete-Element Method with penalty (DEM-P) in the Chrono framework, which characterizes contact through a viscoelastic force model (Fleischmann, 2015; Tasora et al., 2015).

$$\begin{cases} \boldsymbol{F}_n = f(\bar{R}, \delta_n)(k_n \boldsymbol{\delta}_n - \gamma_n \bar{m} \boldsymbol{v}_n) \\ \boldsymbol{F}_t = f(\bar{R}, \delta_n)(-k_t \boldsymbol{\delta}_t - \gamma_t \bar{m} \boldsymbol{v}_t) \end{cases} \quad (28)$$

Here, the vector sum of δ_n (normal) and δ_t (tangential) was the displacement vector at the contact point between two bodies, which symbolizes their overlap in the absence of deformation. The effective mass $\bar{m}$ and the effective radius of curvature $\bar{R}$ are defined as $\bar{m} = \frac{m_1 m_2}{m_1 + m_2}$ and $\bar{R} = \frac{R_1 R_2}{R_1 + R_2}$. $k_n, k_t, \gamma_n, \gamma_t$ are the normal and tangential stiffness and damping parameters, respectively. They are all dependent on $\bar{m}$, $\bar{R}$, and the material properties of the interacting bodies, including Young's modulus (E), Poisson's ratio (v), and the coefficient of restitution (CoR). In our particular design, contact occurred exclusively between the robot's body and the beams. We set their Young's modulus = 10^6 Pa, Poison's ratio = 0.1, coefficient of restitution = 0, and coefficient of friction = 0. Within the Chrono simulation, we could determine the position and orientation of the body and beams (environmental geometry sensing), as well as their contact forces (environmental force sensing). Thus, in simulation, we could control the motors based on these sensory inputs (feedback control).

To validate the simulation, we replicated the experiments from previous research conducted with a real robot (Othayoth et al., 2020). Consistent with the previous findings, we verified that the oscillatory motion aided the robot in transitioning from pitching to rolling to traverse beams via passive interaction with the beams (**Figure 27**B, C).

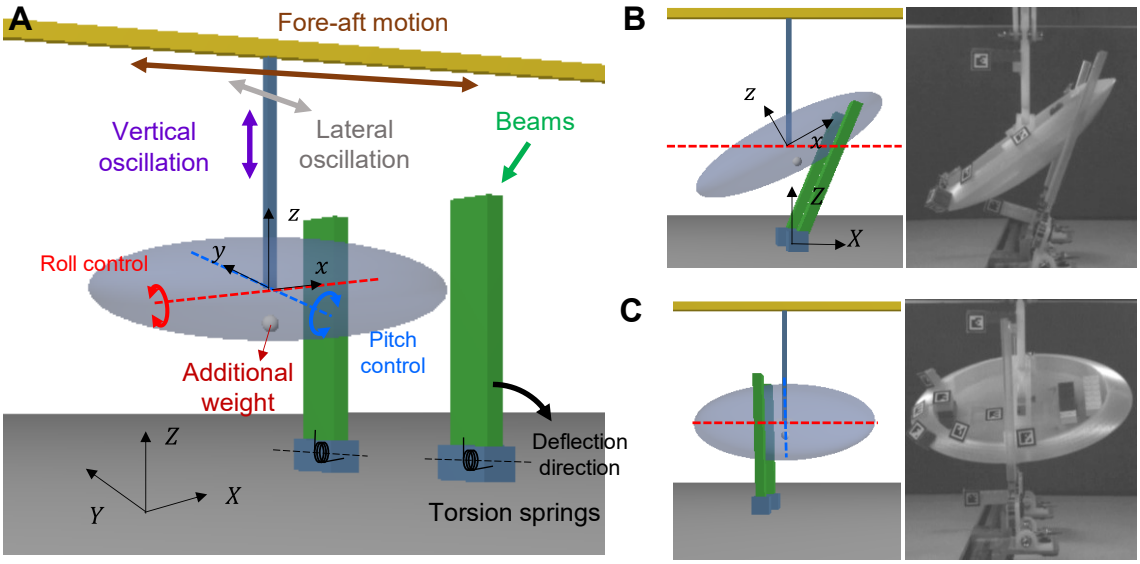

Figure 27. Multi-body dynamic simulation of minimalistic robot traversing beam obstacles. (A) The simulation robot body has five degrees of freedom, fore-aft, vertical, lateral, roll (red arrow), and pitch (blue arrow), which are controlled by motors. The roll axis (red dashed line) is an axis through the rotation center of the robot and parallel to the *X*-axis of the world frame. The pitch axis (blue dashed line) is the *y*-axis in the body frame. An additional weight makes it bottom-heavy. Each beam is connected to the ground via a torsion spring and can deflect in the vertical $X - Z$ plane. The world frame is $X - Y - Z$. Body frame is $x - y - z$, which is attached to the robot. (B-C) Snapshots of simulation and physical robot experiments from our previous study (Othayoth et al., 2020). (B) Without vertical oscillations, both simulation and physical robots are stuck in the pitch mode. (C) With sufficient vertical oscillations, both roll into the beam gap and traverse using the roll mode.

4.5.2 Physics model of body-beams interaction

We built a physics model (**Figure 28**) based on the simulation robot design to estimate the beams' stiffness using environmental force sensing. The physics model consisted of the contact force model and equations of motion.

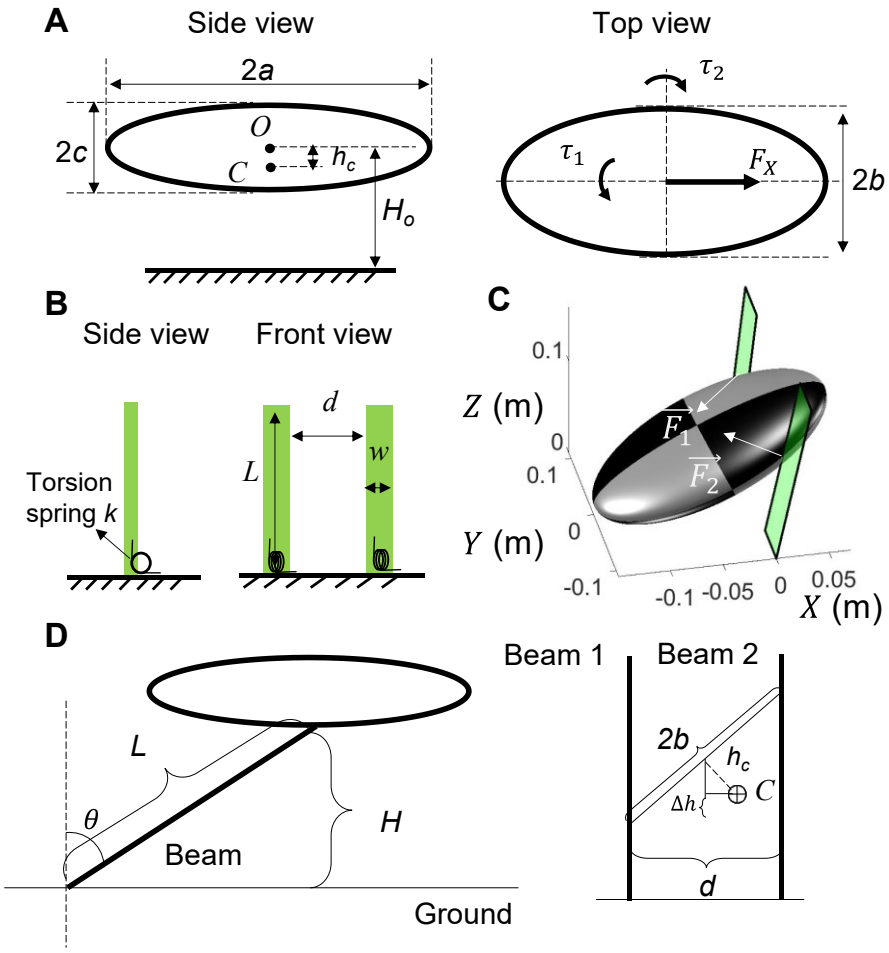

Figure 28. Physics model of robot-beam interaction. (A) Cockroach-inspired robot is modeled as an ellipsoidal rigid body. F_X is propulsive force. τ_1 and τ_2 are roll and pitch torques along the roll and pitch axes in **Figure 27**. The center of mass (C) is lower than the geometric center (O, the intersecting point of roll and pitch axes) by h_c. (B) Each beam is modeled as a rigid plate with a torsion spring with stiffness k. (C) $\vec{F}_1$ and $\vec{F}_2$ are theoretical contact forces with each beam

calculated from the model. (D) Left: In the pitch mode, the potential energy is at a maximum when the bottom of the robot reaches the top of the beam. Right: In the roll mode, the potential energy is at a maximum when the robot rolls until there is no beam contact.

Besides the input force F_x and torques (τ_1, τ_2) from actuators acting on the simulation robot (**Figure 28**A), there were three external forces–gravitational force $\vec{G}$ and contact forces $(\vec{F}_1, \vec{F}_2)$ with two beams (**Figure 28**C). Given these, we could calculate the total force $\vec{F}$ and torque $\vec{\tau}$. Thus, applying Newton–Euler equations, the equations of motion of the robot were:

$$\begin{pmatrix} \vec{F} \\ \vec{\tau} \end{pmatrix} = \begin{pmatrix} M & 0 \\ 0 & I_{CoM} \end{pmatrix} \begin{pmatrix} \vec{\alpha} \\ \vec{\beta} \end{pmatrix} + \begin{pmatrix} 0 \\ \vec{\omega} \times I_{CoM}\vec{\omega} \end{pmatrix} \tag{29}$$

where M was the mass, I_{CoM} was the moment of inertia about the center of mass, $\vec{\alpha}$ and $\vec{\beta}$ were acceleration and angular acceleration about the center of mass, and $\vec{\omega}$ was the angular velocity. In addition, we assumed that actuators would not recycle energy. For example, when the body rolls back to a lower energy state, the decrease in mechanical energy is not returned. Thus, energy is dissipated by motor doing negative work, leading to a mechanical energy cost.

Because the beams were much lighter than the robot, the inertial force of the beam was negligible compared to the contact forces. Therefore, we assumed that each beam was quasi-static and satisfied torque equilibrium during contact.

$$k_i\theta_i - c_{di}\omega_i + \vec{r}_{bi} \times \vec{F}_i \cdot \begin{pmatrix} 0 \\ 1 \\ 0 \end{pmatrix} = \frac{1}{2}mgL\sin\theta_i \tag{30}$$

where k_i and c_{di} were the stiffness and damping coefficients of the ith beam, θ_i and ω_i were its beam deflection angle and angular velocity, $\vec{r}_{bi}$ was the distance from the revolute

axis of the ith beam to the point of application of $\vec{F}_i$.

Because the robot's body surface was smooth, the coefficient of friction was set to 0 in the simulation. Thus, the contact force was normal to the tangent plane of the contact point on the ellipsoidal body's surface.

The normal direction of the ellipsoidal body's tangent plane at a point (x, y, z) in the body frame was:

$$\vec{n} = (b^2c^2x, a^2c^2y, a^2b^2z) \tag{31}$$

Given the current position and orientation of the robot and Eqns. 30 and 31, the theoretical contact forces $\vec{F}_1$ and $\vec{F}_2$ in the world frame was a function of stiffness k_1 and k_2.

4.5.3 Simulation studies to compare between without and with force sensing

We conducted simulations to investigate the traversal of beams with varying stiffness under different strategies. We first studied traversing both flimsy and stiff beams (defined in Sec. 4.5.5) without force sensing, using three different strategies: feedforward pushing without force/torque limits (Sec. 4.6.1.1), feedforward pushing with force/torque limits (Sec. 4.6.1.2), and avoiding obstacles (Sec. 4.6.1.3). Then, we studied traversal of both stiff and flimsy beams using our force feedback strategy (Sec. 4.6.3).

For the feedforward pushing strategy without force/torque limits, the robot had an arbitrarily large propulsive force to maintain a forward speed of $v_X = 0.05$ m/s, with no control exerted over pitch and roll directions.

For the feedforward pushing strategy with force/torque limits, we set $|F_x| \leq 1\ \mathrm{N}, |\tau_1| \leq 0.1\ \mathrm{N \cdot m}, |\tau_2| \leq 0.1\ \mathrm{N \cdot}$

m to examine more realistic traversal with force and limits. When any force or torque component of $\vec{u}$ calculated from Eqn. 34 exceeded its limit, this component was set to be the maximum or minimum values within the limit.

For the obstacle avoidance strategy, we used environmental geometry to determine the minimal angle required for the robot to roll to traverse the beams without contacting them. The robot maintained a forward speed of $v_X = 0.05$ m/s utilizing roll control to rotate its body and avoid contact. Although the above force/torque limits were also applied in this scenario, the absence of contact resulted in no resistance, so these limits were not reached.

For the force feedback strategy, we first estimated beam stiffness based on the body contact force (sensing time $T_s = 100$ ms) sensed after the initial contact. Then, we constructed a potential energy landscape and performed motion planning. Finally, we controlled the robot to track planned trajectories to traverse flimsy and stiff beams. Detailed discussions on the motion planning and control were provided in Sec. 4.5.6 and 4.4.7. To be fair in comparison, the same force/torque limits were also applied in this scenario.

4.5.4 Estimating beam stiffness from force sensing

4.5.4.1 Varying vertical and lateral body oscillations with randomness

To investigate the impact of naturally occurring random body oscillations (Othayoth et al., 2020) on our beam stiffness estimation method, we simulated the robot's movement with lateral and vertical oscillations, generated by linear actuators (**Figure 27**A). The lateral oscillation followed the triangle wave function, with the frequency *f* and amplitude *A*. The vertical oscillation followed a sum of 30 sine functions to induce randomness. The

sum of sine functions is a strategy employed in various research contexts to introduce unpredictable external stimuli (Roth et al., 2011; Roth et al., 2016; Zimmet et al., 2020). The amplitude of each sine function was randomly selected from −0.5 mm to 0.5 mm, and the phase was randomly chosen from − π to π. The frequencies of 30 sine functions were $\frac{f}{50}, \frac{2f}{50}, \frac{3f}{50}, \ldots, \frac{30f}{50}$. We conducted the simulations with varying oscillation amplitude (A = 1, 2, 3 mm) and frequency (f = 2, 4, 6 Hz), while assuming that the position sensing remained accurate. We ran five trials for each set of oscillation amplitude and frequency

4.5.4.2 Varying inaccuracy of position sensing

To study the impact of uncertainty in the sensed position on the accuracy of beam stiffness estimation, we used an inaccurate sensed Y position, by assuming $Y = 0$ mm during traversal regardless of lateral oscillation. Thus, the larger the lateral oscillation amplitude, the less accurate the sensed Y position was. We ran simulations with an oscillation frequency of 6 Hz and varied the oscillation amplitude = 1, 2, and 3 mm. For each oscillation amplitude, we ran five trials.

4.5.4.2 Varying sensing time

Given our constant forward speed, it only took the robot 4.4 seconds to traverse a distance equal to its body length. Thus, the robot needs to react fast, i.e., the time cost of our method is important.

An inevitable time cost is sensing time, which is required to obtain contact force data to estimate stiffness. Therefore, we studied how beam stiffness estimation accuracy depends on the sensing time, to inform how long the robot needs to sense to obtain a reasonable estimate. We conducted tests using sensing time $T_s = 25, 50, 100$, and 200 ms,

with a data sampling rate of 40 Hz. These tests were collected at an oscillation amplitude of 1 mm and a frequency of 2 Hz, with five trials executed for each individual sensing time.

4.5.5 Potential energy barrier calculation to differentiate between stiff and flimsy beams

Cockroaches use different strategies when traversing flimsy and stiff beams (Othayoth et al., 2020). A critical stiffness helps categorize whether beams are stiff and should be traversed via the role mode (rolling through the gap between beams), or whether they are flimsy and should be traversed via the pitch mode (push over the beams).

To find the critical stiffness, we calculated the potential energy barrier corresponding to the pitch and roll modes. This allowed us to estimate which mode costs less mechanical energy for traversing stiff or flimsy beams. The potential energy of the system consisted of the gravitational potential energy of the robot and the elastic potential energy of the beams:

$$E(X,\alpha,\beta) = MgZ_{CoM}(\alpha,\beta) + \frac{1}{2}mgL\,(\cos\theta_1 + \cos\theta_2) + \frac{1}{2}k_1{\theta_1}^2 + \frac{1}{2}k_2{\theta_2}^2 \quad (33)$$

where $Z_{CoM}(\alpha,\beta)$ was the height of the center of mass from the ground, θ_1 and θ_2 were beam deflection angles, which were functions of α, β, and X. We varied X from −0.12 m to 0.12 m with an increment of ΔX = 0.002 m and α and β from −90° to 90° with an increment of $\Delta\alpha$ or $\Delta\beta$ = 2° to obtain a 3-D potential energy landscape over the entire (α, β, X) workspace during traversal (**Figure 29**A).

For simplicity, we started with the case where two beams had the same stiffness ($k_1 = k_2 = k_0$). For the pitch mode, we assumed that the potential energy reaches the maximum when the robot's bottom reaches the top of the beams where beams were

deflected most (**Figure 28**D, left). Thus, its potential energy barrier was $PE_{pitch}(\theta) = 2 \times \frac{1}{2} k_0 \theta^2$, which was the elastic potential energy of two beams. Because $\cos\theta_0 = \frac{H}{L}$, we had $PE_{pitch} = k_0 \, (\cos^{-1}\frac{H}{L})^2$. For the roll mode, the potential energy reached the maximum when the robot rolled until there was no contact in the entire traversal (**Figure 28**D, right). Thus, its potential energy barrier was $PE_{roll} = Mg \cdot \Delta h$, which was the increase of gravitational potential energy of the body.Using the principles of similar triangles, we obtained $\Delta h = h_c \left(1 - \frac{d}{2b}\right)$, which was the lifted height of center of mass of the body (**Figure 28**D, right).

When $PE_{pitch} - PE_{roll} = 0$, the threshold beam stiffness, $k_0 = \frac{Mg\, h_c\left(1-\frac{d}{2b}\right)}{(\cos^{-1}\frac{H}{L})^2}$. Because PE_{roll} did not depend on beam stiffness whereas PE_{pitch} was proportional to it, the barrier difference $PE_{pitch} - PE_{roll}$ monotonically increased with ko. Above this threshold, the roll mode was advantageous due to its lower energy barrier, whereas below this threshold, the pitch mode had a lower barrier.Substituting the parameters' values given in the simulation robot design (Sec.4.5.1),we obtained k_0 = 0.146 N·m/rad.

For simplicity, we selected a single representative stiffness value for each category: k_{low} = 0.01 N·m/rad and k_{high} = 0.2 N·m/rad as the stiffness of flimsy and stiff beams, respectively.

4.5.6 Force feedback strategy motion planning

For the force feedback strategy, we need to obtain the desired trajectory for traversing beams in *X*, roll, and pitch space according to beams stiffness. To determine this trajectory, a prediction of the mechanical energy cost associated with a given path

was necessary. A weighted directed graph (**Figure 29**B), composed of vertices and directed edges, was constructed based on the energy landscape (Sec. 4.5.5). Each vertex was connected through directed edges to its six closest neighbors, $(X \pm \Delta X, \alpha, \beta), (X, \alpha \pm \Delta\alpha, \beta), \text{and } (X, \alpha, \beta \pm \Delta\beta)$, where the increments were defined in Section 2.5. The directed edge had a value representing the mechanical energy cost. The total mechanical energy cost of a path in the network equaled the sum of the values attributed to its constituent directed edges. In a straightforward prediction and approximation, we defined the value of a directed edge leading to a state with greater potential energy to be positive, quantified by the increase in this potential energy. The value of a directed edge heading towards a state with lower potential energy was defined as zero, denoting no energy cost and recovery for such transitions (**Figure 29**B).

For each trajectory, we defined the initial state as the state when the robot started the active control (t_s), following a sensorimotor delay Δt from its first contact with the beams (t_c). The sensorimotor delay was $\Delta t = t_s - t_c$. The target state was defined as the state after traversal at $X = 0.1$ m with the horizontal body pose ($\alpha = \beta = 0°$). Given the directed weighed graph (**Figure 29**B), the A-star algorithm (Hart et al., 1968) was used to search for the path of the minimal cost between the initial and target states (**Figure 29**C), with the heuristic function being the potential energy difference of two states. The A-star algorithm operates by evaluating the cost to travel from one node to another, coupled with a heuristic that estimates the cost to reach the goal from a given node. We took this path as the planned path.

4.5.7 Force feedback strategy motion control

For the force feedback strategy, motion control was required to track the planned trajectory. We controlled the roll and pitch angle while maintaining a forward speed of v_X

= 0.05 m/s. This constant forward speed setting simplified the control process and was retained from the prior design (Othayoth et al., 2020). Based on the position error, we used a model-based feedback control to obtain the control input at every 0.002 s:

$$\vec{u} = F_{ext}(\vec{q}) - K_p(\vec{q} - \overrightarrow{q_d}) \tag{34}$$

where $\vec{q} = (X, \alpha, \beta)$ was the current state and $\overrightarrow{q_d} = (X_d, \alpha_d, \beta_d)$ was the desired state. K_p was positive feedback gain (we chose 0.1). $\vec{u} = (\tau_1, \tau_2, F_X)$ was the control input (**Figure 28**B). τ_1, τ_2 are pitch and roll torques. F_X is the force along X direction. $F_{ext}(\vec{q})$ was the external force calculated from the contact force model (Sec. 4.5.2), including contact forces with beams and the gravitational force. With the control input $\vec{u}$, the current state was controlled to approach the desired state at every time step.

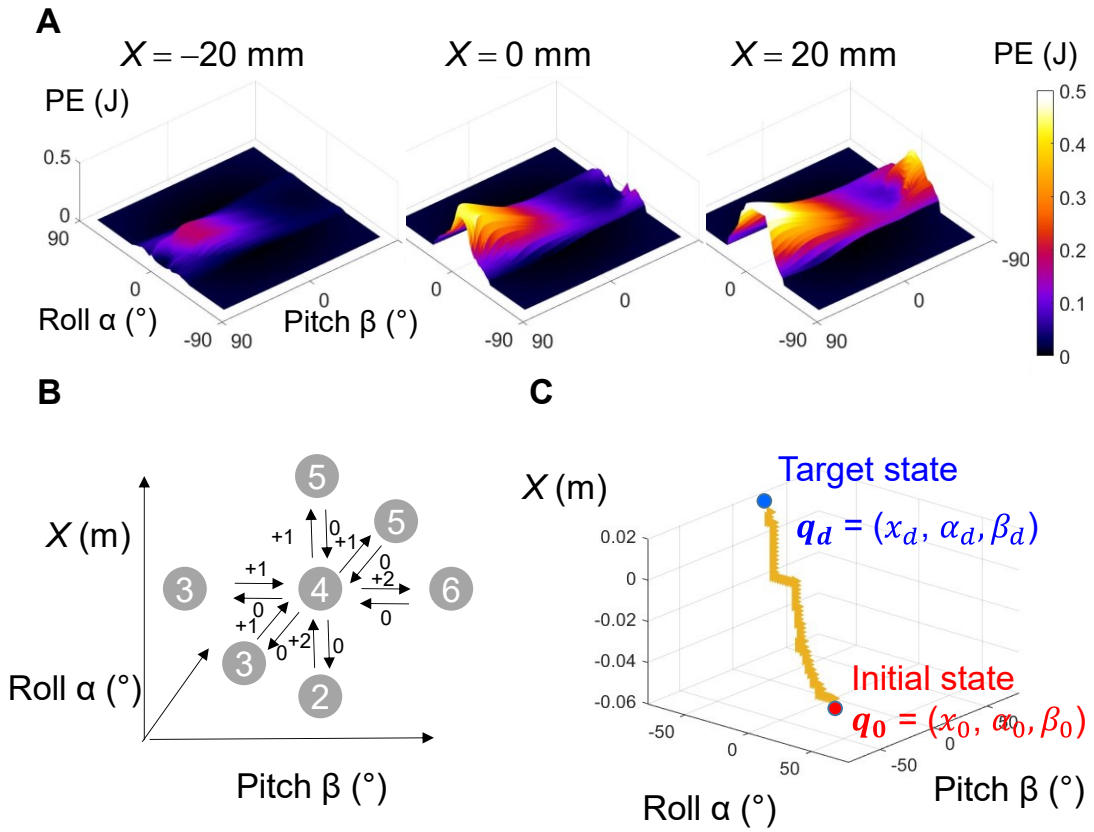

Figure 29. Motion planning. (A) 3-D potential energy landscape of the robot-beam interaction system. (B) Schematic of the weighted directed graph based on potential energy landscape. Circles are states. Values in circles show the potential energy (in Joules) at each state, while values on directed edges show the predicted mechanical energy cost of the movement along the edge. (C) The path from the initial to the target state in the weighted directed graph, with the minimal predicted mechanical energy cost.

4.5.8 Motor work calculation to compare across strategies

To compare the mechanical energy cost of different strategies, we calculated the work done by actuators in the entire traversal using the below function:

$$E_{cost} = \sum_{i=1}^{m}[(F_X v_X)^+ + (\tau_1 \omega_1)^+ + (\tau_2 \omega_2)^+]\, dt \quad (35)$$

where *m* was the number of control steps in the entire traversal time, $dt = 0.002$ s was the control time step (Sec. 4.5.7). $(F_X v_X)$ was the power of the force F_X. $(\tau_1 \omega_1)$ and $(\tau_2 \omega_2)$ were the powers of two torques (τ_1, τ_2). The symbol "+" meant $(f)^+ = \max\{f, 0\}$, as we assumed that actuators would not recycle energy.

4.5.9 Varying sensorimotor delay for force feedback strategy

Sensorimotor delay is inevitable in both animals and robots. To study the impact of sensorimotor delay on traversal performance of our force feedback strategy, we conducted simulations with three different sensorimotor delays $\Delta t = 320$, 480, and 640 ms and evaluated its impact on mechanical energy cost from actuators (Eqn. 35). Sensorimotor delay was defined as the time interval between the instant of the first contact with beams and the start of actuators, incorporating the previously mentioned sensing time T_s. For simplicity, and to better show the impact of sensorimotor delay, the initial body pitch angle started with zero angle and the actuators did not generate body oscillations.

Because the simulation was deterministic without randomness, we ran one trial for each sensorimotor delay.

4.6 Results

We found that each of the three strategies without force sensing offers distinct advantages and drawbacks when traversing flimsy and stiff beams (Sec. 4.6.1). Our force feedback strategy had the combined strengths of these methods, facilitating enhanced beam traversal of both flimsy and stiff beams (Sec. 4.6.3). Beam stiff estimation was robust against random oscillations (Sec. 4.6.2). Additionally, the mechanical energy cost during traversal increased with sensorimotor delay for the force feedback strategy (Sec. 4.6.4).

4.6.1 Traversing flimsy and stiff beams without force sensing

4.6.1.1 Feedforward pushing without force/torque limits

When encountering flimsy beams, the robot pushed over beams with a small body pitch angle (< 4°) (**Figure 30**A, bottom; Movie 5) and small contact force (< 0.13 N). Its energy cost over the entire traversal was 14.8 mJ. When encountering stiff beams, the robot was pushed by the beams to oscillate up and down over a wide range of angles ([–37°, 38°]) (**Figure 30**A, top; Movie 5), and the maximal resistive force from the beams reached 1.5 N. If the robot were freely moving on the ground and experienced such large pitch oscillations, it could easily lose stability and flip over. In addition, the robot's mechanical energy cost over the entire traversal was 185.2 mJ, much larger than during flimsy beam traversal.

4.6.1.2 Feedforward pushing with force/torque limits

When encountering flimsy beams, the robot behaved the same as it did with

unlimited force because the resistive force was smaller than the force limit (**Figure 30**B, bottom; Movie 5). However, when encountering stiff beams, the robot was stuck in front of the beams (**Figure 30**B, top; Movie 5). The body pitched up substantially in this process, and it then oscillated up and down in pitch from intermittent contact with beams.

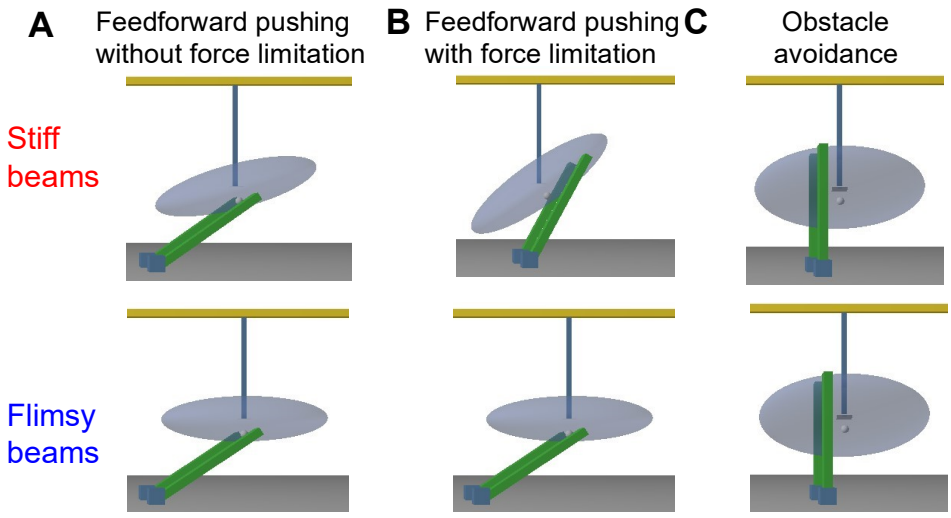

Figure 30. Representative snapshots of simulation robot traversing stiff and flimsy beams using different strategies. (A) Feedforward pushing strategy with unlimited propulsive force. The robot traversed both stiff and flimsy beams. (B) Feedforward pushing strategy with limited propulsive force. The robot was stuck in front of stiff beams but pushed over flimsy beams. (C) Obstacle avoidance strategy with force/torque limits. The robot successfully traversed both stiff and flimsy beams without contact.

4.6.1.3 Avoiding obstacles

Because beams with different stiffness had the same environmental geometry, the robot moved in the exact same way when traversing flimsy and stiff beams (**Figure 30**C; Movie 5). Its energy cost was 35.8 mJ. The obstacle avoidance strategy did save much energy compared to the feedforward pushing strategy (185.2 mJ) when the obstacle was stiff. However, the obstacle avoidance strategy was not the best option for the flimsy

beams. Its energy cost was higher than the feedforward pushing strategy (14.8 mJ), and the large body rolling required to avoid the beams could make it challenging to maintain stability.

4.6.2 Estimating beam properties in simulation

We estimated the stiffness of the beams using the contact physics model and studied the robustness of the estimation accuracy against random body oscillations, inaccuracy position sensing, and the varying sensing time.

4.6.2.1 Estimation of beam stiffness under random body oscillations

Our estimation results for two beams' stiffness ($\widehat{k_1}$, $\widehat{k_2}$) across varying oscillation frequencies indicated that the estimation accuracy was not notably affected by the oscillation frequencies (**Table 2**) or amplitudes (**Table 3**). Although the oscillation caused more collisions and intermittent body-beam contact, our approach still obtained an accurate estimation of stiffness (relative error e_k < 5% in 90% trials), which was a prerequisite for motion planning and control.

Table 2. **Error in beam stiffness estimation (in N·m/rad) for varying oscillation frequencies (five trials each).**

Frequency (Hz)	2	4	6
$\widehat{k_1}$ (e_{k1})	0.484 (3.3%)	0.475 (5.1%)	0.477 (4.7%)
$\widehat{k_2}$ (e_{k2})	0.473 (5.4%)	0.479 (4.3%)	0.475 (4.9%)

Table 3. **Error in beam stiffness estimation (in N·m/rad) for varying oscillation amplitudes (five trials each).**

Amplitude (mm)	1	2	3

$\widehat{k_1}$ (e_{k1})	0.484 (3.3%)	0.482 (3.6%)	0.483 (3.3%)
$\widehat{k_2}$ (e_{k2})	0.473 (5.4%)	0.477 (4.6%)	0.477 (4.6%)

4.6.2.2 Estimation of beam stiffness with position sensing error

In the above estimation, although oscillations and randomness were introduced, the robot still had accurate measurements of its position relative to the obstacles. However, in practice, the robot's position sensing may not be accurate because of its intense oscillations.

Through calculating the mean of relative errors ($\frac{e_{k1}+e_{k2}}{2}$)) of beams' stiffness among trials, we discovered that, generally, an increase in oscillation amplitude led to an increase in the relative error of estimation (**Figure 31**) as well as an increase in the variation of estimation among different trials. Despite these, the estimation accuracy was still acceptable (relative error e_k < 15%), which was sufficient for differentiating stiff and flimsy beams. Thus, our estimation was robust against errors in position sensing.

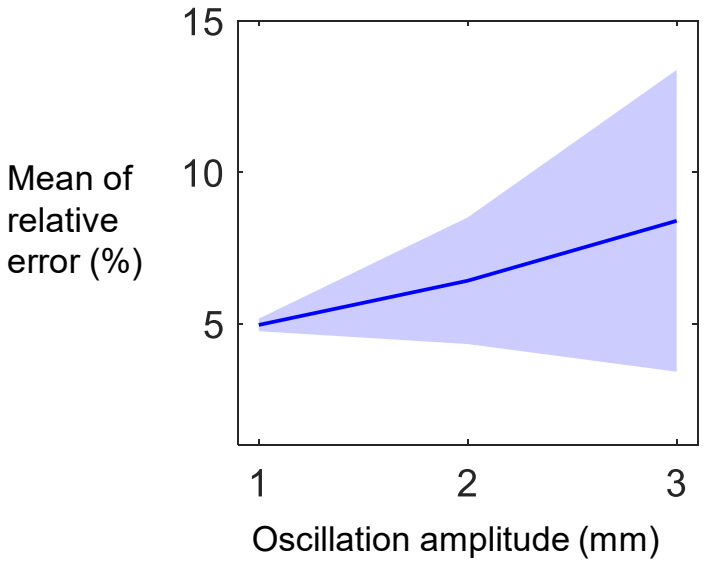

Figure 31. Mean of relative estimation error ($\frac{e_{k1}+e_{k2}}{2}$) as a function of oscillation amplitude. Five trials were performed at each oscillation amplitude. The blue curve represents the mean, and the shaded area indicates the standard deviation (± s. d.).

4.6.2.3 Effect of sensing time on beam stiffness estimation

We varied sensing time T_s to study its impact on estimation of beams stiffness. A longer sensing time means more data can be used in model fitting. As expected, a longer sensing time resulted in a decrease in the combined relative estimation error (Table 3, $e_{k1} + e_{k2}$). This sum represents the overall error. However, for a sufficiently long sensing time (≥ 50 ms), further increasing sensing time (adding more sensed data) did not improve estimation accuracy substantially, because the randomness and modeling error became dominant (**Table 4**).

Table 4. **Error in beam stiffness estimation for different sensing times (five trials each, $f = 2$ Hz, $A_l = 1$ mm).**

T_s	25 ms	50 ms	100 ms	200 ms
$\widehat{k_1}(e_{k1})$	0.531 (6.2%)	0.513 (2.6%)	0.516 (3.2%)	0.522 (4.4%)
$\widehat{k_2}(e_{k2})$	0.383 (23.4%)	0.473 (5.4%)	0.491 (1.8%)	0.488 (3.2%)

4.6.3 Traversing beams with force feedback

The simulation results showed that the force feedback strategy worked well, and the traversal was successful for both flimsy and stiff beams (**Figure 32**; Movie 5). The mechanical energy cost to traverse flimsy beams was 15.0 mJ, which was almost the same as that of the feedforward pushing strategy (14.8 mJ; Sec. 4.6.1.1). The slight increase in energy might be attributed to its cost in pitch control to track desired pitch angle. The mechanical energy cost to traverse stiff beams was 17.4 mJ, which was much smaller

than that of the feedforward pushing strategy (185.2 mJ; Sec. 4.6.1.1). It also consumed less mechanical energy than the obstacle avoidance strategy (35.8 mJ; Sec. 4.6.1.3), because the robot could lean against the beams between the gap and the interaction forces/torques with beams helped the robot roll.

Table 5. **Mechanical energy cost of different strategies for traversing stiff and flimsy beams (one trial each)**.

Strategy	Pushing without force limit	Pushing with force limit	Obstacle avoidance	Force-feedback control
Stiff beams	185.2 mJ	Failure	35.8 mJ	17.4 mJ
Flimsy beams	14.8 mJ	14.8 mJ	35.8 mJ	15.0 mJ

In comparison to strategies without force sensing, our force feedback strategy had the advantage of being able to adaptively traverse beams in response to beam properties (**Table 5**). Without force sensing, it was impossible to differentiate between beam types, leading to the use the same strategy for both stiff and flimsy beams. While the feedforward pushing strategy was effective for flimsy beams, it was challenged by stiff beams, leading to significant energy costs if the force/torque limits were not reached, or causing the robot to become stuck upon reaching that limits. On the other hand, the obstacle avoidance strategy, although working well for stiff beams, was not optimal for flimsy ones due to high energy costs. By incorporating force sensing, our force feedback strategy required minimal energy cost during the traversal of both beam types and reduced the risk of the robot getting stuck. Unlike the feedforward pushing strategy, which failed to traverse stiff beams with force/torque limits, our force feedback strategy successfully traversed them even with force/torque limits.

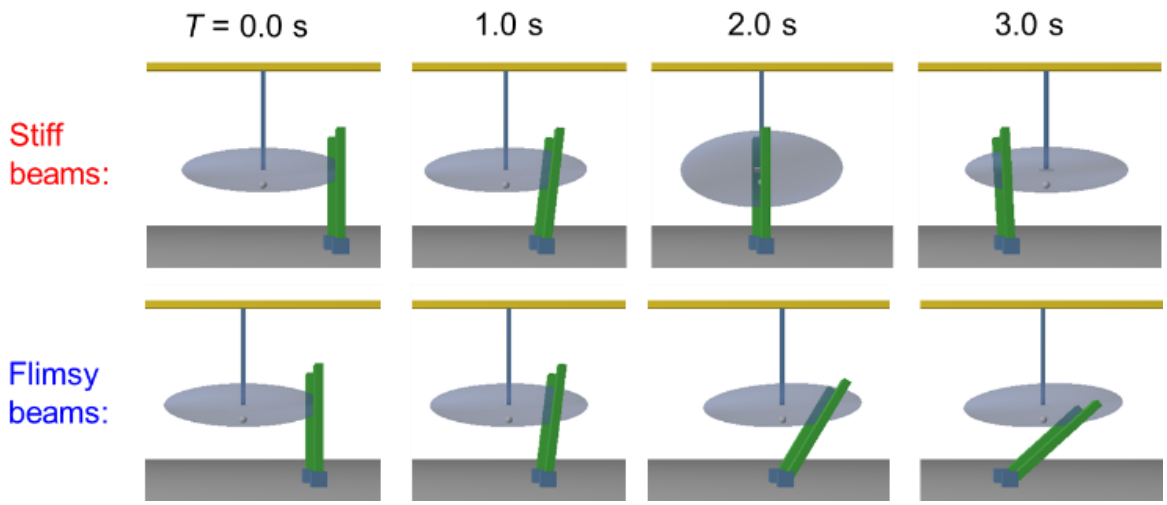

Figure 32. Snapshots of the robot traversing stiff and flimsy beams using force feedback.

4.6.4 Traversal performance with different sensorimotor delay

The longer the sensorimotor delay was, the more the robot had pitched up when it started active control (**Figure 33**A). Despite this, the robot traversed in all trials (Movie 5). We found that the longer the sensorimotor delay, the more energy cost from forwarding and rotation (both roll and pitch) actuators (**Figure 33**B). Thus, the faster the robot could estimate the properties of obstacles and respond after encountering obstacles, the more energy it would save.

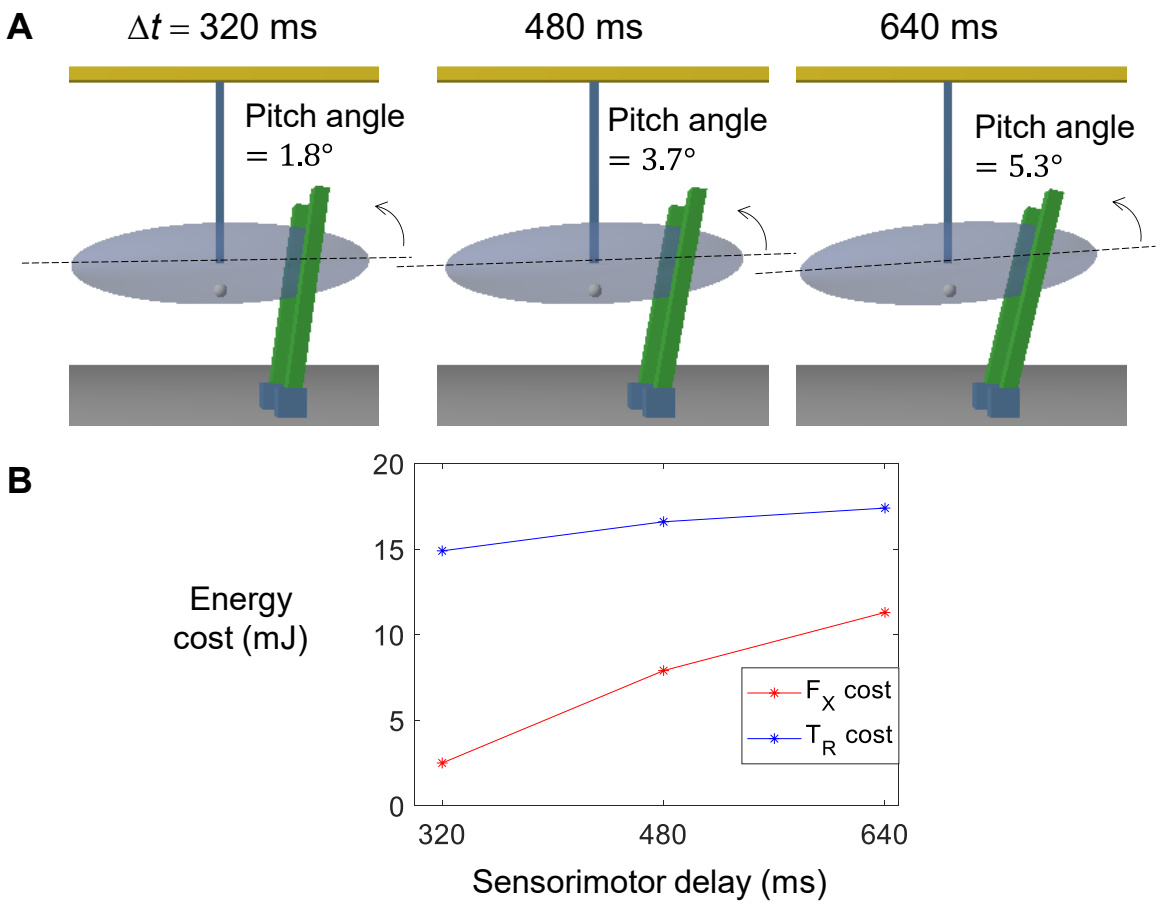

Figure 33. Influence of sensorimotor delay. (A) Snapshots showing system configuration when the control started after different sensorimotor delays. (B) Mechanical energy cost from forwarding and rotation (both roll and pitch) actuators (F_X and T_R cost) as a function of sensorimotor delay (one trial each).

4.7 Discussion

Our modeling and simulation results showed that environmental force sensing can help robots determine previously unknown beam properties and inform planning and control accordingly to traverse cluttered obstacles by effectively using physical interaction. We compared our new force feedback traversal strategy with commonly used traversal

strategies, feedforward pushing and obstacle avoidance, in simulation. The force feedback strategy based on force sensing helped the robot save mechanical energy cost during beam traversal, prevented it from becoming stuck in front of beams, and could prevent it from flipping over.

Our modeling study demonstrated the usefulness of body contact force sensing for estimating terrain properties and allowing robots to traverse larger, cluttered obstacles with enhanced performance. This novel capability to use the body to sense environmental contact forces to infer environmental physics and guide motion control will be directly useful for RHex-class robots (Chou et al., 2012; Ilhan et al., 2018) moving in complex 3-D terrain, and it will also catalyze more diverse robot platforms to sense and use body-obstacle physical interaction (in addition to sensing leg-ground interaction (Arena et al., 2015; Bhattacharya et al., 2020; Kimura et al., 2001; Shill et al., 2015; Walas, 2013; Wu et al., 2016)) to better move in the real world. Our lab is currently developing a robophysical model of the body-beam interaction system, instrumented with custom internal 3-D force sensors and distributed external contact sensors. Building on the modeling insight here, we will use it to further study the principles of mechanical sensory feedback control and demonstrate advancement in a real robotic system.

In addition to robotics, our work also has implications for biology. The discoid cockroach (and other animals that use body-environment physical interaction to traverse cluttered large obstacles) uses load-sensitive mechanoreceptors distributed throughout their body (Ayali et al., 2015) to sense contact. Our modeling suggested that this sensory information may help them use locomotor modes that are less costly to traverse. Such mechanical sensory feedback can complement eyes (Harley et al., 2009) and antennae (Okada and Toh, 2006) that sense the visual/geometric information of the environment and help them better traversing cluttered obstacles with reduced energy cost.

Our motion planning has limitations that require further examination. We neglected the effect of body inertia and assumed constant forward speed in motion planning. These approximations and assumptions simplify the system modeling and analysis, but they may compromise traversal performance. We attempted to apply optimal control while considering body inertia and allowing forward speed to vary. However, it was challenging to find the global minimum because of the non-smooth nature of contact force (for example, abrupt changes in contact force during the transition from roll to pitch mode) and intermittent collisions between the robot body and beams.

While this work simplifies obstacles by modeling them as rigid plates with torsion springs, our proposed approach should extend to a variety of other obstacles. The only prerequisite for our method is the availability of a model that establishes the relationship between contact force and physical properties of obstacles. If the robot encountered a new obstacle, we could develop a physics model tailored to it. For example, when dealing with movable rigid obstacles, considerations such as resistive force and displacement in all directions would become crucial factors in the model and could be monitored through continuous force sensing. Such an extension will be useful in search and rescue operations amidst earthquake rubble, where obstacle avoidance may not be feasible and obstacles vary in stability, rigidity, and mobility. By employing force sensing, we can formulate a traversal strategy to decide whether to lean on, avoid, or push obstacles away.

We focused on using the predictive physics model to estimate unknown obstacle physical properties. Future work should also expand its use in robot control. For example, feedback control (Eqn. 34) requires real-time reading of the robot's states and external forces. However, because there is a time delay in sensors, the actual control input is always calculated using the state and external forces from the previous moment. Therefore, when velocities or accelerations are large, the control may not be timely and

may lead to unexpected collisions. In this case, the physics model can be used to predict the evolution of the state and external forces and enable more effective and timely control of robots.

Chapter 5

Conclusions

5.1 General remarks

In this dissertation research, we employed physics models and simulations to study how a cockroach or a cockroach-inspired robot deals with the strenuous conditions in self-righting and beam traversal. This research contributes to the fundamental principles necessary for understanding and controlling the physical interactions involved in locomotor mode transitions. Both locomotion, ground self-righting and beam traversal, require destabilizing the stable limit cycle to switch to another locomotor mode. From the potential energy landscape framework, this process involves crossing an energy barrier and escaping from an energy basin. Our findings indicate that when energy from wing opening and leg flailing is insufficient, wing-leg coordination, measured by the phase between wing and leg oscillations, had a crucial impact on self-righting outcome. With randomness, the system explored phases thoroughly and had a better chance of encountering good phases to self-right. In addition, our template reveals how wing-leg coordination influences mechanical energy dynamics, including the generation of energy through wing pushing and leg flailing and energy dissipation during wing-ground collisions. These insights offer valuable guidance for robot design and control. In cluttered beam traversal scenarios, sensor-less robots can move through, but it is a strenuous process with risks of getting stuck or flipping over. Cockroaches, however, seem to excel, possibly because they can sense forces during interactions. Inspired by this, our simulations

showed that environmental force sensing helped robots traverse large, cluttered obstacles better. We developed a sensory feedback strategy based on a physics model. The simulations proved that this strategy works better than the usual methods like obstacle avoidance or feedforward pushing.

5.2 Specific accomplishments

5.2.1 Randomness assists in avoiding being trapped in an undesired metastable state

Although randomness is typically considered as a nuisance, it can be useful for locomotion (Bartumeus, 2009; Moore et al., 2017; Reynolds and Rhodes, 2009; Sutantyo et al., 2010). Its inherent unpredictability can be strategically employed to facilitate an escape from undesired states.

Motivated by the considerable randomness observed in the neural control mechanisms of insects for self-righting, as opposed to the more predictable patterns seen in walking and running, this study found integrating randomness into the self-righting motion enhances the coordination between wings and legs, leading to a higher success rate. The increased randomness in motor control patterns may be an adaptation, by probabilistically increasing the likelihood of success during strenuous self-righting maneuvers.

Our work complemented earlier research which focused on mitigating the negative impact of randomness to stabilize locomotion around the limit cycle. As our results demonstrated, randomness in motion can be advantageous, assisting in escaping being trapped in an undesired metastable state. This insight may have broader implications. For instance, when traversing complex terrain with large obstacles, both animals and robots

might frequently require transitioning across distinct locomotor modes, each representing a metastable state.

5.2.2 Wing-leg coordination enhances mechanical energy accumulation in self-righting

The template model successfully captures the basic features of motion by using simpler, lower-dimensional models to represent the key elements of complex systems. This method helps in better understanding their mechanisms and control (Full and Koditschek, 1999). To uncover the fundamental principles of self-righting with randomness and to expand its application, we delved deeper into the phase between wing and leg oscillations and its significant impact on self-righting by creating a dynamic model template.

Few robots have been designed to utilize multiple appendages to self-right (Saranli et al., 2004). In comparison, animals have developed complex strategies that dynamically utilize various body parts for self-righting (for a review, see (Li et al., 2019a)). Our template is innovative because it focuses on the active coordination between different appendage types. Despite the recognized importance of appendage coordination in locomotion involving multiple appendages, the systematic study of its impact on movement has been limited in previous models. In walking models, the coordination between arms and legs has been examined, yet in these studies, the arms were passive (lacking actuation) and the aspect of active coordination between them was not explored (Collins et al., 2009). The multi-legged ground self-righting model efficiently manages the torques of three synchronized pairs of legs to enhance thrust and optimize the recovery of kinetic energy from impacts (Saranli et al., 2004). However, this model focuses on coordination among appendages of the same type, specifically legs.

This template helped us quantify the potential energy barrier the body must surpass to self-right, the mechanical energy from wing pushing and leg flailing, and energy loss from wing-ground collisions. It became clear that wing-leg coordination, or phase, strongly influences the self-righting outcome by changing mechanical energy budget. With good coordination, the system accumulates more mechanical energy, overcoming potential energy barriers and achieving a more successful self-righting.

5.2.3 Model-driven robotic design and control for self-righting

Beyond a mechanistic insight of this complex hybrid dynamical system, we demonstrated practical advantages of the template. It enabled a model-based feedback control strategy that enhanced self-righting performance. Further, we employed the template to study the influence of system parameters on both cumulative mechanical energy and potential energy barriers, providing valuable insights for robotic design.

5.2.4 Body force sensing provides insights into physical properties of obstacles and enhances cluttered obstacle traversal

Traversing large, cluttered obstacles is a challenging task (Guizzo and Ackerman, 2015b; Guizzo and Ackerman, 2015a; Li and Lewis, 2023), and understanding how to utilize and control physical interactions with the environment (known as environmental affordance (Gibson, 1979; Roberts et al., 2020)) is crucial to effective locomotion. Our modeling highlighted the significance of body contact force sensing in physical interaction by estimating physical properties of obstacles, enhancing a robot's ability to traverse cluttered, large obstacles. The force feedback control destabilizes the stable limit-cycle running mode and facilitates transitioning to the more favorable, less strenuous rolling mode based on sensory feedback. Environmental force sensing assists in shifting

between different locomotor modes to traverse large beam obstacles by crossing the energy barrier, preventing the system from getting stuck.

Through simulation, we discovered that environmental force sensing aids the robot in identifying unknown beam stiffness, enabling it to effectively interact with and traverse obstacles. In comparing our force feedback method with prevalent strategies like feedforward pushing and obstacle avoidance, simulation results showed that our approach saved mechanical energy, reduced the risk of robots getting trapped or flipping over during traversal. Moreover, recent developments (Wang and Li, 2023) in our lab include a robophysical model equipped with custom 3-axis force sensors and surface contact sensors. This model was designed to measure forces during interactions with large obstacles. Unlike my research, where the obstacles were predetermined as elastic beams with some unknown parameters like stiffness, the new findings suggest that the measured forces effectively represent gradients in the potential energy landscape for more general obstacles, potentially allowing for the reconstruction of this landscape to facilitate traversal.

5.3 Future directions

5.3.1 Animal experiments to validate randomness as an adaptive response in strenuous self-righting

Our research indicates that randomness could be an adaptive response to strenuous ground self-righting. Animal experiments could offer further validation for this. An interesting study to explore, based on our findings, is whether energetic animals exhibit less randomness in their movements compared to fatigued animals. But it poses an

intriguing challenge to distinguish between uncontrolled randomness in animal self-righting and a deliberate introduction of randomness as a behavioral adaptation.

5.3.2 Advancing models for more complex and practical self-righting

The current model serves as a basic template, intentionally designed for a foundational understanding of the mechanism. Incorporating detailed morphological and actuation attributes would refine models that are grounded in this template (Full and Koditschek, 1999; Lee et al., 2008). For example, to explore more complex and practical self-righting strategies, we can consider the role of the bending abdomen in self-righting (Li et al., 2019b). We can use the advanced model with the abdomen to study how wings, legs, and abdomen coordinate together.

5.3.3 Demonstrating the efficacy of environmental force sensing feedback control in diverse cluttered obstacles

This study represents the obstacle as rigid plates combined with torsion springs. While we believe our approach can apply to a range of different obstacles, further research is necessary for validation. For instance, when confronted with movable rigid obstacles, the contact force could provide insights into the friction coefficient, inertia, and mass. In a household setting, a vacuum robot might use force sensing to discern movable objects like plastic bags or boxes from immovable ones like tables or to determine if a door can be pushed open. In search and rescue missions after earthquakes, avoiding obstacles is not always possible. By employing force sensing, we can formulate a traversal strategy to decide whether to lean on, climb up, or push obstacles away.

5.3.4 Enhancing locomotion capabilities on complex terrains through optimal control

Legged locomotion requires the coordinated control of body joints, a challenging task due to the typically high degrees of freedom involved. Maintaining stable and energy-efficient motion in such systems is complex. To address this, many studies have applied optimal control methods, defining cost functions to guide the process. This approach has achieved success in bipedal, quadrupedal, and hexapedal robots on flat ground (Bai et al., 2017; Farshidian et al., 2017; Mombaur and Truong, 2010; Mombaur et al., 2010). Additionally, there is a well-established focus on utilizing optimal control to manage traversal across more complex terrains (Byl and Tedrake, 2008; Gangapurwala et al., 2022; Wu and Popović, 2010; Zucker et al., 2011).

In our own research, as detailed in Chapter 4, we have explored the application of optimal control in beam traversal. This task proved to be particularly challenging due to the difficulty in finding the global minimum, largely because of the non-smooth nature of contact forces, such as sudden changes during transitions from rolling to pitching modes, and the intermittent collisions between the robot and the beams. With further simplifications or the adoption of more advanced optimal control strategies, this approach could be effectively applied to traversing beam-like obstacles. Moreover, it holds potential for further enhancing self-righting performance.

Appendices

List of supplementary movies

The movies are uploaded with this dissertation and also available through YouTube links.

Movie 1. Cockroach' self-righting using wing opening and leg. Link: https://youtu.be/QmccVocX1KU.

Movie 2. Comparison between self-righting of the physical robot and simulation. Link: https://youtu.be/n3xUmW_8pSA.

Movie 3. Comparison of self-righting of the simulation robot with and without randomness in phase. Link: https://youtu.be/69sekO0UXQ0

Movie 4. Coordinated appendages accumulate more energy to self-right on the ground. Link: https://youtu.be/aWGojRufNbc

Movie 5. Environmental force sensing helps robots traverse cluttered large obstacles. Link: https://youtu.be/3dvaISmcJa0

Unpublished results

Below are some of the preliminary results that were not included in the previous chapters or other publications but can be potentially useful in future research or inspire new ideas that contribute to science and technology.

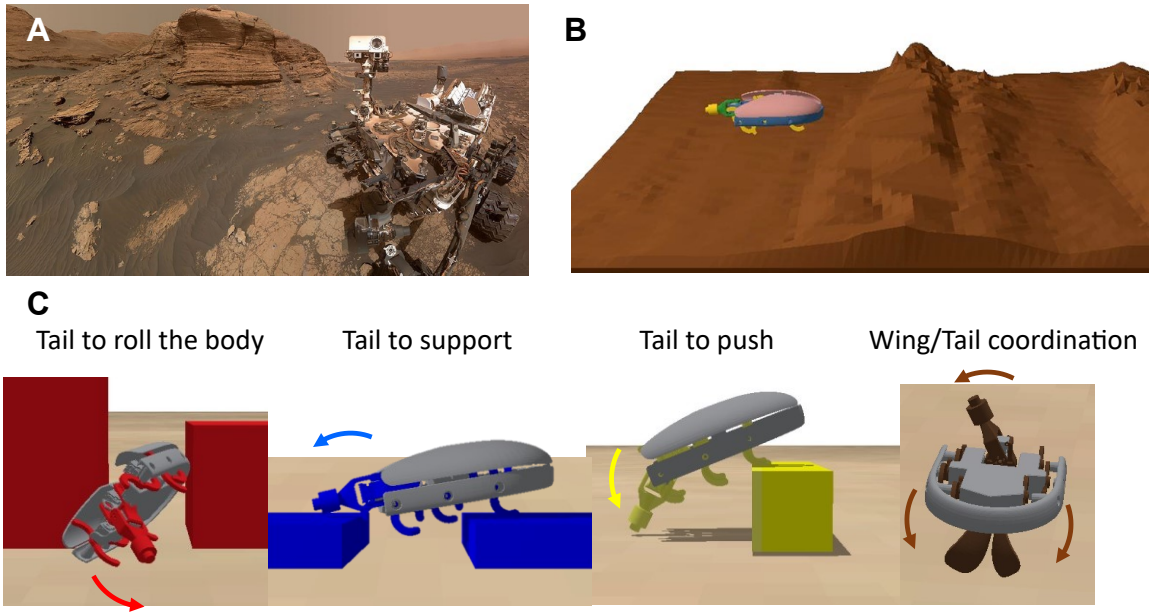

Figure 34 Simulation of multi-functional robot (Omni-Roach) on complex terrain. (A) The Curiosity Rover navigating Martian terrain. Due to its mobility constraints, it operates within a confined workspace. (B) A simulation demonstrated Omni-Roach traversing a Martian landscape, reconstructed using data from the Curiosity Rover. (C) Simulations demonstrate the Omni-Roach traversing multiple barriers by coordinating its appendages (wings, legs, tail) using feedback control.

Reference

Bibliography

Agarwal, S., Karsai, A., Goldman, D. I. and Kamrin, K. (2021). Surprising simplicity in the modeling of dynamic granular intrusion. *Sci. Adv.* **7**,.

Aguilar, J. and Goldman, D. I. (2016). Robophysical study of jumping dynamics on granular media. *Nat. Phys.* **12**, 278–283.

Aguilar, J., Zhang, T., Qian, F., Kingsbury, M., McInroe, B., Mazouchova, N., Li, C., Maladen, R., Gong, C., Travers, M., et al. (2016). A review on locomotion robophysics: The study of movement at the intersection of robotics, soft matter and dynamical systems. *Reports Prog. Phys.* **79**, 110001.

Alber, M., Buganza Tepole, A., Cannon, W. R., De, S., Dura-Bernal, S., Garikipati, K., Karniadakis, G., Lytton, W. W., Perdikaris, P., Petzold, L., et al. (2019). Integrating machine learning and multiscale modeling—perspectives, challenges, and opportunities in the biological, biomedical, and behavioral sciences. *npj Digit. Med.* **2**,.

Altendorfer, R., Moore, N., Komsuoglu, H., Buehler, M., Brown, H. B., Mcmordie, D., Saranli, U., Full, R. and Koditschek, D. E. (2001). RHex: A biologically inspired hexapod runner. *Auton. Robots* **11**, 207–213.

Arena, P., Furia, P., Patané, L. and Pollino, M. (2015). Fly-inspired sensory feedback in a reaction-diffusion neural system for locomotion control in a hexapod robot. *Proc. Int. Jt. Conf. Neural Networks* **2015-Septe**, 1–8.

Ayali, A., Couzin-Fuchs, E., David, I., Gal, O., Holmes, P. and Knebel, D. (2015). Sensory feedback in cockroach locomotion: current knowledge and open questions. *J. Comp. Physiol. A Neuroethol. Sensory, Neural, Behav. Physiol.* **201**, 841–850.

Bai, L., Ma, L., Dong, Z. and Ge, X. (2017). Kinematics , Dynamics , and Optimal Control of Pneumatic Hexapod Robot. *Math. Probl. Eng.* **2017**,.

Bangs Laboratories (2015). Material Properties of Polystyrene and Poly(methyl methacrylate) (PMMA) Microspheres. 1–2.

Bartumeus, F. (2009). Behavioral intermittence, Lévy patterns, and randomness in animal movement. *Oikos* **118**, 488–494.

Bekker, M. G. (1960). *Off the road locomotion*. University of Michigan Press.

Bénichou, O., Coppey, M., Moreau, M., Suet, P. H. and Voituriez, R. (2005). A stochastic theory for the intermittent behaviour of foraging animals. *Phys. A Stat. Mech. its Appl.* **356**, 151–156.

Bergman, C. M., Schaefer, J. A. and Luttich, S. N. (2000). Caribou movement as a correlated random walk. *Oecologia* **123**, 364–374.

Bergstra, J. and Bengio, Y. (2012). Random search for hyper-parameter optimization. *J. Mach. Learn. Res.* **13**, 281–305.

Bhattacharya, S., Luo, A., Dutta, S., Miura-Mattausch, M. and Mattausch, H. J. (2020). Force-sensor-based surface recognition with surface-property-dependent walking-speed adjustment of humanoid robot. *IEEE Access* **8**, 169640–169651.

Bledt, G., Powell, M. J., Katz, B., Di Carlo, J., Wensing, P. M. and Kim, S. (2018). MIT Cheetah 3: Design and Control of a Robust, Dynamic Quadruped Robot. *IEEE Int. Conf. Intell. Robot. Syst.* 2245–2252.

Blickhan, R. (1989). The spring-mass model for running and hopping. *J. Biomech.* 1217–1227.

Blickhan, R. and Full, R. J. (1993). Similarity in multilegged locomotion: Bouncing like a monopode. *J. Comp. Physiol. A* **173**, 509–517.

Borenstein, J. and Koren, Y. (1991). The vector field histogram-fast obstacle avoidance for mobile robots - Robotics and Automation, IEEE Transactions on. *IEEE Trans. Robot.* **7**, 278–288.

Bovet, P. and Benhamou, S. (1988). Spatial analysis of animals' movements using a correlated random walk model. *J. Theor. Biol.* **131**, 419–433.

Byl, K. and Tedrake, R. (2008). Approximate Optimal Control of the Compass Gait on Rough Terrain. *IEEE Int. Conf. Robot. Autom.* 1258–1263.

Byl, K. and Tedrake, R. (2009). Metastable walking machines. *Int. J. Rob. Res.* **28**, 1040–1064.

Caines, P. E. (2002). An introduction to hybrid dynamical systems. *Automatica* **38**, 566–567.

Camhi, J. M. (1977). Behavioral switching in cockroaches: transformations of tactile reflexes during righting behavior. *J. Comp. Physiol.* ■ *A* **113**, 283–301.

Casarez, C. S. and Fearing, R. S. (2017). Dynamic terrestrial self-righting with a minimal tail. *IEEE Int. Conf. Intell. Robot. Syst.* **2017-Septe**, 314–321.

Cavagna, G. A., Heglund, N. C. and Taylor, C. R. (1977). Mechanical work in terrestrial locomotion: two basic mechanisms for minimizing energy expenditure. *Am. J. Physiol. - Regul. Integr. Comp. Physiol.* **2**, R243–R261.

Choi, S., Ji, G., Park, J., Kim, H., Mun, J., Lee, J. H. and Hwangbo, J. (2023). Learning quadrupedal locomotion on deformable terrain. *Sci. Robot.* **8**, 1–14.

Chou, Y. C., Yu, W. S., Huang, K. J. and Lin, P. C. (2012). Bio-inspired step-climbing in a hexapod robot. *Bioinspiration and Biomimetics* **7**,.

Chou, Y. C., Huang, K. J., Yu, W. S. and Lin, P. C. (2015). Model-based development of leaping in a hexapod robot. *IEEE Trans. Robot.* **31**, 40–54.

Clifton, G., Stark, A. Y., Li, C. and Gravish, N. (2023). The bumpy road ahead: the role of substrate roughness on animal walking and a proposed comparative metric. *J. Exp. Biol.* **226**,.

Collins, S. H., Adamczyk, P. G. and Kuo, A. D. (2009). Dynamic arm swinging in human walking. *Proc. R. Soc. B Biol. Sci.* **276**, 3679–3688.

Coros, S., Jones, B. and Reveret, L. (2011). Locomotion Skills for Simulated Quadrupeds. **1**, 1–12.

Delcomyn, F. (1987). Motor activity during searching and walking movements of cockroach legs. *J. Exp. Biol.* **133**, 111–120.

Ding, Y., Sharpe, S. S., Masse, A. and Goldman, D. I. (2012). Mechanics of Undulatory Swimming in a Frictional Fluid. *PLoS Comput. Biol.* **8**, e1002810.

Domokos, G. and Várkonyi, P. L. (2008). Geometry and self-righting of turtles. *Proc. R. Soc. B Biol. Sci.* **275**, 11–17.

Elfes, A. (1989). Using occupancy grids for mobile robot perception and navigation. *Computer (Long. Beach. Calif).* **22**, 46–57.

Ellery, A. (2015). *Planetary rovers: robotic exploration of the solar system*. Springer.

Faisal, A. A., Selen, L. P. J. and Wolpert, D. M. (2008). Noise in the nervous system. *Nat. Rev. Neurosci.* **9**, 292–303.

Farley, C. T., Glasheen, J. and Mahon, T. A. M. C. (1993). Running springs: Speed and

animal size. **86**, 71–86.

Farshidian, F., Neunert, M., Winkler, A. W., Rey, G. and Buchli, J. (2017). An Efficient Optimal Planning and Control Framework For Quadrupedal Locomotion. *2017 IEEE Int. Conf. Robot. Autom.* 93–100.

Fiorini, P. and Burdick, J. (2003). The development of hopping capabilities for small robots. *Auton. Robots* **14**, 239–254.

Fleischmann, J. (2015). DEM-PM Contact Model with Multi-Step Tangential Contact Displacement History. *Madison, Tech. Rep. No. TR-2015* 18.

Frantsevich, L. (2004). Righting kinematics in beetles (Insecta: Coleoptera). *Arthropod Struct. Dev.* **33**, 221–235.

Full, R. J. and Koditschek, D. E. (1999). Templates and anchors: Neuromechanical hypotheses of legged locomotion on land. *J. Exp. Biol.* **202**, 3325–3332.

Full, B. Y. R. J. and Tu, M. S. (1990). Mechanics of six-legged runners. *J. Exp. Biol.* **148**, 129–146.

Gamini Dissanayake, M. W. M., Newman, P., Clark, S., Durrant-Whyte, H. F. and Csorba, M. (2001). A solution to the simultaneous localization and map building (SLAM) problem. *IEEE Trans. Robot. Autom.* **17**, 229–241.

Gammaitoni, L. and Bulsara, A. R. (2002). Noise Activated Nonlinear Dynamic Sensors. *Phys. Rev. Lett.* **88**, 4.

Gangapurwala, S., Geisert, M., Orsolino, R., Fallon, M. and Havoutis, I. (2022). RLOC: Terrain-Aware Legged Locomotion Using Reinforcement Learning and Optimal Control. *IEEE Trans. Robot.* **38**, 2908–2927.

Gao, Y. (2016). *Contemporary planetary robotics: an approach toward autonomous systems*. John Wiley & Sons.

Gart, S. W. and Li, C. (2018). Body-terrain interaction affects large bump traversal of insects and legged robots. *Bioinspiration and Biomimetics* **13**, 026005.

Gart, S. W., Yan, C., Othayoth, R., Ren, Z. and Li, C. (2018). Dynamic traversal of large gaps by insects and legged robots reveals a template. *Bioinspiration and Biomimetics* **13**, 026006.

Gibson, J. J. (1979). The theory of affordances. The ecological approach to visual perception. *Psychol. Press* 50–60.

Goldman, D. I., Chen, T. S., Dudek, D. M. and Full, R. J. (2006). Dynamics of rapid vertical climbing in cockroaches reveals a template. *J. Exp. Biol.* **209**, 2990–3000.

Grizzle, J. W., Abba, G. and Plestan, F. (2001). Asymptotically stable walking for biped robots: Analysis via systems with impulse effects. *IEEE Trans. Automat. Contr.* **46**, 51–64.

Guizzo, E. and Ackerman, E. (2015a). The hard lessons of DARPA's robotics challenge [News]. *IEEE Spectr.* **52**, 11–13.

Guizzo, E. and Ackerman, E. (2015b). DARPA Robotics Challenge: A Compilation of Robots Falling Down.

Han, Y., Wang, Y. and Li, C. (2017). Body shape helps legged robots climb and turn in complex 3-D terrains. In *Bulletin of the American Physical Society 62*, pp. Y12--002.

Han, Y., Othayoth, R., Wang, Y., Hsu, C. C., de la Tijera Obert, R., Francois, E. and Li, C. (2021). Shape-induced obstacle attraction and repulsion during dynamic

locomotion. *Int. J. Rob. Res.* **40**, 939–955.

Hanggi, P. (1986). Escape from a metastable state. *J. Stat. Phys.* **42**, 105–148.

Harley, C. M., English, B. A. and Ritzmann, R. E. (2009). Characterization of obstacle negotiation behaviors in the cockroach, Blaberus discoidalis. *J. Exp. Biol.* **212**, 1463–1476.

Hart, P. E., Nilsson, N. J. and Raphael, B. (1968). A Formal Basis for the Heuristic Determination of Minimum Cost Paths. *Syst. Sci. Cybern.* **4**, 100–107.

Heams, T. (2014). Randomness in biology. *Math. Struct. Comput. Sci.* **24**,.

Ho, H. T. (1997). Noise impact on servo TMR. *Proc. Am. Control Conf.* **5**, 2906–2909.

Hoffmann, G. (1983). The random elements in the systematic search behavior of the desert isopod Hemilepistus reaumuri. *Behav. Ecol. Sociobiol.* **13**, 81–92.

Holmes, P., Full, R. J., Koditschek, D. and Guckenheimer, J. (2006). The dynamics of legged locomotion: Models, analyses, and challenges. *SIAM Rev.* **48**, 207–304.

How, J. P. and Tillerson, M. (2001). Analysis of the Impact of Sensor Noise on Formation Flying Control. *Proc. 2001 Am. Control Conf.* **5**, 3986–3991.

Hutter, M., Gehring, C., Jud, D., Lauber, A., Bellicoso, C. D., Tsounis, V., Hwangbo, J., Bodie, K., Fankhauser, P., Bloesch, M., et al. (2016). ANYmal - A highly mobile and dynamic quadrupedal robot. *IEEE Int. Conf. Intell. Robot. Syst.* **2016-Novem**, 38–44.

Hwangbo, J., Lee, J., Dosovitskiy, A., Bellicoso, D., Tsounis, V., Koltun, V. and Hutter, M. (2019). Learning agile and dynamic motor skills for legged robots. *Sci.*

Robot. **4**, 1–13.

Ilhan, B. D., Johnson, A. M. and Koditschek, D. E. (2018). Autonomous legged hill ascent. *J. F. Robot.* **35**, 802–832.

Khatib, O. (1985). Real-time obstacle avoidance for manipulators and mobile robots. *Proc. - IEEE Int. Conf. Robot. Autom.* 500–505.

Kim, H. G., Lee, D. G., Liu, Y., Jeong, K. and Seo, T. W. (2016). Hexapedal Robotic Platform for Amphibious Locomotion on Ground and Water Surface. *J. Bionic Eng.* **13**, 39–47.

Kimura, H., Fukuoka, Y. and Konaga, K. (2001). Adaptive dynamic walking of a quadruped robot using a neural system model. *Adv. Robot.* **15**, 859–878.

Koditschek, D. E., Full, R. J. and Buehler, M. (2004). Mechanical aspects of legged locomotion control. *Arthropod Struct. Dev.* **33**, 251–272.

Kovač, M., Schlegel, M., Zufferey, J. C. and Floreano, D. (2010). Steerable miniature jumping robot. *Auton. Robots* **28**, 295–306.

Kuo, A. D. (2007). The six determinants of gait and the inverted pendulum analogy: A dynamic walking perspective. *Hum. Mov. Sci.* **26**, 617–656.

Kurita, Y., Shinohara, M. and Ueda, J. (2013). Wearable sensorimotor enhancer for fingertip based on stochastic resonance effect. *IEEE Trans. Human-Machine Syst.* **43**, 333–337.

Kwak, B. and Bae, J. (2017). Design of hair-like appendages and comparative analysis on their coordination toward steady and efficient swimming. *Bioinspiration and Biomimetics* **12**, 036014.

Lee, J., Sponberg, S. N., Loh, O. Y., Lamperski, A. G., Full, R. J. and Cowan, N. J. (2008). Templates and anchors for antenna-based wall following in cockroaches and robots. *IEEE Trans. Robot.* **24**, 130–143.

Lerman, P. M. (1980). Fitting Segmented Regression Models by Grid Search. *Appl. Stat.* **29**, 77–84.

Li, C. and Lewis, K. (2022). The Need for and Feasibility of Alternative Ground Robots to Traverse Sandy and Rocky Extraterrestrial Terrain. *Adv. Intell. Syst.* **2100195**, 2100195.

Li, C. and Lewis, K. (2023). The Need for and Feasibility of Alternative Ground Robots to Traverse Sandy and Rocky Extraterrestrial Terrain. *Adv. Intell. Syst.* **5**, 1–8.

Li, C. and Qian, F. (2023). Swift progress for robots over complex terrain. *Nature* **616**, 252–253.

Li, C., Umbanhowar, P. B., Komsuoglu, H., Koditschek, D. E. and Goldman, D. I. (2009). Sensitive dependence of the motion of a legged robot on granular media. *Proc. Natl. Acad. Sci.* **106**, 3029–3034.

Li, C., Zhang, T. and Goldman, D. I. (2013). A terradynamics of legged locomotion on granular media. *Science (80-.).* **339**, 1408–1412.

Li, C., Pullin, A. O., Haldane, D. W., Lam, H. K., Fearing, R. S. and Full, R. J. (2015). Terradynamically streamlined shapes in animals and robots enhance traversability through densely cluttered terrain. *Bioinspiration and Biomimetics* **10**,.

Li, C., Kessens, C. C., Young, A., Fearing, R. S. and Full, R. J. (2016). Cockroach-inspired winged robot reveals principles of ground-based dynamic self-righting. In

2016 IEEE/RSJ International Conference on Intelligent Robots and Systems (IROS), pp. 2128–2134.

Li, C., Kessens, C. C., Fearing, R. S. and Full, R. J. (2017). Mechanical principles of dynamic terrestrial self-righting using wings. *Adv. Robot.* **31**, 881–900.

Li, C., Wöhrl, T., Lam, H. K. and Full, R. J. (2019a). Cockroaches use diverse strategies to self-right on the ground. *J. Exp. Biol.* **222**, jeb186080.

Li, C., Wöhrl, T., Lam, H. K. and Full, R. J. (2019b). Cockroaches use diverse strategies to self-right on the ground. *J. Exp. Biol.* **222**,.

Libby, T., Moore, T. Y., Chang-Siu, E., Li, D., Cohen, D. J., Jusufi, A. and Full, R. J. (2012). Tail-assisted pitch control in lizards, robots and dinosaurs. *Nature* **481**, 181–186.

Libby, T., Johnson, A. M., Chang-Siu, E., Full, R. J. and Koditschek, D. E. (2016). Comparative Design, Scaling, and Control of Appendages for Inertial Reorientation. *IEEE Trans. Robot.* **32**, 1380–1398.

Lock, R. J., Burgess, S. C. and Vaidyanathan, R. (2013). Multi-modal locomotion: from animal to application. *Bioinspir. Biomim.* **9**, 011001.

Lynch, D. J., Lynch, K. M. and Umbanhowar, P. B. (2020). The Soft-Landing Problem: Minimizing Energy Loss by a Legged Robot Impacting Yielding Terrain. *IEEE Robot. Autom. Lett.* **5**, 3658–3665.

Maladen, R. D., Ding, Y., Umbanhowar, P. B., Kamor, A. and Goldman, D. I. (2011). Mechanical models of sandfish locomotion reveal principles of high performance subsurface sand-swimming. *J. R. Soc. Interface* **8**, 1332–1345.

Marti, K. (2003). Stochastic optimization methods in optimal engineering design under stochastic uncertainty. *ZAMM Zeitschrift fur Angew. Math. und Mech.* **83**, 795–811.

Mazhar, H., Heyn, T., Pazouki, A., Melanz, D., Seidl, A., Bartholomew, A., Tasora, A. and Negrut, D. (2013). CHRONO: A parallel multi-physics library for rigid-body, flexible-body, and fluid dynamics. *Mech. Sci.* **4**, 49–64.

McDonnell, M. D. and Ward, L. M. (2011). The benefits of noise in neural systems: Bridging theory and experiment. *Nat. Rev. Neurosci.* **12**, 415–425.

Mckenna, M. and Zeltzer, D. (1990). Dynamic Simulation of Autonomous Legged Locomotion. **24**,.

Mi, J., Wang, Y. and Li, C. (2022). Omni-Roach: A Legged Robot Capable of Traversing Multiple Types of Large Obstacles and Self-Righting. *Proc. - IEEE Int. Conf. Robot. Autom.* 235–242.

Mombaur, K. and Truong, A. (2010). From human to humanoid locomotion — an inverse optimal control approach. *Aut. Robot* 369–383.

Mombaur, K., Laumond, J. and Yoshida, E. (2010). An Optimal Control-Based Formulation to Determine Natural Locomotor Paths for Humanoid Robots ∗. *Adv. Robot.* **24**, 515–535.

Moore, E. Z., Campbell, D., Grimminger, F. and Buehler, M. (2002). Reliable stair climbing in the simple hexapod “RHex.” *Proceedings-IEEE Int. Conf. Robot. Autom.* **3**, 2222–2227.

Moore, T. Y., Cooper, K. L., Biewener, A. A. and Vasudevan, R. (2017). Unpredictability of escape trajectory explains predator evasion ability and microhabitat preference of

desert rodents. *Nat. Commun.* **8**, 1–9.

NASA/JPL-Caltech (2019). Driving Distances on Mars and the Moon.

Nilsson, J., Bernhardsson, B. and Wittenmark, B. (1998). Stochastic analysis and control of real-time systems with random time delays. *Automatica* **34**, 57–64.

Okada, J. and Toh, Y. (2006). Active tactile sensing for localization of objects by the cockroach antenna. *J. Comp. Physiol. A Neuroethol. Sensory, Neural, Behav. Physiol.* **192**, 715–726.

Oliveira, L. F. P., Moreira, A. P. and Silva, M. F. (2021). Advances in forest robotics: A state-of-the-art survey. *Robotics* **10**, 1–20.

Osborne, L. C., Lisberger, S. G. and Bialek, W. (2005). A sensory source for motor variation. *Nature* **437**, 412–416.

Othayoth, R. and Li, C. (2021). Propelling and perturbing appendages together facilitate strenuous ground self-righting. *Elife* **10**, 1–23.

Othayoth, R., Xuan, Q. and Li, C. (2017). Induced vibrations increase performance of a winged self-righting robot. In *Bulletin of the American Physical Society 62*, pp. Y12-001.

Othayoth, R., Thoms, G. and Li, C. (2020). An energy landscape approach to locomotor transitions in complex 3D terrain. *Proc. Natl. Acad. Sci. U. S. A.* **117**, 14987–14995.

Othayoth, R., Xuan, Q., Wang, Y. and Li, C. (2021). Locomotor transitions in the potential energy landscape-dominated regime. *Proc. R. Soc. B Biol. Sci.* **288**,.

Patel, A. and Braae, M. (2014). Rapid acceleration and braking: Inspirations from the

cheetah's tail. *Proc. - IEEE Int. Conf. Robot. Autom.* 793–799.

Pazouki, A., Kwarta, M., Williams, K., Likos, W., Serban, R., Jayakumar, P. and Negrut, D. (2017). Compliant contact versus rigid contact: A comparison in the context of granular dynamics. *Phys. Rev. E* **96**, 1–13.

Popov, V. L. (2010). *Contact Mechanics and Friction*.

Pratt, G. A. (2014). Robot to the rescue. *Bull. At. Sci.* **70**, 63–69.

Qian, F., Zhang, T., Korff, W., Umbanhowar, P. B., Full, R. J. and Goldman, D. I. (2015). Principles of appendage design in robots and animals determining terradynamic performance on flowable ground. *Bioinspiration and Biomimetics* **10**,.

Raibert, M. H. (1986). *Legged robots that balance*. MIT Press.

Raibert, M. (2008). BigDog, the rough-terrain quadruped robot. *IFAC Proc. Vol.* **17**, 6–9.

Ramírez, R., Pöschel, T., Brilliantov, N. V. and Schwager, T. (1999). Coefficient of restitution of colliding viscoelastic spheres. *Phys. Rev. E - Stat. Physics, Plasmas, Fluids, Relat. Interdiscip. Top.* **60**, 4465–4472.

Reddy, A. H., Kalyan, B. and Murthy, C. S. N. (2015). Mine Rescue Robot System – A Review. *Procedia Earth Planet. Sci.* **11**, 457–462.

Reingold, S. C. and Camhi, J. M. (1977). A quantitative analysis of rhythmic leg movements during three different behaviors in the cockroach, Periplaneta americana. *J. Insect Physiol.* **23**, 1407–1420.

Reynolds, A. M. and Rhodes, C. J. (2009). The Lévy flight paradigm: Random search patterns and mechanisms. *Ecology* **90**, 877–887.

Rimon, E. and Koditschek, D. E. (1992). Exact robot navigation using artificial potential functions. *IEEE Trans. Robot. Autom.* **8**, 501–518.

Roberts, S. F., Koditschek, D. E. and Miracchi, L. J. (2020). Examples of Gibsonian Affordances in Legged Robotics Research Using an Empirical, Generative Framework. *Front. Neurorobot.* **14**, 1–9.

Roos, P. E. and Dingwell, J. B. (2010). Influence of simulated neuromuscular noise on movement variability and fall risk in a 3D dynamic walking model. *J. Biomech.* **43**, 2929–2935.

Roth, E., Zhuang, K., Stamper, S. A., Fortune, E. S. and Cowan, N. J. (2011). Stimulus predictability mediates a switch in locomotor smooth pursuit performance for Eigenmannia virescens. *J. Exp. Biol.* **214**, 1170–1180.

Roth, E., Hall, R. W., Daniel, T. L. and Sponberg, S. (2016). Integration of parallel mechanosensory and visual pathways resolved through sensory conflict. *Proc. Natl. Acad. Sci. U. S. A.* **113**, 12832–12837.

Saranli, U., Buehler, M. and Koditschek, D. E. (2001). RHex: A simple and highly mobile hexapod robot. *Int. J. Rob. Res.* **20**, 616–631.

Saranli, U., Rizzi, A. A. and Koditschek, D. E. (2004). Model-based dynamic self-righting maneuvers for a hexapedal robot. *Int. J. Rob. Res.* **23**, 903–918.

Schmitt, J. and Holmes, P. (2000). Mechanical models for insect locomotion: Dynamics and stability in the horizontal plane I. Theory. *Biol. Cybern.* **83**, 501–515.

Seay, J. F., Haddad, J. M., van Emmerik, R. E. A. and Hamill, J. (2006). Coordination variability around the walk to run transition during human locomotion. *Motor Control*

10, 178–196.

Sherman, E., Novotny, M. and Camhi, J. M. (1977). A modified walking rhythm employed during righting behavior in the cockroach Gromphadorhina portentosa. *J. Comp. Physiol.* ■ *A* **113**, 303–316.

Shill, J. J., Collins, E. G., Coyle, E. and Clark, J. (2015). Tactile surface classification for limbed robots using a pressure sensitive robot skin. *Bioinspiration and Biomimetics* **10**,.

Shrivastava, S., Karsai, A., Aydin, Y. O., Pettinger, R., Bluethmann, W., Ambrose, R. O. and Goldman, D. I. (2020). Material remodeling and unconventional gaits facilitate locomotion of a robophysical rover over granular terrain. *Sci. Robot.* **5**, 1–11.

Sponberg, S. and Full, R. J. (2008). Neuromechanical response of musculo-skeletal structures in cockroaches during rapid running on rough terrain. *J. Exp. Biol.* **211**, 433–446.

Sutantyo, D. K., Kernbach, S., Levi, P. and Nepomnyashchikh, V. A. (2010). Multi-robot searching algorithm using Lévy flight and artificial potential field. *8th IEEE Int. Work. Safety, Secur. Rescue Robot. SSRR-2010* 2–7.

Tan, J., Zhang, T., Coumans, E., Iscen, A., Bai, Y., Hafner, D., Bohez, S. and Vanhoucke, V. (2018). Sim-to-Real: Learning Agile Locomotion For Quadruped Robots. *Robot. Sci. Syst.*

Tasora, A., Serban, R., Mazhar, H., Pazouki, A., Melanz, D., Fleischmann, J., Taylor, M., Sugiyama, H. and B, D. N. (2015). Chrono: An Open Source Multi-physics

Dynamics Engine. In *International Conference on High Performance Computing in Science and Engineering*, pp. 19–49.

Thrun, S., Burgard, W. and Fox, D. (2000). Real-time algorithm for mobile robot mapping with applications to multi-robot and 3D mapping. *Proc. - IEEE Int. Conf. Robot. Autom.* **1**, 321–328.

Tresch, M. C., Saltiel, P., D'Avella, A. and Bizzi, E. (2002). Coordination and localization in spinal motor systems. *Brain Res. Rev.* **40**, 66–79.

Tribelhorn, B. and Dodds, Z. (2007). Evaluating the roomba: A low-cost, ubiquitous platform for robotics research and education. *Proc. - IEEE Int. Conf. Robot. Autom.* 1393–1399.

Van Beers, R. J., Baraduc, P. and Wolpert, D. M. (2002). Role of uncertainty in sensorimotor control. *Philos. Trans. R. Soc. B Biol. Sci.* **357**, 1137–1145.

Walas, K. (2013). Tactile sensing for ground classification. *J. Autom. Mob. Robot. Intell. Syst.* **7**, 18–23.

Wang, Y. and Li, C. (2023). Force sensing can help robots reconstruct potential energy landscape and guide locomotor transitions to traverse large obstacles. In *Bulletin of the American Physical Society 68*, p. W10.00008.

Wang, H., Zheng, Y. F., Jun, Y. and Oh, P. (2014). DRC-hubo walking on rough terrains. *IEEE Conf. Technol. Pract. Robot Appl. TePRA* 1–6.

Wang, Y., Othayoth Mullankandy, R. S. and Li, C. (2020). Active adjustments help cockroaches traverse obstacles by lowering potential energy barrier. In *Bulletin of the American Physical Society 65*, p. APS.

Wang, Y., Othayoth, R. and Li, C. (2022). Cockroaches adjust body and appendages to traverse cluttered large obstacles. *J. Exp. Biol.* **225**,.

Watson, J. T. and Ritzmann, R. E. (1997). Leg kinematics and muscle activity during treadmill running in the cockroach, Blaberus discoidalis: I. Slow running. *J. Comp. Physiol. - A Sensory, Neural, Behav. Physiol.* **182**, 11–22.

Wiesenfeld, K. and Moss, F. (1995). Stochastic resonance and the benefits of noise: From ice ages to crayfish and SQUIDs. *Nature* **373**, 33–36.

Wong, J. Y. (2009). *Terramechanics and off-road vehicle engineering: terrain behaviour, off-road vehicle performance and design*. Butterworth-heinemann.

Wu, J. and Popović, Z. (2010). Terrain-Adaptive Bipedal Locomotion Control. *ACM Trans. Graph.* **29**, 1–10.

Wu, X. A., Huh, T. M., Mukherjee, R. and Cutkosky, M. (2016). Integrated Ground Reaction Force Sensing and Terrain Classification for Small Legged Robots. *IEEE Robot. Autom. Lett.* **1**, 1125–1132.

Xuan, Q. and Li, C. (2019). In silico experiments reveal the importance of randomness of motions in cockroach's winged self-righting. In *Integrative and Comparative Biology 59*, pp. E255–E255.

Xuan, Q. and Li, C. (2020a). Randomness in appendage coordination facilitates strenuous ground self-righting. *Bioinspir. Biomim.*

Xuan, Q. and Li, C. (2020b). Coordinated Appendages Accumulate More Energy to Self-Right on the Ground. *IEEE Robot. Autom. Lett.* **5**, 6137–6144.

Zheng, B., Xuan, Q. and Li, C. (2021). A minimalistic stochastic dynamics model of

cluttered obstacle traversal. 1–8.

Zimmet, A. M., Cao, D., Bastian, A. J. and Cowan, N. J. (2020). Cerebellar patients have intact feedback control that can be leveraged to improve reaching. *Elife* **9**, 1–25.

Zucker, M., Ratliff, N., Stolle, M., Chestnutt, J., Bagnell, J. A., Atkeson, G. and Kuffner, J. (2011). Optimization and learning for rough terrain legged locomotion. *Int. J. Rob. Res.* **30**, 175–191.

Vita

Qihan Xuan was born in Shaoxing, China on Oct. 22th, 1994 to XIngding Xuan and Youdi Xue. He grew up in Shaoxing, China and went to Beijing, China to attend Peking University in 2013. He received a Bachelor of Physics there in 2017. He then went to Baltimore, MD, USA in August 2017 to pursue a doctoral degree at Johns Hopkins University under the supervision of Prof. Chen Li. During this program, he received a Master of Science in Engineering degree in Robotics in 2020. His work has been published in journals such as *Robotics and Automation Letters*, *Proceedings of the Royal Society B*, and *Bioinspiration and Biomimetics*.